Advanced Land Imager Science Validation Summary

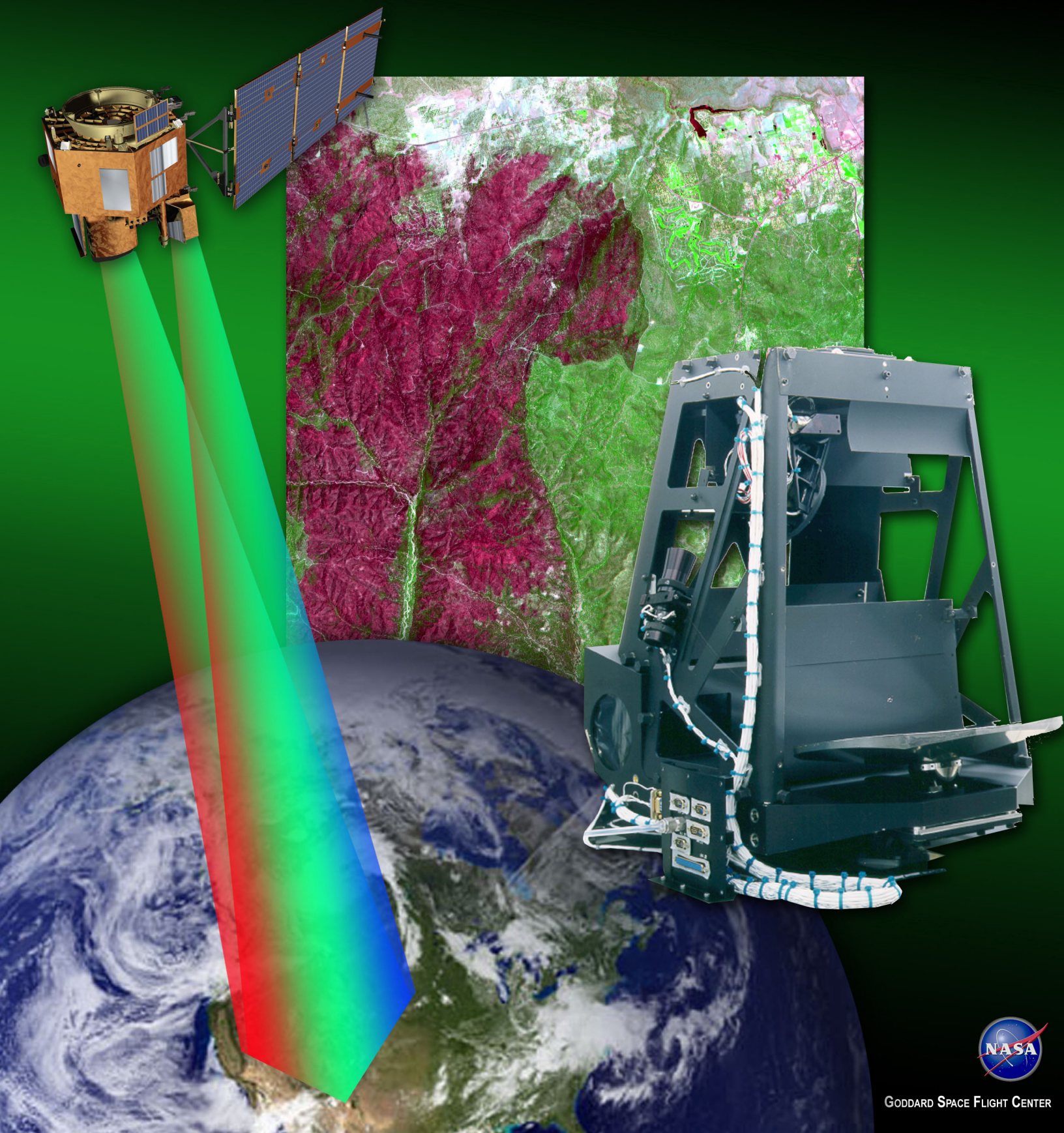

NASA

Goddard Space Flight Center

EO-1 Advanced Land Imager

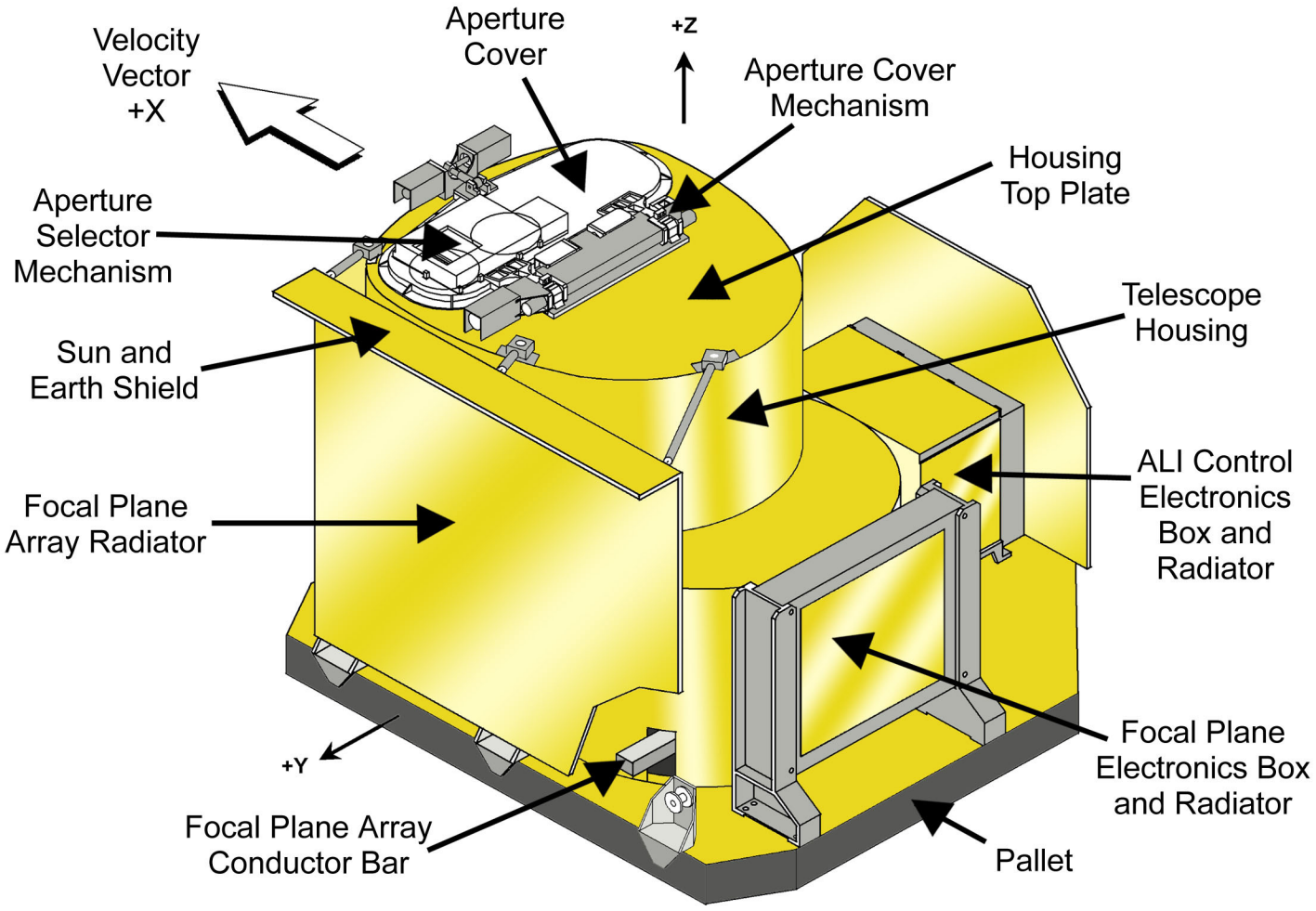

ALI vs. ETM+ Specifications

ALI	Specifications	ETM+
100	Mass (kg)	425
100	Power (W)	545
0.2	Size (m^3)	1.4
80 x 50 x 50	Size (cm)	196 x 114 x 66
10	VNIR / SWIR Bands	7
6200	Detectors Per Band	16
None	Thermal Bands	1
400	Data Rate (Mbps)	150
10	Pan Resolution (m)	15
5	Relative SNR	1

EO-1 Advanced Land Imager Science Validation Summary

Stephen G. Ungar
EO-1 Mission Scientist
NASA/GSFC

BACKGROUND

The Advanced Land Imager (ALI), flown on the New Millennium Program's first Earth Observing Mission (EO-1), represents a potential Landsat follow-on capability based on multispectral "push broom" imaging and wide field silicon carbide reflective optics. To reduce cost and minimize the required schedule, the implementation of ALI as flown on EO-1 contains a partially populated focal plane, fully sufficient for the required technology validation. Relative to the imager on the current Landsat 7, the Enhanced Thematic Mapper Plus (ETM+), a fully populated ALI represents a four fold reduction in mass, power, and volume while achieving a 5-10 fold increase in signal-to-noise ratio across all ten bands. The EO-1 mission was launched in November 2000 and is presently fully functional and engaged in an extended mission.

This report summarizes the science validation findings for the performance of the Advanced Land Imager (ALI). Individual summaries for each of the Science Validation Team (SVT) investigations pertaining to the ALI, as supplied by the PI involved, are attached to this report. The overall goal of the ALI science validation is to assess how suitable ALI technology, and the techniques developed for using this technology on EO-1, is for meeting Landsat mission continuity requirements. The metric used for these studies is ALI performance measured in terms of Landsat 7 ETM+ performance. The studies fall into two broad categories:

(1) Comparison of radiometric performance against well characterized targets, and

(2) Comparison of results from typical remote sensing applications studies.

ALI RADIOMETRIC CHARACTERIZATION

Pre-Flight Characterization

The EO-1 SVT participated in pre-launch radiometric assessment studies, and played a dominant role in measuring the post-launch radiometric performance of the EO-1 ALI. The EO-1 Mission Science Office (MSO) maintained a computerized analysis facility at the Massachusetts Institute of Technology's Lincoln Laboratory (LL) and participated

fully in the pre-flight calibration of the ALI. Brian Markham (Landsat Calibration Scientist) fully characterized the LL integrating sphere, the source of ALI calibration, with the Landsat Transferred Radiometer (LXR) on two separate occasions, thereby establishing a pre-launch basis for comparisons between ALI and ETM+. The MSO and the SVT attended many of the preflight calibration reviews and participated actively in the analysis of pre-flight calibration data.

The geometric behavior of the ALI sensor array elements was established through theodolite measurements performed at the Lincoln Laboratory prior to launch. These measurements allowed for the establishment of a matrix of line-of-sight "pointing" vectors to be used in determining where on the ground each sensor element was imaging.

On-Orbit Characterization

A variety of measurements were made during the first 90 days of launch to checkout instrument performance and confirm or modify the pre-launch characterization. The EO-1 SVT participated in collaboration with the LL Instrument Team to establish a post-launch characterization of the ALI. In particular, an extensive field measurement campaign was conducted at a variety of sites throughout Argentina almost immediately after launch. Detailed measurements were made of ground reflectance and atmospheric transmission, coincident with EO-1 and Landsat 7 overpasses, by teams led by Stuart Biggar of the University of Arizona, Alex Goetz of the University of Colorado, and Robert Green, AVIRIS Instrument Scientist, of JPL. Two major radiometric calibration sites consisting of highly reflective dry lakes at Barreal Blanco and high in the Andes at Arrizaro were selected as targets for EO-1/Landsat cross comparison. Satellite passes were supported by extensive coincident ground measurements and AVIRIS airborne overflights. Our Australian colleagues took complementary measurements at Lake Frome in South Central Australia. The University of Arizona group made measurements simultaneous with EO-1 and Landsat 7 overpasses during the spring, summer, and fall of 2001 at the traditional Landsat and Terra test sites at Railroad Valley and Ivanpah. Additionally, Dennis Helder of the University of South Dakota analyzed in excess of 600 EO-1 scenes to compare the stability in response of ALI against his extended characterization of Landsat 7 carried out while he was a member of the Landsat Science Team. Results based on these analyses are as follows:

(1) Short-term stability is excellent and comparable in every respect to the performance of Landsat 7;

(2) The signal to noise ratio of ALI is between 5 and 10 times that of Landsat 7;

(3) The solar, lunar, lamp-based, and vicarious calibrations lead to a consistent picture of a very small drift in ALI calibration coefficients over time confirming the ability to reliably calibrate the instrument to within a few percent;

(4) Measurements of the ALI bands 4 and 4P response indicate less sensitivity to atmospheric water vapor content than the response present in Landsat 7 band 4.

The EO-1 MSO has continued to trend the performance of ALI through the extended mission;

(5) The pre-launch geometric characterization of the ALI sensor array elements in conjunction with a spacecraft pointing model demonstrate that the EO-1 ALI pointing accuracy is within 50 m cross-track and 100 m along-track; and

(6) A comparison of the EO-1 and Landsat 7 pan bands over areas of regular geometric shapes clearly indicates the superior geometric performance of ALI.

TYPICAL REMOTE SENSING APPLICATION STUDIES

The performance of ALI in a series of remote sensing application studies by the EO-1 SVT met or exceeded results obtained from Landsat 7 ETM+ in every instance. Results of the ALI application studies, including comparisons against Landsat, are presented in the attached SVT summary reports. For purposes of this overall summary we selected representative examples for four landscapes of interest to the Earth Science Enterprise (ESE). Please refer to Table 1 (below) to clarify the specifics of the comparisons addressed in this section.

Table 1. Band characteristics for Landsat ETM+ and EO-1 ALI sensors.

	EO-1 ALI		Landsat ETM+	
Band	**Wavelength (μm)**	**Ground Resolution (m)**	**Wavelength (μm)**	**Ground Resolution (m)**
1p	0.433 – 0.453	30	n/a	n/a
1	0.45 – 0.515	30	0.45 – 0.515	28.5
2	0.525 – 0.605	30	0.525 – 0.605	28.5
3	0.633 – 0.69	30	0.63 – 0.69	28.5
4	0.775 – 0.805	30	0.75 – 0.90	28.5
4p	0.845 – 0.89	30		
5p	1.2 – 1.3	30	n/a	n/a
5	1.55 – 1.75	30	1.55 – 1.75	28.5
7	2.08 – 2.35	30	10.40 – 12.5	28.5
Pan	0.48 – 0.69	10	0.52 – 0.90	14.25

n/a = Not applicable

Agricultural Applications

David Lobell and Gregory Asner of Stanford University at their study site in Mexico conducted a comparison of EO-1 ALI and Landsat 7 ETM+ for crop identification and yield prediction. Radiance measurements for both ALI and ETM+ in the five bands with similar wavelength ranges agreed very well in the 115 fields surveyed. These fields exhibited cover types ranging from bare soil to fully developed crop canopies, which facilitated comparisons across a wide range of values in each band. ALI fell within 3% of Landsat radiance for the five bands the two instruments had in common, and three of the five ALI bands were within 1% of the ETM+ radiances. Results also suggested that the

"prime" ALI bands (1p, 4p, and 5p) added little spectral information over that available from ETM+ data. Overall classification accuracy did increase from 72.0% with ETM+ to 81.4% for ALI, resulting mainly from improved separation of maize from wheat. This increased distinction between maize and wheat was attributed in part to the effect of canopy water status on near-IR reflectance derivatives. The additional spectral information in ALI, residuals of a regression between bands 4 and 4p, although of small magnitude, appeared significant in crop classification. The greater sensitivity of ALI in the near-IR region demonstrated the usefulness of its two near-IR bands (4 and 4p).

A study conducted by Susan Moran of the USDA (a member of the Landsat 7 Science Team) quantified the continuity of satellite-retrieved surface reflectance for the three most recent Landsat sensors (Landsat 4 TM, Landsat 5 TM, and Landsat 7 ETM+) and the EO-1 ALI sensor. The study was based on ground data verification and, in the case of the ETM+ to ALI comparison, coincident image analysis. Image data was obtained from two locations where extensive ground data were available: the Maricopa Agriculture Center (MAC) southwest of Phoenix, Arizona; and the Walnut Gulch Experimental Watershed in southeastern Arizona, an area that has been studied for nearly 50 years. All comparisons relied on ground measurements of surface reflectance for an independent measure of sensor response. The direct comparison between image pairs of Landsat 7 ETM+ and EO-1 ALI showed good comparability for bands 1-4 and band 7, (Root Mean Squared Error (RMSE) ≤ 0.02) and moderate results for band 5 (RMSE = 0.03). When the RMSE of all sensors were compared (to minimize the effects of different methodologies), the sensors showed excellent data continuity. The absolute differences in RMSE ranged from 0.00 to 0.02. A qualitative analysis of the new ALI spectral band 5p (1.20-1.30 μm) showed that ALI band 5p provides information that is not provided by the ETM+/ALI SWIR bands 5 and 7 for agricultural targets. Further investigation is required to determine what distinctive surface characteristics influenced the reflectance in band 5p. ALI band 4p has the advantage over both the ETM+ band 4 and ALI band 4 in that it is relatively insensitive to water vapor absorption (Table 7). Furthermore, since the reflectances retrieved from ETM+ band 4, ALI band 4, and ALI band 4p for 21 agricultural targets were nearly identical, it could be an excellent substitute band for ETM+ band 4 on the next Landsat mission. Dr Moran concluded, "The four sensors can provide excellent data continuity for temporal studies of natural resources. Furthermore, the new technologies put forward by the EO-1 ALI sensor have had no apparent negative effect on data continuity and should be considered for the next Landsat sensor payload."

The results of the two preceding investigations are entirely consistent with those obtained during an extensive two-year measurement campaign by our Australian colleagues in the Colembally Irrigation Area of central Australia

Sparsely Vegetated Applications

Sparsely vegetated regions were the subject of an investigation by Andrew Elmore and John Mustard of Brown University. Owens Valley, a semi-arid basin in eastern California characterized by drought-tolerant shrubs and grasses, was chosen for this study. ALI and ETM+ each acquired one dataset on June 21, 2001. Concurrently, field

data on %GC floristic composition was collected at 27 field sites. By averaging the near infrared (NIR) bands centered at 0.790 µm and 0.868 µm and removing the bands centered at 0.443 µm and 1.25 µm, a six-band ALI data set was created. The ETM+ and ALI data sets were then co-registered to a previously georeferenced data set and the six-band ALI data set was spectrally aligned to the ETM+ data set. End member sets were selected for the ETM+ and the ALI data that included spectra from a variety of land cover. An additional end member was selected utilizing ALI's complete range of nine bands. Spectral Mixture Analysis (SMA) was applied to the one ETM+ dataset and the two ALI datasets (six-band and nine-band). The resulting vegetation fraction images were used as the remotely sensed estimate of %GC as compared to field data. Field sites were located in each data set and compared with the remotely acquired data to determine the accuracy of the vegetation measurement. The ability of ALI and ETM+ to estimate vegetation cover relative to field results was compared using criteria that calculated the standard deviation from a perfect fit, a 1:1 line. The deviation from the 1:1 line represents the uncertainty in using remotely sensed measurements as a replacement for field-based vegetation measurements. ALI and ETM+ produced similarly accurate %GC estimates: ± 6.16 %GC for ALI and ± 5.61 %GC for ETM+ deviation from a perfect fit with the 1:1 line. Although these uncertainty values indicated little advantage to using ALI over ETM+ for these measurements, other differences between the sensors favored ALI. For example, ALI did not result in as many negative %GC values as did ETM+. And, when profiles across landscapes with low vegetation cover were compared, ALI exhibited lower pixel-to-pixel noise. Using only six ALI bands appeared to produce the same degree of accuracy as using all nine of its bands. This fact can lead investigators to conclude that increased data precision, rather than the number of bands, makes ALI a better, more accurate sensor for estimating vegetation coverage in this type of environment.

Forestry Applications

Forestry studies, over large expanses (including the greater Victoria watershed) in the Pacific Northwest, conducted by David Goodenough, of the Pacific Forestry Centre, Natural Resources Canada, have yielded results that indicate that ALI provides significant improvement in ability to differentiate between species of hardwood as compared to ETM+. Overall, species identification accuracy with ALI is 85% as compared with 75% using simultaneously acquired ETM+ data. This difference in performance is consistent with results obtained by Greg Asner for tropical forest studies in Amazonia.

"Hot Spot" (Volcano and Fire) Applications

Luke Flynn of the University of Hawaii conducted a quantitative analysis of hot spots using EO-1 ALI and Landsat 7 ETM+. The objectives of this investigation were to compare the capabilities of the two instruments to monitor active volcanic eruptions and fires as well as to assess the merits of using spacecraft flying in formation over highly temporally variable targets. Frequent saturation problems with Landsat TM bands 5 and 7, which are sensitive to high temperatures, left the most interesting parts of the lava

flows unstudied. While the qualitative aspects of these flow studies were tantalizing in that they showed that 30 m data can be used to assess geologic hazards from effusive eruptions, the limited number of relevant spectral channels of the TM precluded more quantitative assessments using more than pixel integrated temperatures. Similarly, a study of the differences in spatial temperature distribution between flows and fires demonstrated that both anomalies could have similar maximum temperatures while fires cool more rapidly than lava flows. However, TM data were insufficient to produce flux density maps of the fire data because of the inadequate dynamic range in the few relevant near-IR spectral channels. This investigation examined the sensitivity of the EO-1 instruments to high-temperature thermal anomalies such as lava flows and forest fires focusing on Mt. Etna, Sicily, as the primary study site. Covering the same spectral region as the instruments aboard EO-1 (0.4μm - 2.5μm), the FieldSpec FR system developed by Analytical Spectral Devices was also used to provide simultaneous ground-truth. In addition, a FLIR (infrared) camera collected very high spatial resolution observations of active lava flows that were then used to model the number of thermal components present. The investigators concluded the following: "The increased SNR of the ALI and better radiometric sensitivity coupled with the extra SWIR channels has produced an instrument that is very capable in terms of remote sensing of active lava flows. If ALI technology is incorporated into a replacement Landsat instrument with a fully populated focal place, the resulting data should prove highly useful in the analysis of active lava flows to an extent not possible before. The study also showed that the number and placement of channels offered by Hyperion and ALI allow investigators to assess more accurately the distribution of thermal radiators within a pixel than was available with Landsat ETM+."

CONCLUSION

The ALI technology on EO-1 has proven to be a viable alternative to the current Landsat 7 instrument, ETM+. The ALI's stability of performance, enhanced SNR, and extended dynamic range has allowed it to exceed ETM+ performance for a variety of remote sensing applications. In no case has there been any indication that a fully populated ALI instrument would not meet or exceed ETM+ performance in every respect.

EO-1 Advanced Land Imager
Science Validation Summaries

The essence of the EO-1 science validation studies that pertain most specifically to the ALI instrument is contained in the following collection of validation summaries. The list of summaries is presented below in alphabetical order of Principal Investigator authors or otherwise by first author if no PI is one of the authors (PI's name is in bold print).

A. **Abrams, Michael**, NASA Jet Propulsion Laboratory
   Satellite and Airborne Remote Sensing Investigations
B. Lobell, David and **Asner, Gregory**, University of Colorado
   Comparison of EO-1 Advanced Land Imager and Landsat Enhanced Thematic Mapper for Crop Identification and Yield Prediction in Mexico
C. Schowengerdt, Robert and **Biggar, Stuart**, University of Arizona
   Radiometric Calibration, Spatial Characterization, and Spectral Evaluation of the Advanced Land Imager and Hyperion Sensors
D. **Bindschadler, Robert,** NASA Goddard Space Flight Center
   EO-1 Ice-Sheet Investigations
E. Crawford, Melba, Neuenschwander, Amy and Ringrose, Susan, The University of Texas at Austin
   Investigations in the Okavango Delta Using EO-1 Data
F. **Flynn, Luke**, University of Hawaii at Manoa
   Quantitative Analysis of Hot Spots Using EO-1 and Landsat 7
G. **Gong, Peng**, Biging, Greg and Pu, R., University of California, Berkeley
   Retrieval of Surface Reflectance and Estimation of Forest Leaf Area Index (LAI) Using Hyperion, ALI and AVIRIS
H. **Goodenough, David G.**, Hall, R., Iisaka, J., Leckie, D., Staenz, Karl, Dyk, A., Natural Resources Canada, Hollinger, A., Canadian Space Agency, Miller, J., York University, Niemann, Olaf, University of Victoria, Zwick, H., MacDonald Dettwiler and Pearlman, Jay, The Boeing Company
   Evaluation and Validation of EO-1 for Sustainable Development (EVEOSD) of Forests
I. **Liang, Shunlin**, University of Maryland
   Using ALI Observations to Estimate Land Surface Biophysical Variables
J. Bryant, R., **Moran, M.S.**, McElroy, Holifield, C., Thome, K., Miura, T., and Biggar, S.F., University of Arizona
   Data Continuity of Earth Observation (EO-1) Advanced Land Imager (ALI) and Landsat TM and ETM+
K. Elmore, Andrew and **Mustard, John**, Brown University
   Comparison of the Precision and Accuracy of ALI and ETM+ Data for Semiarid Vegetation Studies
   Identification, Classification, and Mapping of Invasive Leafy Spurge Using Hyperion, AVIRIS, and CASI
L. **Smith, James**, NASA, Goddard Space Flight Center
   Canopy Modeling and Satellite Comparison Studies Using EO-1
M. **White, William A.**, Crawford, Melba, Erzurumlu, Sinan, Tremblay, Thomas and Raney, J.A., The University of Texas at Austin
   Evaluation of EO-1 ALI Data Through an Analysis of Land Cover and Land Use and Local Impacts of Hurricane Iris in Belize, Central America

Satellite and Airborne Remote Sensing Investigations
Michael Abrams

The objective of this study was to evaluate data acquired by the spaceborne high-resolution EO-1 Hyperion and Advanced Land Imager (ALI) sensors by integrating it with hyperspectral data from airborne sensors. This data was applied to three investigations: (1) urban and industrial mapping in Venice and Porto Marghera, Italy; (2) bathymetry using a site in Lake Tahoe, California; and (3) wetlands vegetation in the Venice Lagoon. As well as using the sensors aboard EO-1, these investigations used data acquired by TERRA ASTER, the Landsat 7 Enhanced Thematic Mapper Plus (ETM+), the Multispectral Infrared Visible Imaging Spectrometer (MIVIS) airborne imaging spectrometer, and IKONOS.

Venice Urban Mapping:
Venice consists of a low-lying land mass intersected by a number of canals. It is situated in a lagoon and also borders the ocean. Several islands near the largest land mass also are considered part of the urban area. In total, this study area encompasses a dense urban environment, a polluted lagoon, and the offshore waters of the Adriatic Sea.

Data from all six sensors were used for the urban mapping investigation. Figure 1 shows Landsat ETM+, MIVIS, and EO-1 ALI and Hyperion images for a similar area, acquired from March through July 2001. Figure 2 shows representative images for the area under study at the spatial resolution of each of the above sensors as well as for ASTER and IKONOS and provides the number of available bands.

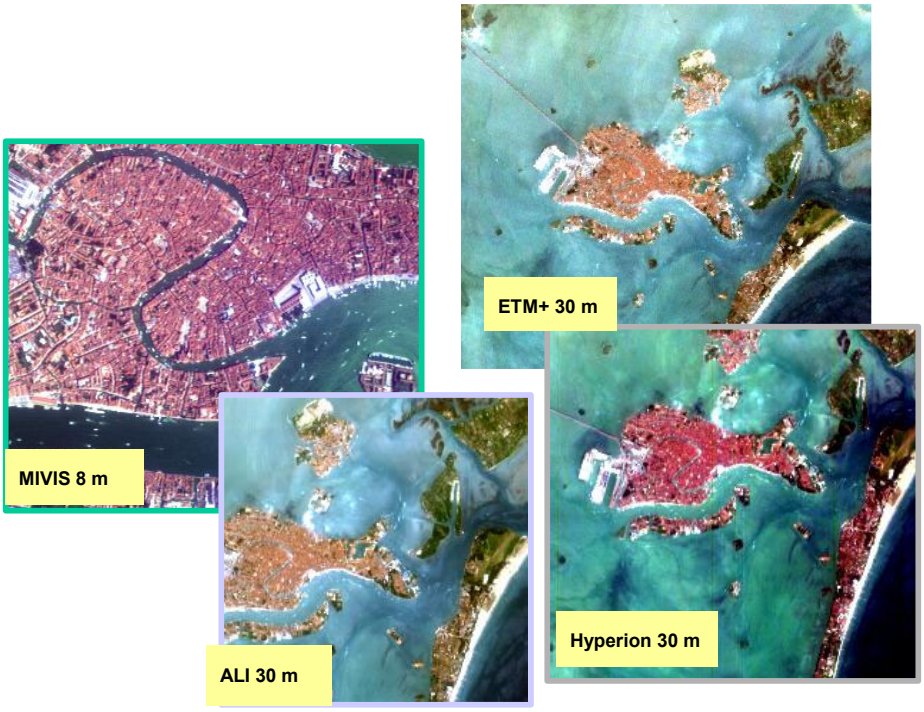

Figure 1. Similar images acquired from MIVIS, ALI, ETM+, and Hyperion.

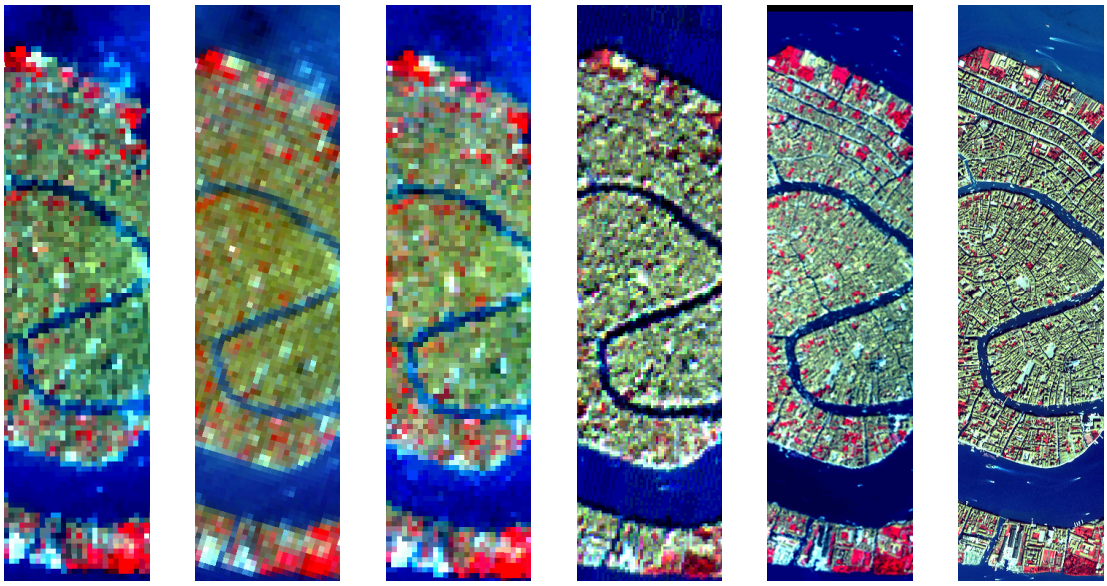

Figure 2. Spatial resolution and number of bands for each sensor.

A total of six study sites were used. The Malamocco Golf Club on the island of Lido was used to inter-calibrate the instruments used in the study by means of a group of balloon-borne instruments. The industrial area of Porto Marghera, an area equipped with several meteorological stations, also provided measurements for calibration purposes. The Marco Polo International Airport provided easily identifiable features such as runways and parking lots that were helpful during the data calibration phase. Another area was a crop area a short distance north of the airport characterized primarily by cultivated fields and very small groves of trees. Also, the Acqua Alta ocean platform in the Adriatic Sea was equipped with a cluster of permanent instruments for measuring wind, direct solar radiation, the tide, and sea waves. An additional land site was located at Pellestrina to the south of the golf club.

Data acquired by the different sensors was subject to various pre-processing (Table 1). In addition, a variety of image processing techniques was applied to the data, including using the pixel purity index (PPI), mixture tuned matched filter (MTMF), minimum noise fraction (MNF), and spectral angle mapper (SAM) techniques.

Table 1. Venice data pre-processing.

	IKONOS	MIVIS	ASTER	ALI	Hyperion	ETM+
Adjustment of VNIR and SWIR geometry					X	
Conversion to radiance at sensor		X	X	X	X	X
ACORN atmospheric correction		X Modtran	X	X	X	
Registration to IKONOS with NN		X GPX/INS	X	X	X	X

In a validation area, each of the instruments successfully differentiated a number of materials. The level of each material was given as a percentage of the total number of pixels observed in an

area. The number of pixels varied among each instrument although the relative number of pixels was consistent in most cases. Table 2 shows the percent of pixels that were identified as vegetation, tile roof, or pavement for each of the sensors.

Table 2. Percent of pixels identified in three classes.

	Vegetation	Tile Roof	Pavement
ALI	6.1	10.6	2.3
ETM+	3.7	13.3	2.3
Hyperion	3.0	12.8	9.5
ASTER	5.1	8.0	14.6
MIVIS	4.7	6.7	7.5
IKONOS	2.9	7.3	4.3

As mentioned above, various processing techniques were applied to sensor data. For a MIVIS scene, the entire roof dataset was spectrally investigated using a PPI procedure. Two different spectra were recognized as corresponding to brick coverings of new and old buildings. The spatial recognition of such covering materials was obtained by means of a SAM classification procedure. This procedure also stressed the orthogonality of the two selected spectral classes (new and old tiles—Figure 3).

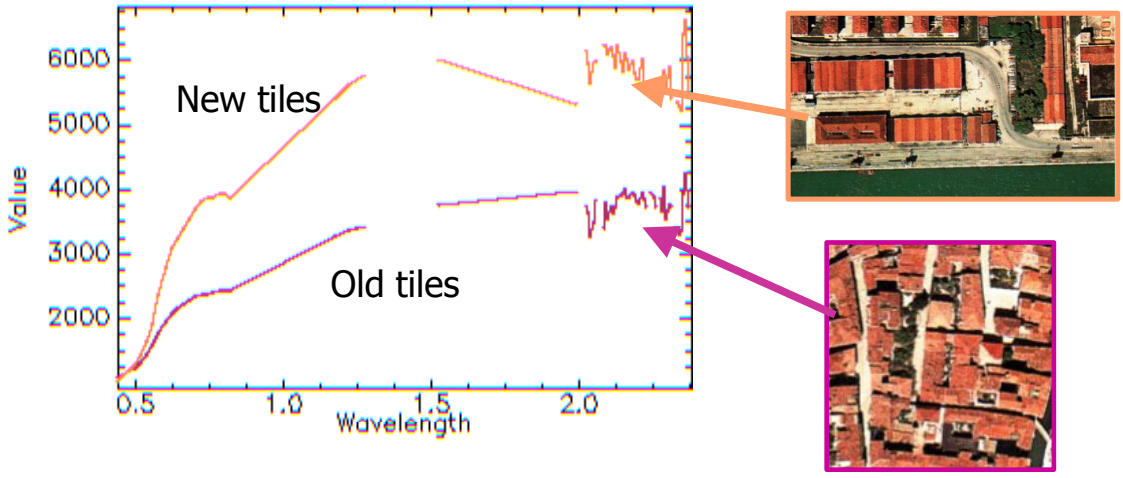

Figure 3. Mapping of old and new tiles using MIVIS.

Metallic coverings, asphalt, and trachyte spectral classes were classified using a MTMF procedure to derive the abundance of each input spectral class (Figure 4). (Trachyte is a type of igneous rock.)

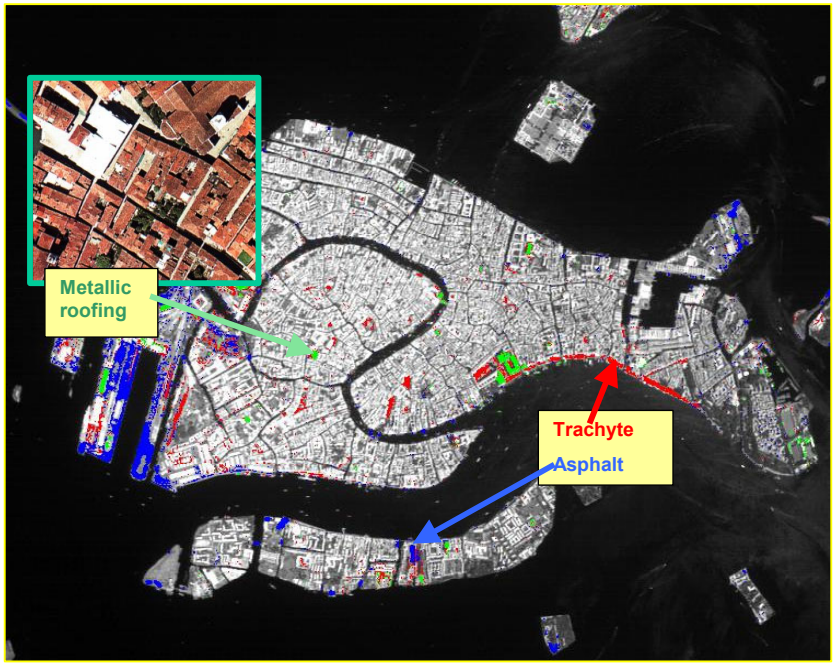

Figure 4. MIVIS Mapping of metallic roofing, trachyte, and asphalt with 8-m pixels, 102 bands.

Figure 5 shows mapping of the same area using the SAM image processing technique for each of the sensors.

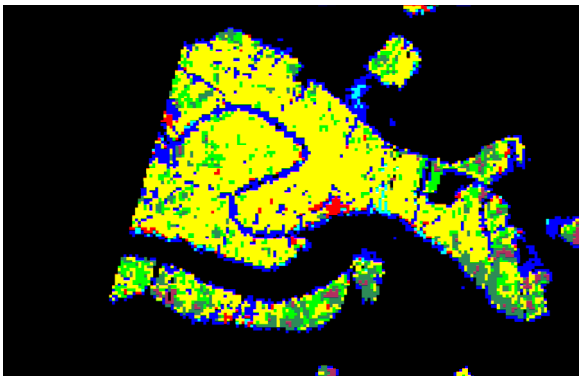

ALI

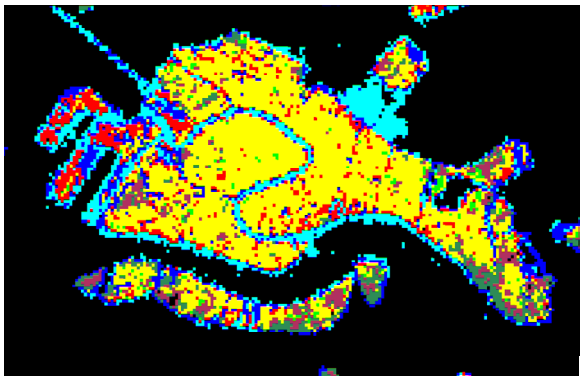

ETM+

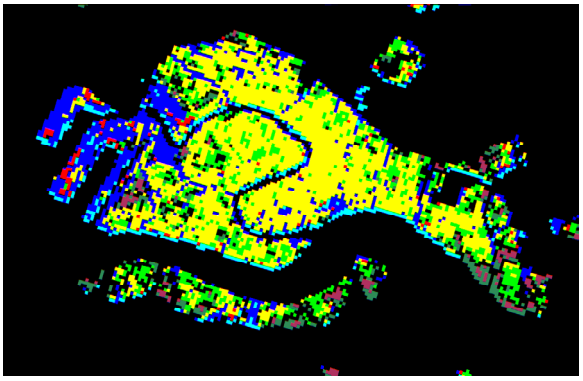

Hyperion

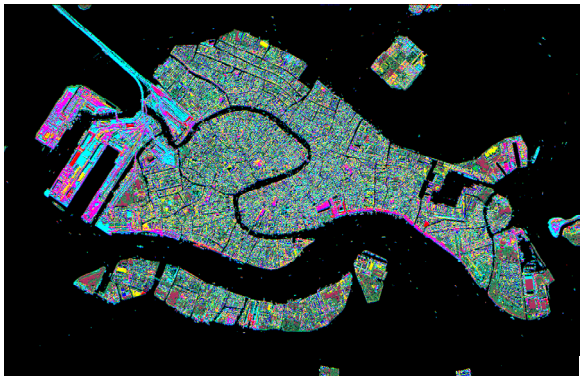

IKONOS

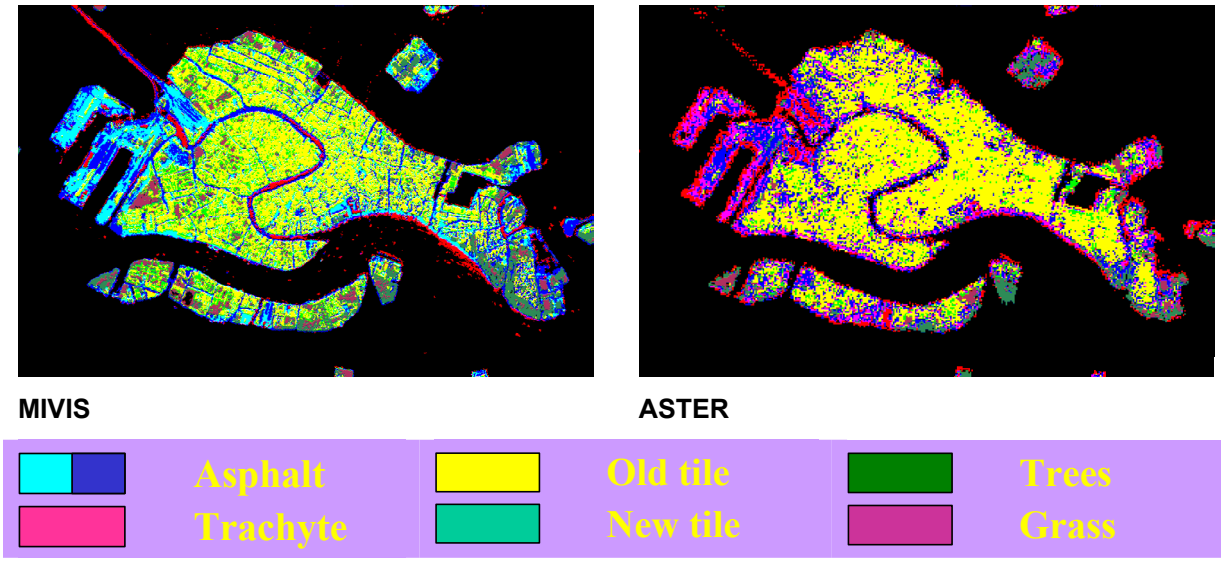

Figure 5. Spectral Angle Mapper classifications.

Hyperion data were unmixed by using end-members derived from MIVIS data. Both MIVIS and Hyperion data were converted to radiance at the sensor. Atmospheric correction was applied, and Hyperion resampled to the MIVIS spectral bands. Datasets were co-registered, and the empirical line method used to normalize Hyperion to MIVIS, using MIVIS image spectra.

Conclusion

Overall, the ALI, ETM+, and Hyperion datasets, all at 30 meters resolution, provided generally similar results. ALI allowed better mapping than ETM+ because of its larger number of bands and higher signal-to-noise ratio. Hyperion mapping was similar to that of ETM+ because of its low signal-to-noise ratio, even though its larger number of spectral bands should improve mapping. ASTER 15-meter data was better than any of the 30-meter data, due to the smaller pixel size. MIVIS data, with its 8-meter pixels, were better yet because of its hyperspectral coverage and high spatial resolution. IKONOS data provided the greatest detail, the least amount of mixed pixels, and could separate all of the urban classes.

Bathymetric Analyses at Lake Tahoe:

In this investigation, researchers obtained simultaneous ALI, ETM+, and ASTER datasets for an area of Lake Tahoe, California, to examine the abilities of the three sensors to penetrate its waters and see the bottom (Figure 6). Lake Tahoe is an attractive test site because of the exceptional clarity of its water (60+ feet), thin atmosphere, and infrequent cloud cover; however, visibility into its depths has declined from approximately 120 feet to 70 feet during the last 35 years. Depth vs. radiance profiles were extracted for the study area using ALI, ASTER, and ETM+ data. Data for this study was acquired on September 1, 2002.

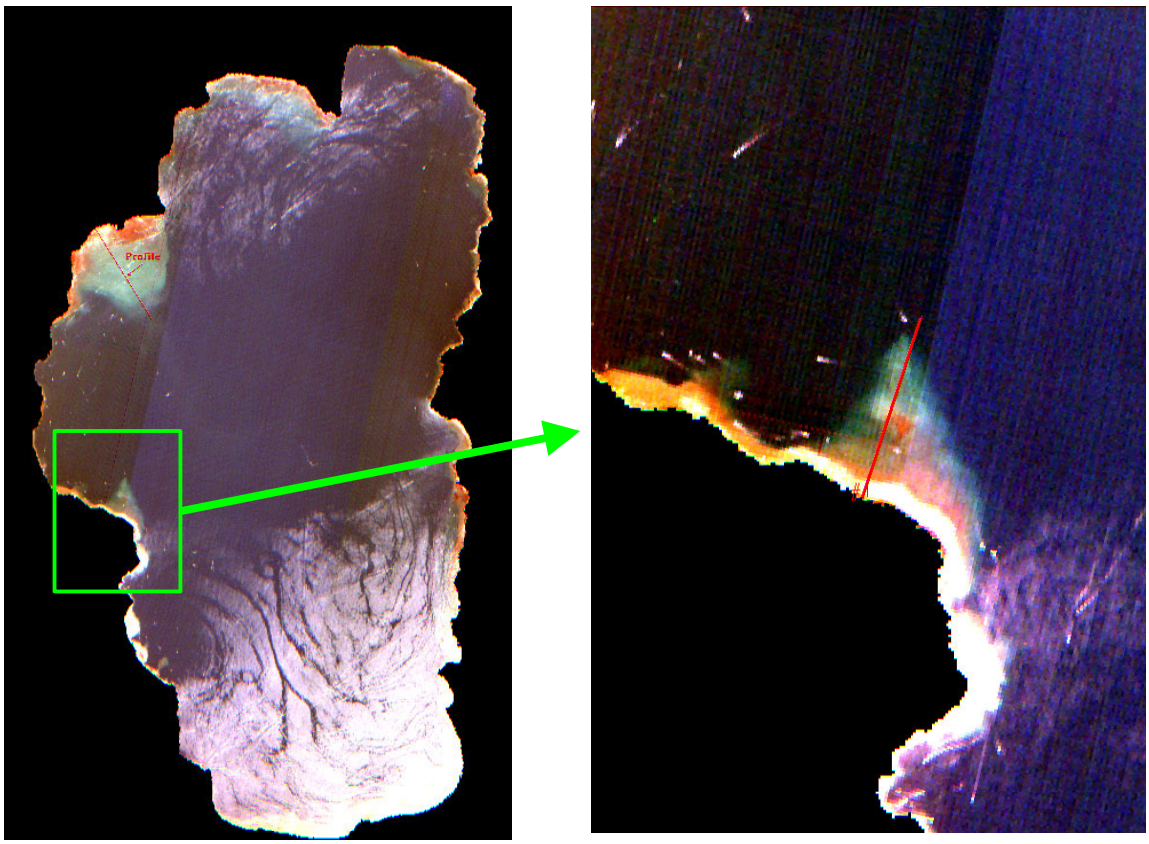

Figure 6. (Left) ALI Bands 2, 1', and 1 in red-green-blue for Lake Tahoe. The land area in the investigation is boxed off. (Right) Sub-area used to produce profiles of depth vs. radiance for ALI, ASTER, and ETM+ data.

ALI has two characteristics that potentially improve water penetration in clear waters when compared to Landsat ETM+: it has higher signal-to-noise and it has an additional band--a far blue band at a shorter wavelengths than ETM+ Band 1.

Plots were created for ALI Band 2, ETM+ Band 2, and ASTER Band 1 (Figure 7). All three instruments have similar bandpasses of 0.52-0.60 microns. ALI and ETM+ are at 30-m pixel resolution, and ASTER is at 15-m resolution (resampled to 30 meters for this analysis). All three data sets were converted to radiance using provided calibration coefficients.

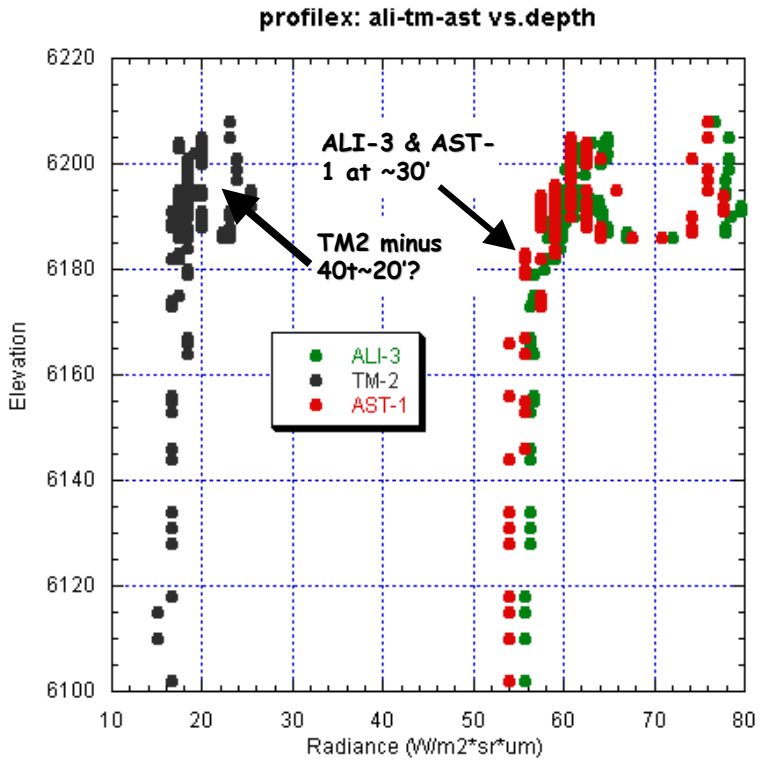

Figure 7. Depth vs. radiance plots for a profile from the shore of Lake Tahoe. The three similar 0.52-0.60 micron bands for ALI, ETM+, and ASTER were plotted. Elevation refers to number of feet the lake is located above sea level.

Data from both ALI and ASTER suggested that the bottom could be seen to a depth of 30 feet. ETM+ data were noisier, and might allow 20 feet of penetration before the radiance values became uniform. One saw a similar effect when looking at the same area with ETM+ Band 1 and the equivalent ALI band (Figure 8).

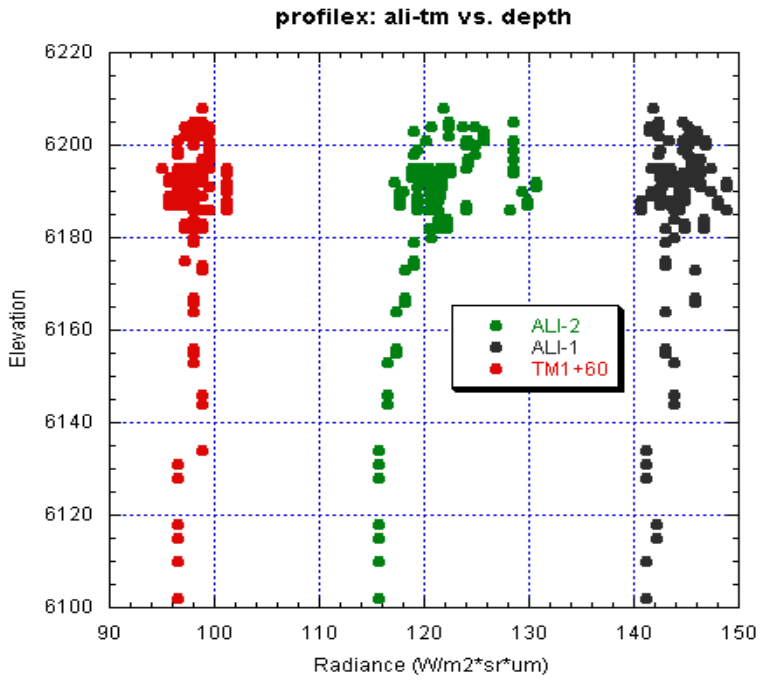

Figure 8. Depth vs. radiance plots for a profile from the shore of Lake Tahoe. The two similar 0.45-0.52 micron bands for ALI and ETM+ are plotted.

ALI data suggested penetration to a depth of 50 feet, and ETM+ Band 1 data showed no penetration, probably due to the very low signal-to-noise. A final plot shows the penetration of the ALI far blue band (Figure 9)

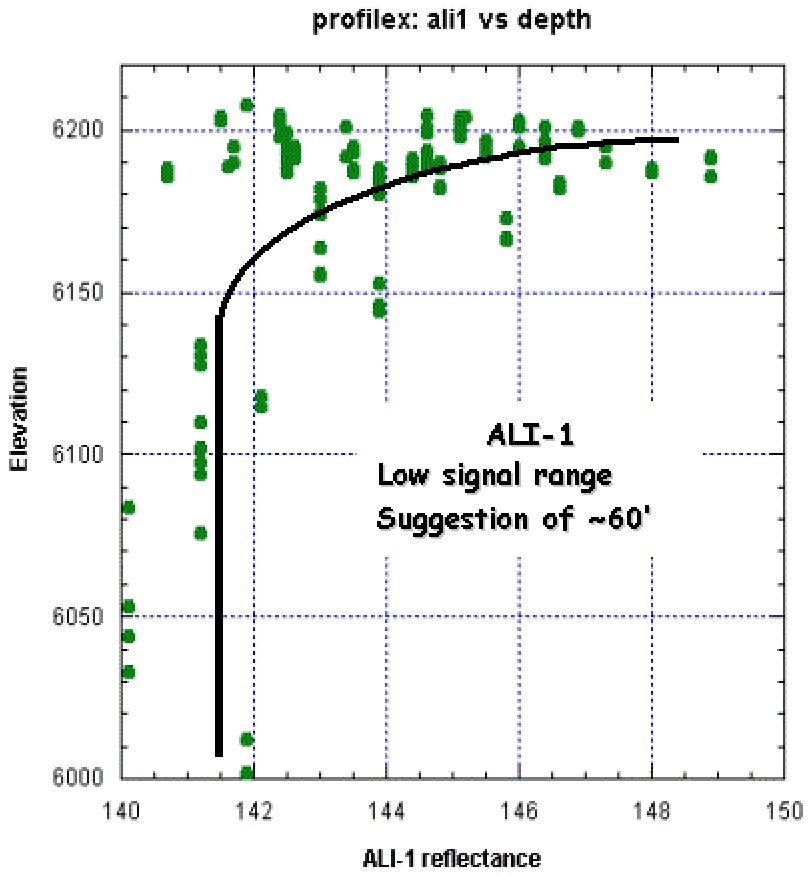

Figure 9. Depth vs. radiance for ALI far blue band.

The curve of depth vs. radiance became asymptotic at an elevation of about 6140 feet above sea level. This is at a depth of 60 feet.

Conclusion:

The analysis and comparison of ETM+ and ALI for depth penetration confirmed the initial hypothesis that ALI, with its higher signal-to-noise and additional far blue band, achieved greater depth penetration for bands equivalent to ETM+. Further, the far blue band achieved greater penetration than the traditional blue band.

Vegetation Mapping in the Venice Lagoon

In the Venice Lagoon, maps of submerged aquatic vegetation have been used to plan selective harvesting of benthic macro-algae and all activities relating to sea phanerogam plantations. Mapping techniques currently used have been based on in situ observations and aerial photo-interpretations. Results obtained with multispectral data have been limited to the detection of entire submerged vegetation cover.

In this study investigators compared the capability of ALI and ETM+ data to map submerged vegetation and separate different types of vegetation. Sea truth data was obtained from boat surveys at the time of the satellite overpasses.

ETM+ data proved to be of limited use in mapping vegetation. Image spectra derived from the data (Figure 10) showed very little distinction between macro-algae and phanerogam spectral signatures. Only discrimination of vegetation cover could be achieved.

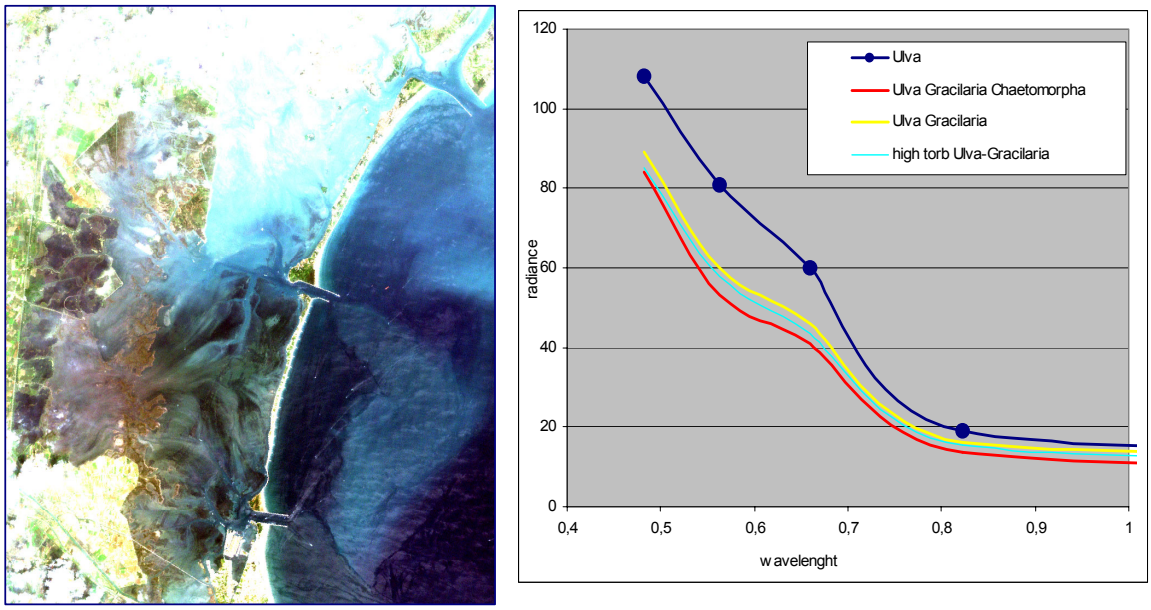

Figure 10. (Left) False color ETM+ composite image of Southern Basin in Venice Lagoon. (Right) ETM+ image spectra of macro-algae and phanerogam. Very little discrimination between species types is seen.

Information for the same areas were extracted from ALI data, and spectral signatures were plotted (Figure 11). The higher signal-to-noise of ALI as compared to ETM+ and the presence of a far blue band produced signatures that were distinct and well separated.

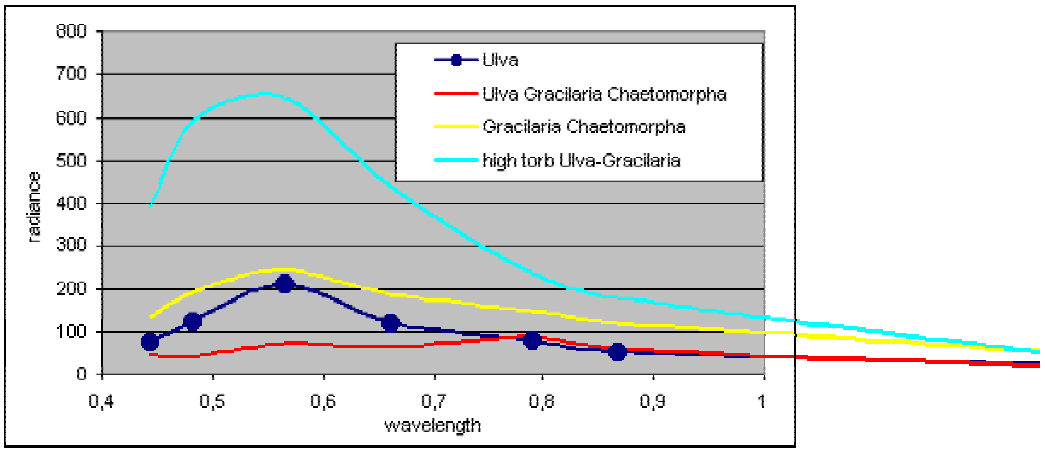

Figure 11. Spectral signatures derived from ALI data for lagoon vegetation types.

Sub-pixel mapping of vegetation types using ALI data was performed using the sub-pixel processing approach. The submerged vegetation species mixtures generated, for each pixel, a composite spectral signature. The analysis assumed that every pixel contained a fraction of the material of interest, and the remainder contained the background materials. The analysis detected the material of interest by subtracting fractions of candidate background spectra. The output was presented in the form of fraction planes (maps) for each material of interest. Analysis for benthic macro-algae and sea phanerogams is shown in Figure 12. The analysis used ALI bands 1-5 for spectral classification. Band 9 was used to mask out the land portion of the image.

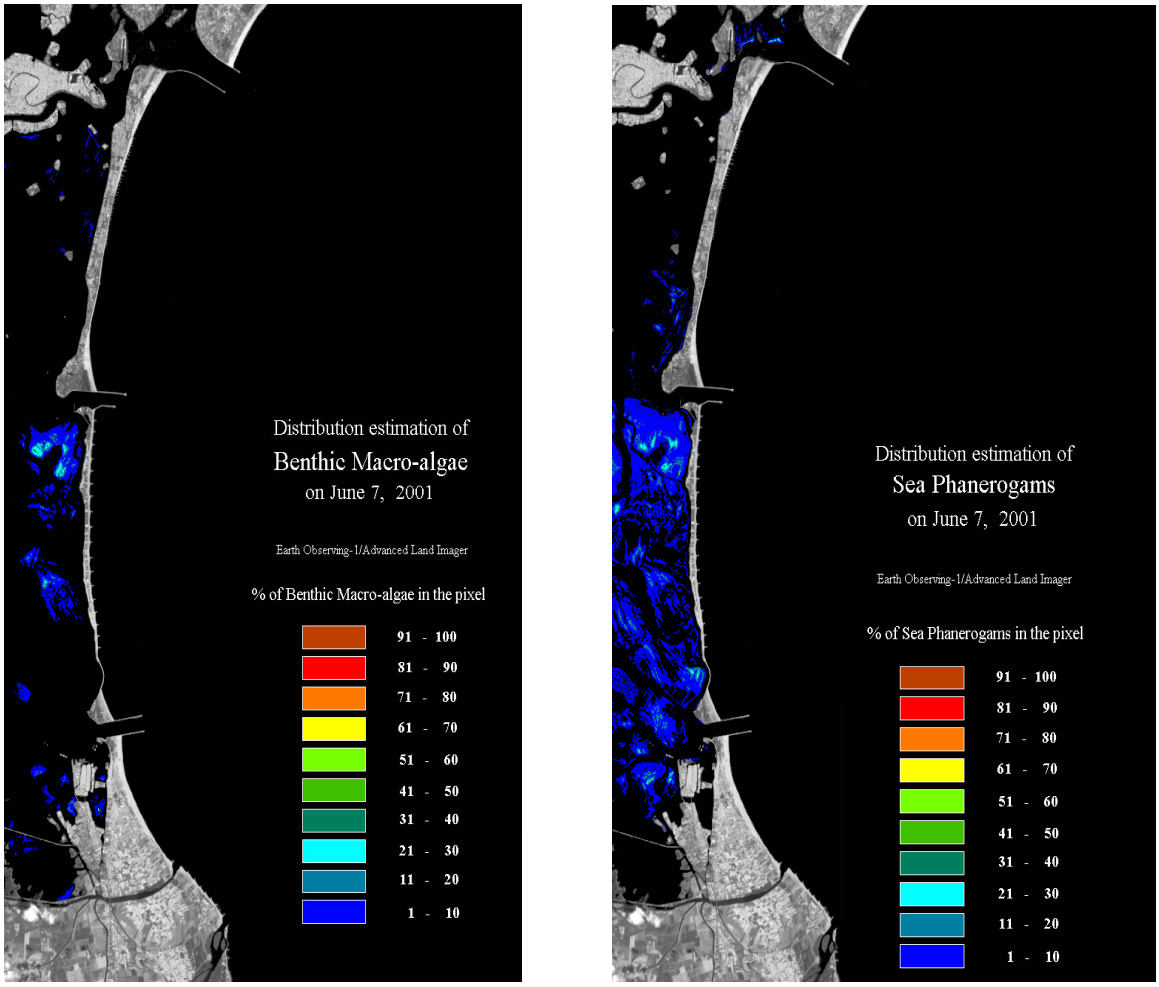

Figure 12. (Left) Sub-pixel processing classification of ALI data for benthic macro-algae. (Right) Sub-pixel processing classification of ALI data for sea phanerogams.

The sub-pixel processing approach also permitted mixture maps to be produced. For the two types of vegetation, a three-part classification was created: (1) dominantly sea phanerogams, (2) dominantly benthic macro-algae, and (3) a mixture of the two types. This was compared with sea-truth maps, and produced quite satisfactory results (Figure 13).

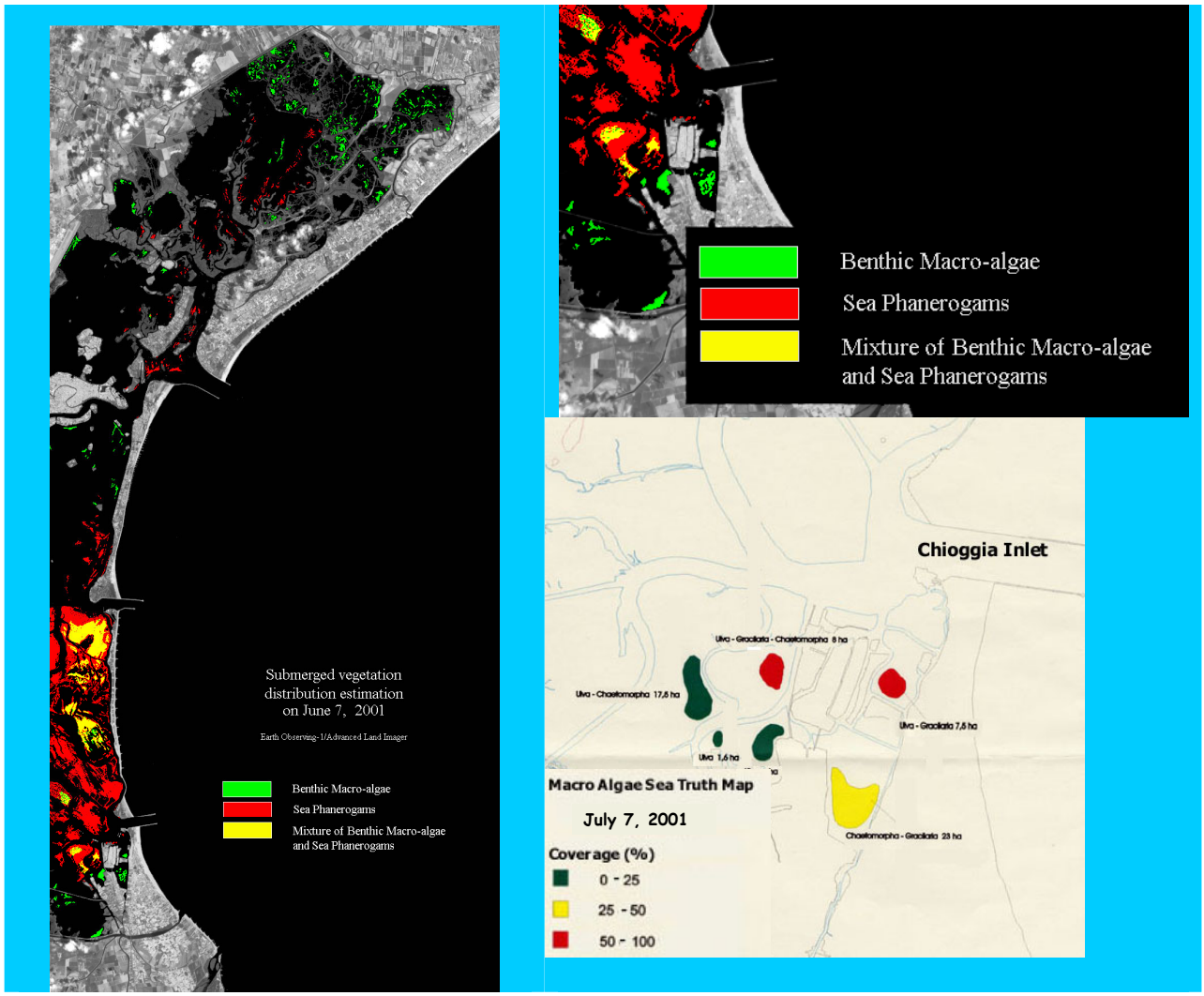

Figure 13. Sub-pixel processing mixture classification of benthic macro-algae and sea phanerogam in Venice Lagoon using ALI data.

Conclusion:

The comparison of ALI and ETM+ data for vegetation mapping in Venice Lagoon indicates that the improved signal-to-noise and additional blue band of ALI compared to ETM+ allow significantly better recognition and mapping of vegetation types.

Comparison of EO-1 Advanced Land Imager and Landsat 7 Enhanced Thematic Mapper for Crop Identification and Yield Prediction in Mexico

David Lobell and **Gregory Asner**

Possible applications for the EO-1 Advanced Land Imager (ALI) are crop identification and crop yield prediction, both important for cropland monitoring and management. Crop identification is valuable for preparing large-scale area estimates, tracking the transport of important nutrients, and for identifying constraints on crop-specific characteristics such as the efficiency of water and light use. Crop yield estimates help identify areas with high or low yields, which can be used to determine appropriate areas for crop control and management. Yield estimates also provide valuable information to farmers and governments for marketing and trading decisions. Estimating crop yields require that crop condition be measured during the growing season, typically indicated by estimates of leaf area index (LAI).

A team of investigators carried out science validation activities relating to crop identification and crop yield prediction to determine whether the ALI could produce images directly comparable to those produced by the Enhanced Thematic Mapper Plus (ETM+) flying on Landsat 7 but at significant reductions in sensor size, mass, and cost. The validation also focused on determining the suitability of the ALI for continuity of Landsat-type remote sensing.

The science validation study took place over an agricultural region in northwest Mexico. Data was collected from the two sensors on January 14, 2002. The investigators compared the measurements obtained by the sensors, which have five similar spectral bands, a panchromatic band, and similar spatial resolutions. The ALI also has three additional bands: 1p, 4p, and 5p (Table 1).

Table 1. Band characteristics for Landsat ETM+ and EO-1 ALI sensors.

	EO-1 ALI		Landsat ETM+	
Band	**Wavelength (μm)**	**Ground Resolution (m)**	**Wavelength (μm)**	**Ground Resolution (m)**
1p	0.433 – 0.453	30	n/a	n/a
1	0.45 – 0.515	30	0.45 – 0.515	28.5
2	0.525 – 0.605	30	0.525 – 0.605	28.5
3	0.633 – 0.69	30	0.63 – 0.69	28.5
4	0.775 – 0.805	30	0.75 – 0.90	28.5
4p	0.845 – 0.89	30	n/a	n/a
5p	1.2 – 1.3	30	n/a	n/a
5	1.55 – 1.75	30	1.55 – 1.75	28.5
7	2.08 – 2.35	30	10.40 – 12.5	28.5
Pan	0.48 – 0.69	10	0.52 – 0.90	14.25

n/a = Not applicable

The researchers carried out field observations during January 2002 to identify the crops present on 115 fields (Figure 1). The three most common crops identified were two types of wheat (durum and bread wheat) and irrigated maize. The wheat fields were revisited later in the growing season when physical differences between the wheat types were more pronounced to confirm the wheat type classification.

Figure 1. An ALI panchromatic image of the Yaqui Valley study region. Fields used to compare ALI and ETM+ radiance are delineated by white lines.

In the study, Landsat ETM+ imagery was collected; one minute later ALI data was acquired for virtually identical ground scenes. ALI data was calibrated to radiance with a different calibration factor being applied to each detector in each of ALI's four sensor chip assemblies (SCAs). Some bad data was evident in ALI bands 5 and 5p, and band 3 in SCA 3 suffered from misregistration that was attributed to a "leaky" pixel correction and which required manual section of ground control points to register band 3 to the other SCA 3 bands. All datasets were geo-registered to within 1 pixel using geographic information systems (GIS) coverage of roads. A rectangular, interior portion of each field was defined for the analyses. An interior area of the field was selected to eliminate potential contamination from roads or adjacent fields in the comparison. The homogeneous fields and accurate georeferencing allowed the researchers to compare the spectral responses of the ALI and ETM+ without complications arising from spatial mismatches between the sensors.

To compare the ALI and ETM+ for crop identification, a supervised maximum likelihood classification (MLC) was performed on each image using all optical bands on the two instruments and the three major crops. Accuracy was defined in terms of the percentage of total pixels correctly classified by the MLC. For yield prediction, only the maize fields were analyzed.

This was done through the use of an identical growth model for the ALI and ETM+. There were no field measurements of grain yields available for direct field validation of yields, so while the performance of ETM+ and ALI yield predictions could be compared with each other, they could not be compared with yield predictions compiled through field measurements.

Radiance measurements for both ALI and ETM+ in the five bands with similar wavelength ranges agreed very well in the 115 fields surveyed. These fields exhibited cover types ranging from bare soil to fully developed crop canopies, which facilitated comparisons across a wide range of values in each band. ALI fell within 3% of Landsat radiance for the five bands the two instruments had in commoon, and three of the five ALI bands were within 1% of the ETM+ radiances. Results also suggested that the "prime" ALI bands (1p, 4p, and 5p) added little spectral information over that available from ETM+ data. Overall classification accuracy did increase from 72.0% with ETM+ to 81.4% for ALI, resulting mainly from improved separation of maize from wheat. This increased distinction between maize and wheat was attributed in part to the effect of canopy water status on near IR reflectance derivatives. The additional spectral information in ALI, residuals of a regression between bands 4 and 4p, although of small magnitude, appeared significant in crop classification. The greater sensitivity of ALI in the near IR region demonstrated the usefulness of its two near IR bands (4 and 4p).

Neither sensor was able to differentiate between the two types of wheat.

Both sensors generated similar crop yield predictions, but since there were no field measurements of yield, concluding which sensor predicted more accurate yields was difficult.

The panchromatic bands resulted in the most dramatic differences between the two sensors (Figures 2 and 3). The ALI pan band revealed far more landscape detail than the ETM+. ALI could also recognize gradients within fields that were not evident in ETM+ data. The enhanced performance of the ALI pan band was attributed to ALI's 10 meter instantaneous field of view (IFOV) compared to the 18 - 21 meter IFOV for ETM+, ALI's superior signal-to-noise ratio (SNR) and greater dynamic range, and the fact that the ALI pan band was limited to visible wavelengths of 480 – 680 nm while the ETM+ pan band covered both visible and near IR wavelengths of 520 – 900 nm. This is important because multiple scattering by vegetation in the near IR region leads to greater pixel-to-pixel interactions, or adjacency effects. Further, sensitivity to both visible and near IR wavelengths, as in the ETM+, reduces the contrast between bare soil and surfaces with vegetation present.

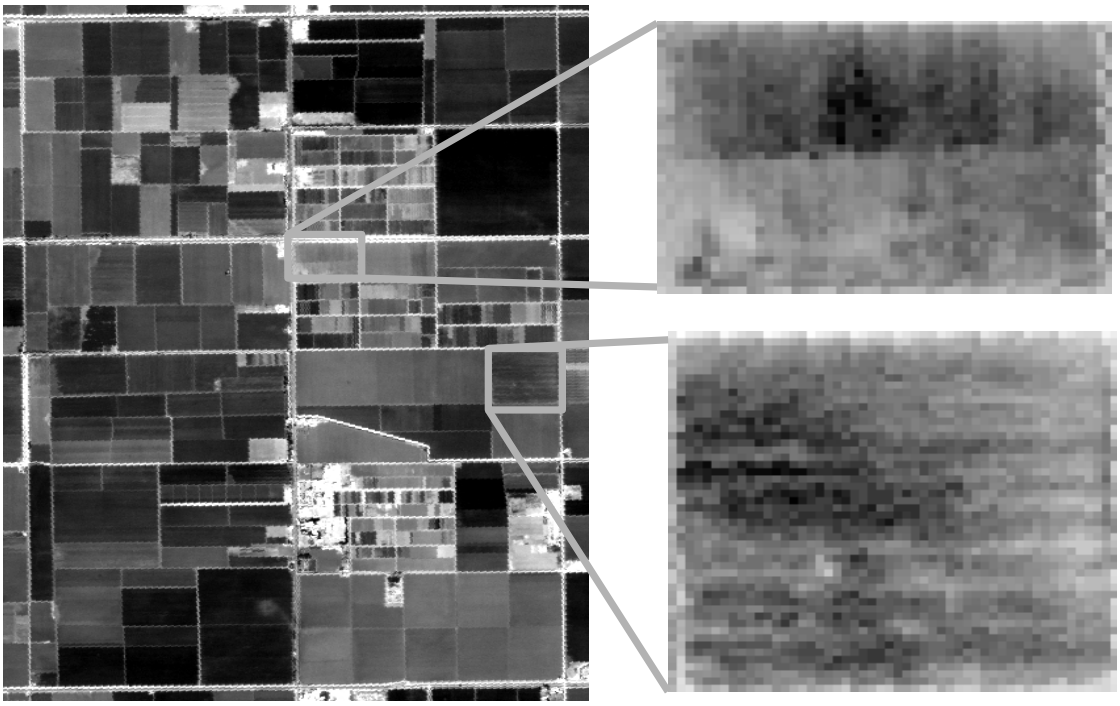

Figure 2. Panchromatic image from ALI for a 4 x 6-km area within the study region. Note the superior quality of this image when compared with the ETM+ image seen in Figure 3.

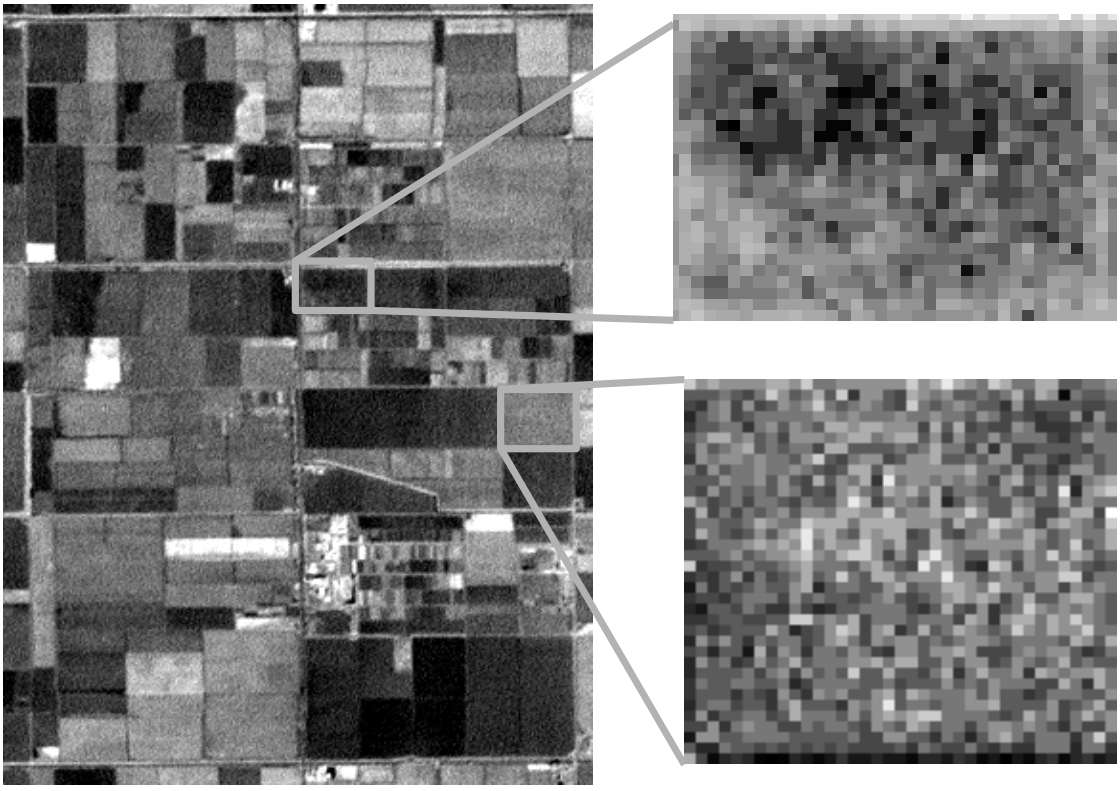

Figure 3. Panchromatic image from ETM+ for the same 4 x 6-km area as shown in Figure 2.

Conclusions:
Generally, this investigation demonstrated that ALI technology matches ETM+ performance in all areas except for problems associated with leaky pixels in ALI's band 3. ALI exceeded ETM+'s capabilities in identifying crops as a result of its additional spectral bands and produced very similar results for crop yield predictions. Further, the ALI pan band provided superior high spatial resolution images resulting from its increased SNR and dynamic range and its smaller IFOV and spectral range.

ALI's ability to capture small differences within fields is germane to precision agriculture, which aims to adjust inputs within fields to account for soil and topographic variations. ALI images would be more useful than those from the ETM+ when detecting early season deficiencies in different areas of a field, which the farmer could then address. The availability of satellite-based imagery, which is less costly than ground or airplane-based approaches, could greatly impact future precision agriculture.

Radiometric Calibration, Spatial Characterization, and Spectral Evaluation of the Advanced Land Imager and Hyperion Sensors

Robert Schowengerdt and **Stuart Biggar**

This summary describes the effort to characterize the spatial response of the EO-1 Advanced Land Imager (ALI) multispectral and panchromatic bands using datasets derived from two different geographic areas. The cross-track and in-track performance of the ALI 30-meter multispectral bands was evaluated using agricultural berms between fields at the Maricopa Agricultural Center (MAC), Arizona (Figure 1). This dataset was acquired on July 27, 2001. IKONOS data acquired on July 26, 2001, were used for target validation purposes. The cross-track performance of the ALI 10-meter panchromatic band was analyzed using the Lake Pontchartrain Causeway, Louisiana (Figure 2). The ALI data used for this analysis were acquired on September 20, 2001. The results of this analysis were compared to published results for the Landsat 7 Enhanced Thematic Mapper Plus (ETM+), which also used the Causeway. The in-track performance of the ALI 10-meter panchromatic band was analyzed using the same Maricopa data used for the multispectral bands.

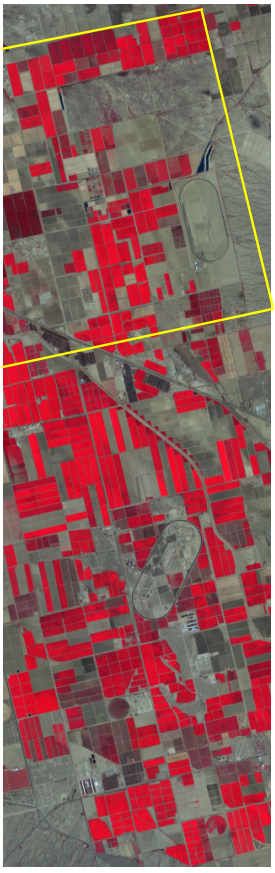

Figure 1. Maricopa Agriculture Center was used to characterize performance of ALI multispectral and pan (in-track) bands. IKONOS was used for target validation

Figure 2. Lake Pontchartrain Causeway was used to analyze the ALI 10-meter panchromatic band in the cross-track direction. These results were compared to the spatial response of ETM+.

The agricultural fields at Maricopa are oriented in a north-south and east-west pattern and formed angles of 13.08° with the ALI in-track and cross-track directions. This inclination of the fields to the EO-1 orbit provided sub-pixel sampling across the target. Results indicated that there was a 20% broader spatial response in-track compared to cross-track for ALI's multispectral bands. This is probably due to integration time smear in-track.

The Louisiana causeway target used to evaluate ALI's panchromatic band consists of a double-span bridge, each span 10 meters wide and with a center-to-center separation of 24.4 meters. This separation was large enough to allow two separate spatial response measurements. The angle between the causeway and the ALI data was 4.1949°, resulting in a sub-pixel cross-track sample increment of 0.0733 ALI pixels. The in-track analysis of the panchromatic band was done using the east-west berms at Maricopa.

Results indicated that the measured cross-track on-orbit MTF was about 0.1 higher at the Nyquist frequency (0.5 cycles/pixel) than pre-launch data for sensor chip assembly (SCA) 4. The cross-track spatial response Full Width Half Maximum (FWHM) value was found to be 1.3 pixels (13-m) and the cross-track MTF at 0.5 cycles/pixel, corrected for the target, was found to be 0.31. These values compare to 1.28 pixels (19.2-m) and 0.28, respectively, for ETM+ as reported by J. Storey in an earlier analysis.

A comparison of in-track and cross-track ALI spatial response calibration showed an expected lower on-orbit performance in-track. The panchromatic band in-track, on-orbit MTF was measured to be about 50% lower than the cross-track MTF at the Nyquist frequency. As in the case of the multispectral bands, this is consistent with in-track integration time smear. Results from this on-orbit characterization of the ALI multispectral and pan bands are somewhat different from pre-launch measurements and models developed by Lincoln Lab, but are consistent in terms of lower response in-track compared to cross-track. A detailed comparison of pre-launch and on-orbit results is in progress.

EO-1 Ice-Sheet Investigations
Robert Bindschadler

A series of investigations has validated the utility of EO-1's Advanced Land Imager (ALI) and Hyperion sensors for optical imagery in glaciological applications. These instruments have been used to investigate several ice-sheet phenomena that could not be investigated successfully with other remote imaging sensors. ALI multispectral bands were used to discriminate between clouds and snow and to measure flowstripe relief on ice shelves. The ALI panchromatic band was used to detect sastrugi (snow dunes). Hyperion hyperspectral capabilities were used to resolve and map snow grain size and determine albedo for ice sheets. Hyperion images of the Greenland ice sheet were also used to characterize errors in Hyperion's visible and near infrared (VNIR) and shortwave infrared (SWIR) detector arrays.

Cloud-Snow Discrimination

Discrimination between clouds and snow has been a problem with satellite optical imagery ever since the technology was first introduced because clouds and snow are both very bright and have similar spectral signatures. The problem is most acute over ice sheets where the surface provides little texture. ALI data were used to develop a methodology called "shadow matching" that can discriminate between clouds and snow. Shadow matching, which is available for any sensor with high enough resolution, detects a cloud's shadow, which appears darker than the cloud it borders. Areas of snow, although similar in brightness to clouds, do not have shadows. Other dark images, such as rocks, do not have shadows. Figure 1 depicts this methodology.

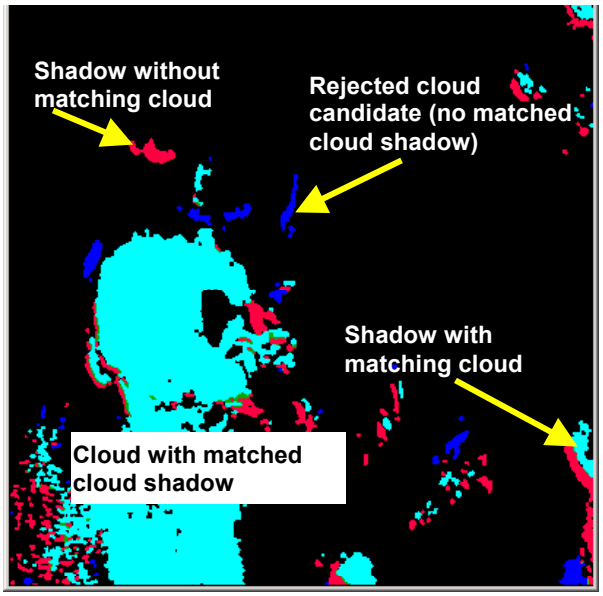

Figure 1. Cloud detection using shadow matching.

Flowstripe analysis

Flowstripes are topographic ridges generated by ice flow. The topographic relaxation of the flowstripes depends on its deformation and flow and is related to the length of time since the ice went afloat. The shape and trajectory of flowstripes offer clues to ice flow history. Photoclinometry applied to ALI images provides quantitative measurement of flowstripe relief (Figure 2).

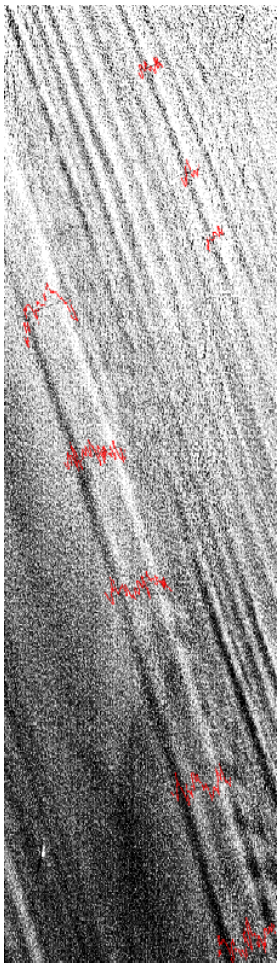

Figure 2. ALI flowstripe image. Profiles, shown in red, indicate brightness variations across the flowstripes.

This study analyzed flowstripes from the Amery Ice Shelf in Antarctica using ALI-derived measurements. When compared to similar data obtained through Landsat's Enhanced Thematic Mapper (ETM+) sensor, ALI permitted better discrimination of surface features that allowed for improved flow interpretation and velocity determination. This was due to ALI's improved radiometric resolution, which is approximately an order of magnitude better than that of ETM+.

Sastrugi Detection and Tracking

The ALI panchromatic band's ability to detect and track sastrugi was a newly discovered capability. Tracking sastrugi, which are windblown snow dunes typically less than 10 meters across and 1 meter in height (Figure 3), is valuable because it could greatly expand satellite measurements of ice-sheet surface motion.

Figure 3. Sastrugi have an eerie beauty.

Tracking sastrugi requires that the sastrugi features, which are individually smaller than a pixel, produce unique patterns at a macro-pixel scale. It also requires that these patterns persist over "meaningful" time scales.

ALI's increased radiometric resolution provides a signal-to-noise ratio (SNR) sufficient to detect the unique patterns produced by sastrugi fields. The unique patterns that persist over time allow investigators to track the movement of the sastrugi. ETM+, on the other hand, has a poorer SNR, leaving the sensor unable to detect subtle patterns of reflectance variation and thus unable to track the movement of sastrugi fields.

Figure 4 below shows ALI images of sastrugi fields for February 20 and October 2, 2001. The majority of the region is covered with sastrugi adjacent to the crevassed margin of an Antarctic ice stream (upper left). The three images at the right show the cross-correlation results between the two ALI images using correlation chips of different sizes. The leftmost correlation image uses the smallest chip size and has poor results except for the crevassed ice stream margin. The middle correlation image uses a larger correlation chip size, resulting in better cross-correlation. The rightmost image uses the largest correlation chip size, and the increased number of bright pixels in this image indicates that it is possible to track sastrugi over many months.

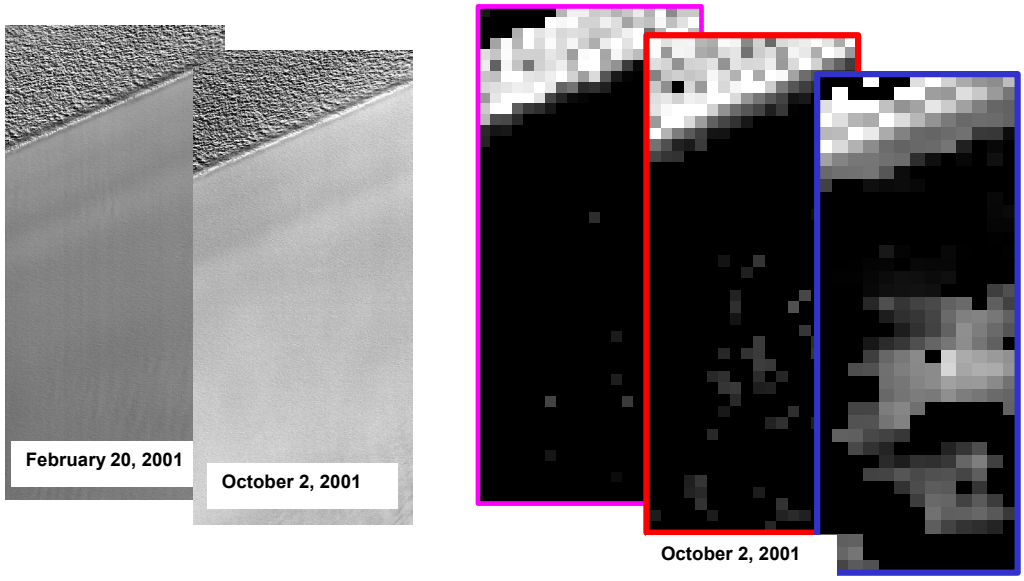

Figure 4. Sastrugi image cross-correlation with sub-image areas of varying-sizes.

Surface albedo calculations

The EO-1 Hyperion has been used to resolve and map variations in snow grain size over large regions of the East Antarctic Plateau. This contributes to improved calculations of broadband surface albedo for ice sheets, an important component of surface energy balance. The Hyperion was also used to map snow grain size over Greenland and to compute spectral albedo using the ice absorption feature from the Hyperion image and the Radiative Transfer Model (Figure 5). This results in a more accurate determination of albedo ($\pm$2%) than previously available.

Figure 5. Hyperion image of Greenland, May 20, 2001.

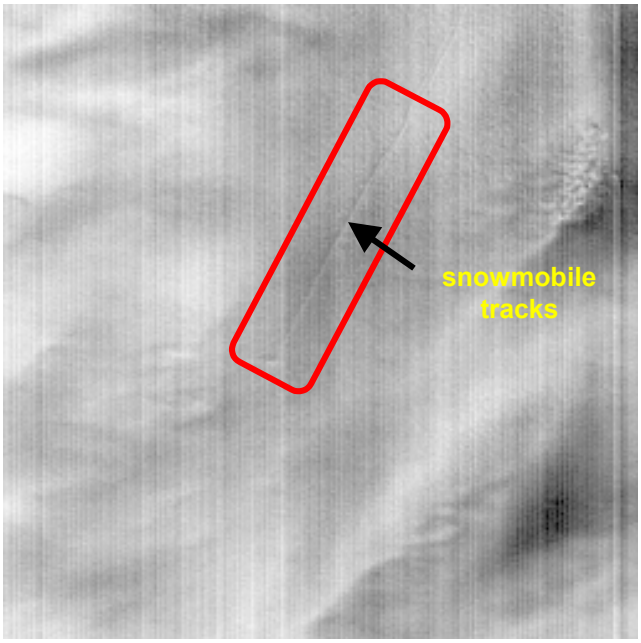

Hyperion detector array errors

Investigators used Hyperion images of the Greenland ice sheet to characterize errors in the Hyperion VNIR and SWIR detector arrays. The homogeneous character of the ice sheet over time underscored the usefulness of ice sheets as targets for on-orbit sensor characterization. The ice sheet's uniformity and stability in terms of surface slope and surface reflectivity allowed spatial variations to legitimately be attributed to detector variability of the Hyperion instrument rather than to variations in the landscape.

The analysis of two images of an extremely homogeneous region, taken on July 7, 2001, and August 8, 2001, revealed variability of the Hyperion detector arrays across the swath direction, in the spectral dimension, and in the temporal dimension. This variability caused striping in the images. The striping could be almost completely removed by applying appropriate corrections to the specific scenes that were available from another image that was taken either very soon before or after the scene requiring correction. Figure 6 shows images of ice sheets derived from Hyperion data used to determine detector errors for three Hyperion bands.

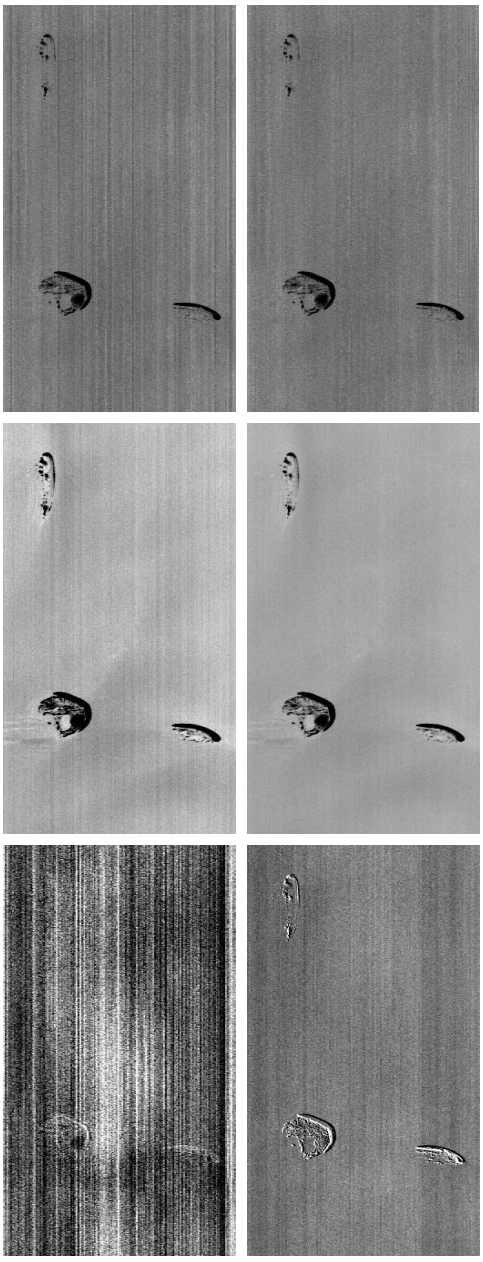

Figure 6. Correction of a short (526-line) portion of Hyperion data of the ice sheet near to the region used in the determination of detector errors. Band 80 (942.8 nm) is shown. The upper pair is the uncorrected (left) and corrected image (right); middle pair is MNF band 4; lower pair is MNF band 11.

Conclusions

The ALI and Hyperion sensors aboard the EO-1 have proven useful a variety of glaciological applications. These instruments have successfully investigated several ice-sheet phenomena that could not be examined effectively with other remote imaging sensors. ALI multispectral bands discriminated between clouds and snow and measured flowstripe relief on ice shelves. The ALI panchromatic band detected sastrugi. Hyperion hyperspectral capabilities resolved and mapped snow grain size and determined albedo for ice sheets. Hyperion images of the Greenland ice sheet characterized errors in Hyperion's visible and near infrared (VNIR) and shortwave infrared (SWIR) detector arrays. Methods were devised to correct the errors.

Investigations in the Okavango Delta Using EO-1 Data

Melba Crawford, Amy Neuenschwander, and Susan Ringrose

A series of investigations that relate to the performance of EO-1 instruments have centered on the seasonal flooding of the Okavango Delta in northwestern Botswana. The extreme inaccessibility of the area makes it an ideal candidate for the use of remote sensing to map the annual flooding and land cover in the region (Figure 1)

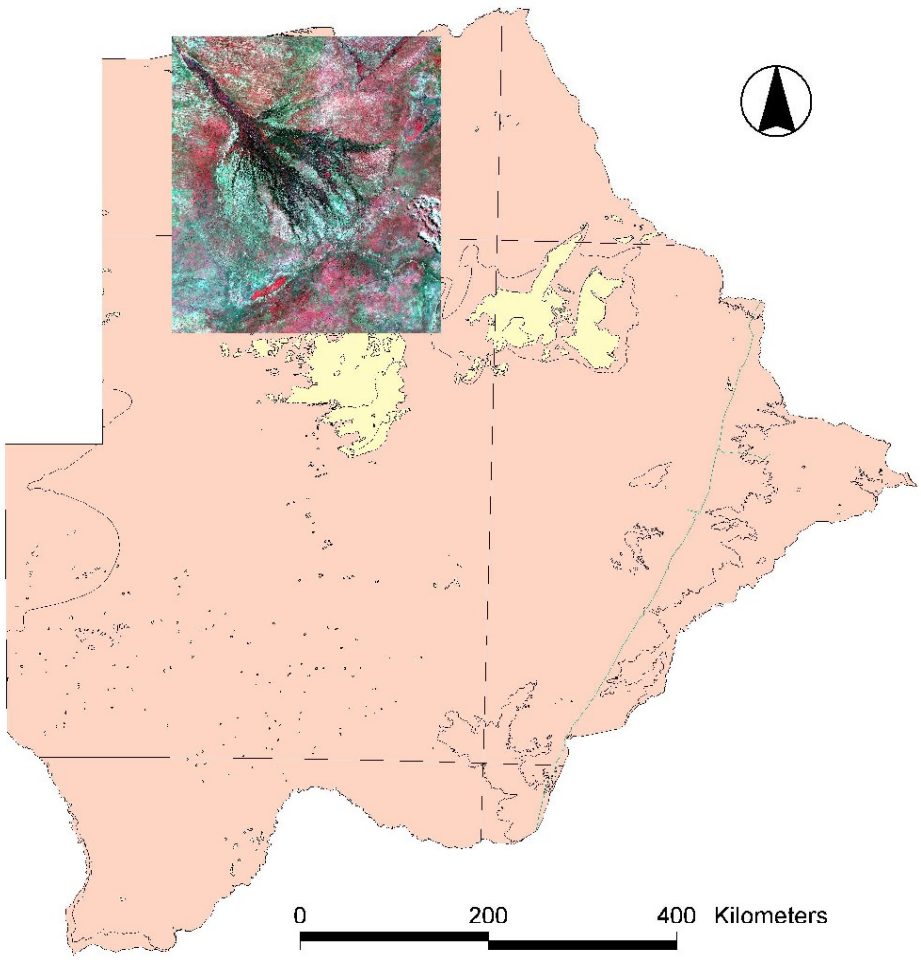

Figure 1. Okavango Delta of Botswana as seen in Landsat ETM+ data.

The Okavango Delta is the world's largest inland delta. It is fed by the Okavango River, which originates in Angola's western highlands (Figure 2). The catchment area for the Okavango River lies in three countries (Angola, Namibia, and Botswana, although the drainage flow from Namibia is completely dry) and has a total area of approximately 325,000 km^2. The Delta extends 250 km along its radial axis and extends over 22,000 km^2 in area. The floodwaters require approximately nine months to travel from their source in Angola to the bottom of the Delta because of the extremely low topographic relief. Interestingly, the annual flooding occurs during the area's dry season (June through August) when most days are cloud-free and suitable

for acquiring data from optical sensors such as MODIS, Landsat TM, and EO-1 ALI and Hyperion.

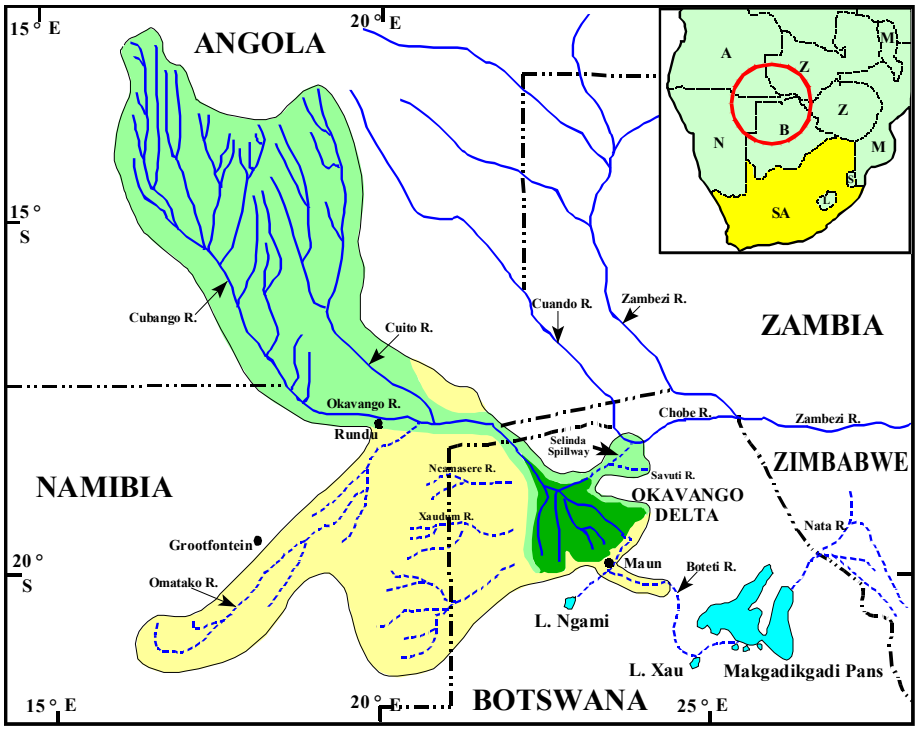

Figure 2. Okavango Catchment

A field campaign, conducted in March 2001 by the University of Texas Center for Space Research (CSR) in conjunction with the University of Botswana Harry Oppenheimer Okavango Research Center (HOORC), focused on a portion of the Delta known as Chief's Island (Figure 3). The land cover in this area includes swamplands, grasslands that are seasonally flooded, as well as woodlands that are not flood prone. Seasonal swamps, which cover ~4,700 km^2, are areas of grasslands that flood annually. Occasional swamps flood in one-to-ten-year intervals rather than annually. These areas occupy ~11,000 km^2 and are comprised primarily of grasslands, but also include shrubs and small woody plants. A focus of this study was to characterize the annual flooding by mapping the spatial patterns within the lower Delta as well as to identify small-scale responses of vegetation. The interannual flow variability in the Delta is primarily due to alluvial processes but appears to be a function of annual variability in vegetation within the floodplain, hippo activity and burning practices, as well as of the amount of annual rainfall. The spatial and temporal variation of flooding of these channels is important for managing the competing uses of this scarce resource.

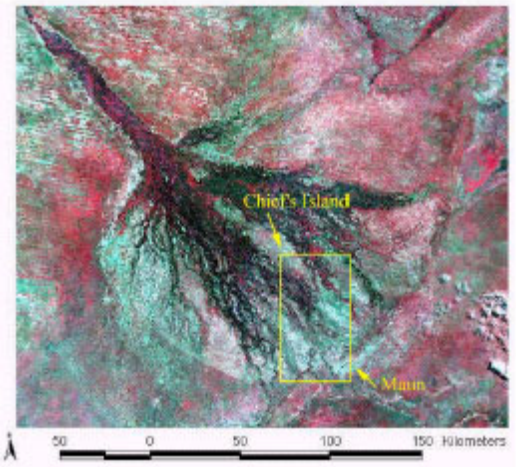

Figure 3. ALI coverage of Chief's Island and the lower Okavango Delta

The investigations used data acquired by the Advanced Land Imager (ALI) on five dates: May 31, June 16, July 11, and August 19, 2001 (Figure 4) and September 16, 2002. The study focused on the following:

- Characterizing vegetation responses to flooding and seasonal variations in spectral responses of vegetation,
- Determining the spectral response of riparian forest to seasonal flooding as a potential indicator of increased evapotranspiration rate in the Delta, and
- Comparing the improved capabilities of the ALI multispectral bands relative to the Landsat Enhanced Thematic Mapper (ETM+) for discriminating land cover types.

Further analyses, using only imagery acquired on May 31, investigated the following:

- Potential improvement of hyperspectral data from Hyperion for discriminating land cover,
- Viability of configuring application-specific multispectral sensors from hyperspectral sensors,
- Capability of new algorithms for classifying complex land cover environments, and
- Methods for mitigating artifacts in ALI and Hyperion data and the impact of these artifacts on classification results.

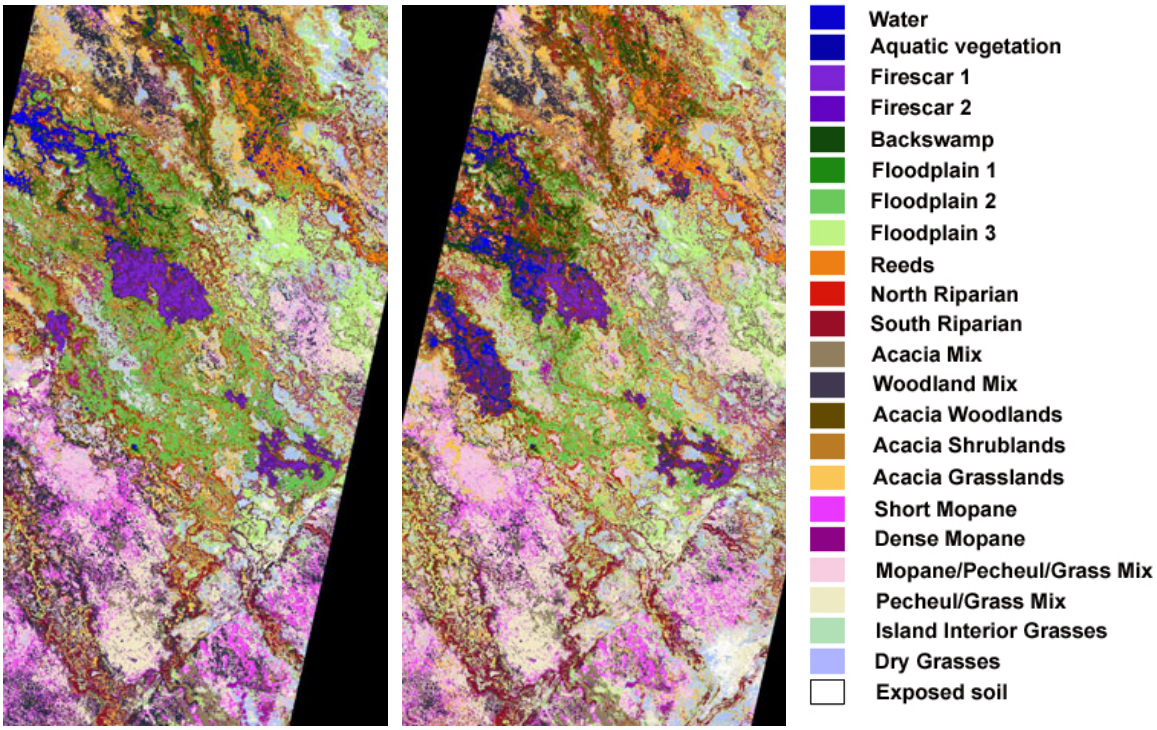

(a) May 31, 2001

(b) June 16, 2001

(c) July 11, 2001

(d) August 19, 2001

Figure 4. ALI 2001 Classified Data.

A Bayesian Pairwise Classifier (BPC) algorithm with feature selection was used to classify land cover into the 23 categories listed in Figure 4. The feature selection method provided one means of investigating the contribution of the new bands in ALI relative to those of ETM+ and typically performed well when classes were difficult to discriminate due to similar spectral signatures. Overall classification accuracies for ALI were consistently higher (~83%) compared to ETM+ (~68%), and results were also superior in terms of visual, qualitative evaluation. This improvement in the classification is attributed to the higher signal-to-noise ratio (SNR) and the increased dynamic range of the ALI data. ALI also yielded improved fine scale mapping of the flood channels relative to ETM+.

This spatial variability of the flooding patterns and its impact on biota of the Delta is not well understood, but is critical for management of the ecosystem. The variability in inter-annual variation in flood patterns is clearly demonstrated in Figure 5 that contains corresponding flood cover from 2001 and 2002. The total area of flooded lands in 2001 was 257 km^2, whereas in 2002, only 200 km^2 was flooded in this portion of the Delta.

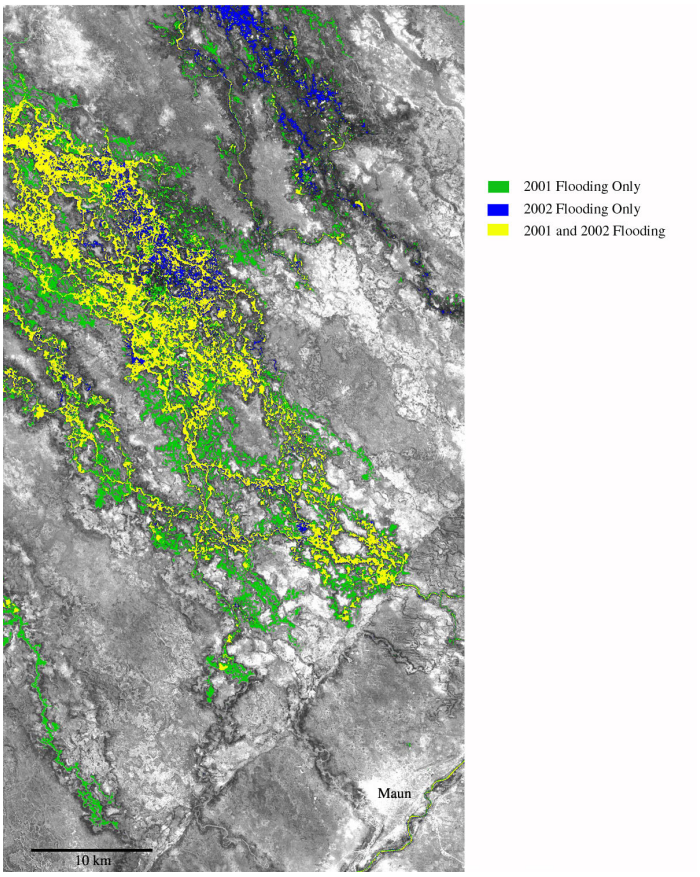

Figure 5. Flood cover for lower Delta in 2001 and 2002.

EO-1 also provided the first high-resolution sequence of remotely sensed data for studying the response of woodland species including the riparian forest. Riparian forest is thought to be a potential contributor to the high evapotranspiration rate in the Okavango. Figure 6 compares the spectral responses of many woodland species in May 31, 2001 and July 11, 2001. Although the

woodland classes do not exhibit greening, there is a response in the short-wave infrared (SWIR) of shrubs, short mopane, and woodland mix. While the signatures for some classes are not well understood, the increase in the reflectance of the short mopane class in the July 11 is due to the fact that the short mopane has begun to drop its leaves by mid-July and the soil background is now showing through.

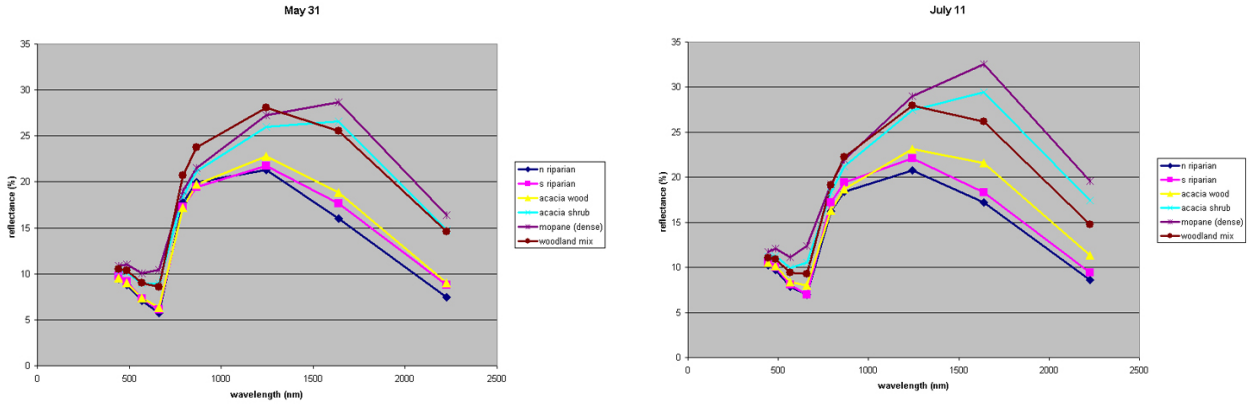

Figure 6. Spectral signatures May 31, 2001 woodland classes (left) and July 11, 2001 woodland classes.

The improved resolution and increased SNR of the ALI panchromatic band relative to that of ETM+ is well demonstrated in Figure 7 which contains scenes over the town of Maun acquired on August 12 and August 19, 2001 respectively. It also helped delineate boundaries of land cover types and discrimination of boundaries of trona islands located in the seasonal swamps (Figure 8).

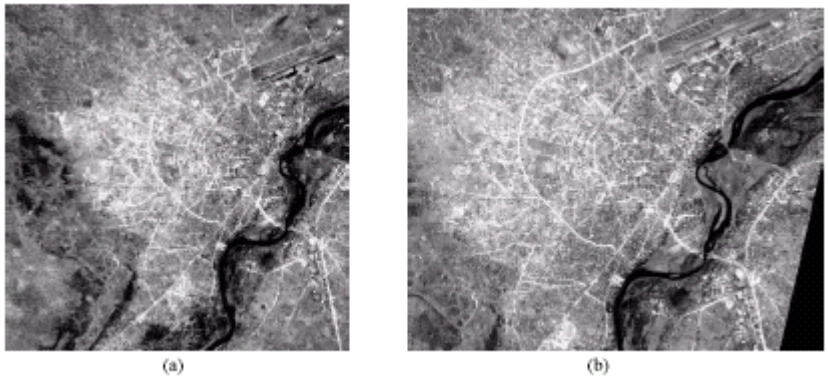

Figure 7. Panchromatic images from ETM+ (a) and ALI (b).

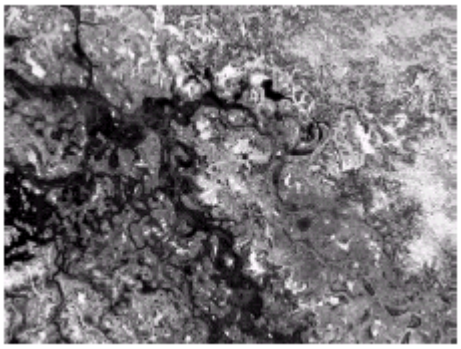

Figure 8. ALI panchromatic image of trona islands in seasonal swamp.

In addition to mapping the flood extent in the lower delta, ALI and Hyperion data were compared on the May 31 acquisition to determine whether improved accuracies would be achieved using the hyperspectral sensor. The May 31 data were acquired at the onset of the flooding season; thus the vegetation within the Hyperion swath was more diverse and less inundated than later in the year. To date, this type of direct comparison between multispectral and hyperspectral sensors has not been possible as hyperspectral sensors prior to the EO-1 have been flown on airborne platforms flown at lower altitudes, and acquisitions have not been simultaneous. Overall, classification accuracies obtained from analysis of Hyperion data (~73%) were slightly lower than those obtained using ALI (~82%), although discrimination of some classes that exhibited distinct fine feature signatures was superior to that of ALI. Of particular note was the over- classification of the riparian category in ALI results since the riparian ecotone is thought to play a critical role in the evapotranspiration process in the Delta. Hyperion data provided improved discrimination of these classes (see Figure 9). The unexpected overall lack of improvement from Hyperion was attributed to problems with uncompensated streaking in the hyperspectral data and to signatures of mixed classes, for which classification cannot benefit from the narrow hyperspectral bands. Classification accuracies using synthesized ALI data (~75%) generated from Hyperion bands were comparable to those for data acquired from the original ALI bands in terms of classification, thus lending credibility to the practice of creating "on the fly" multispectral sensors from hyperspectral data.

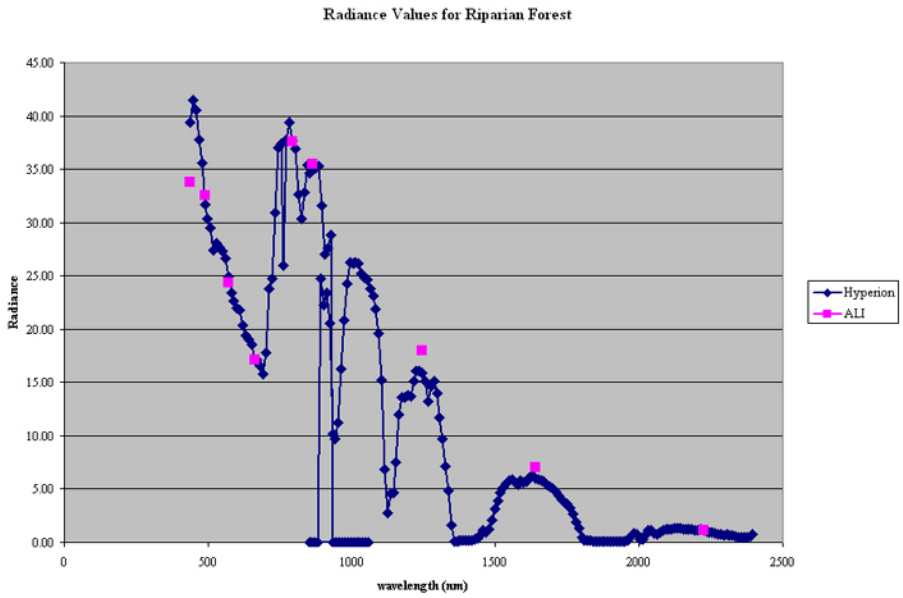

Figure 9. Comparison of Spectral Information between ALI and Hyperion.

Ongoing research is focusing on analysis of data acquired during the 2002 flooding season and on field verification of land cover mapping. Collaborative research to improve digital elevation models and incorporate them into the analysis is also underway. Finally, results obtained from ALI and ETM+ are being related to MODIS data for up scaling results and providing a higher temporal resolution capability for monitoring the ecology of the Delta region.

Quantitative Analysis of Hot Spots Using EO-1 and Landsat 7
Luke Flynn

The objectives of this investigation were to compare the capabilities of the Earth Observing-1 (EO-1) Advanced Land Imager (ALI) and Hyperion instruments and the Landsat 7 Enhanced Thematic Mapper (ETM+) to monitor active volcanic eruptions and fires and to assess the merits of using spacecraft flying in formation over highly temporally variable targets. This capability would allow for (1) the evaluation of Hyperion and ALI spectral bands for incorporation into a Landsat-type follow-on instrument, (2) greatly improved maps of thermally emitted energy as a result of using improved EO-1 technology, and (3) the ability to study short-term changes associated with eruptions and forest fires.

EO-1 represents a unique opportunity to study the characteristics of high-temperature thermal anomalies including lava flows and forest fires. Previous attempts at measuring the thermal output of lava flows and forest fires at 30 meters resolution have been limited by instrument characteristics of the earlier Landsat 4 and 5 Thematic Mapper (TM). Frequent saturation problems with Landsat TM bands 5 and 7, which are sensitive to high temperatures, left the most interesting parts of the lava flows unstudied. While the qualitative aspects of these flow studies were tantalizing in that they showed that 30 m data can be used to assess geologic hazards from effusive eruptions, the limited number of relevant spectral channels of the TM precluded more quantitative assessments using more than pixel integrated temperatures. Similarly, a study of the differences in spatial temperature distribution between flows and fires demonstrated that both anomalies could have similar maximum temperatures while fires cool more rapidly than lava flows. However, TM data were insufficient to produce flux density maps of the fire data because of the inadequate dynamic range in the few relevant near-IR spectral channels.

In contrast, Hyperion and ALI represent a tremendous advance for high-temperature studies of volcanic eruptions and forest fires because:

- The number of spectral channels available with Hyperion (220 channels between 0.4μm – 2.5μm) is useful for solutions of multi-component models that would accurately determine the sub-pixel temperatures and spatial extent of anomalies.
- Comparisons of results derived from Hyperion, ALI (with its critical band 5p at 1.2μm - 1.3μm), and Landsat 7 ETM+ will allow an assessment of instrument capabilities from future Landsat-type sensors.
- Saturation at near-IR wavelengths is not as disastrous for Hyperion or ALI as it was with the TM, because channels at shorter wavelengths (i.e., 1.2μm - 1.3μm) can be used to make temperature and area calculations.
- Better sub-pixel solutions of hot spots will yield more accurate estimates of emitted energy for both lava flows and forest fires and also a basis for determining the requirements for future Landsat sensors.

This investigation examined the sensitivity of the EO-1 instruments to high-temperature thermal anomalies such as lava flows and forest fires focusing on Mt. Etna, Sicily, as the primary study site. Covering the same spectral region as the instruments aboard EO-1 (0.4μm - 2.5μm), the FieldSpec FR system developed by Analytical Spectral Devices was also used to provide simultaneous ground-truth. In addition, a FLIR (infrared) camera collected very high spatial resolution observations of active lava flows that were then used to model the number of thermal

components present. The study showed that the number and placement of channels offered by Hyperion and ALI allowed investigators to assess more accurately the distribution of thermal radiators within a pixel than was available with Landsat ETM+.

It was expected that EO-1 data would yield much more detailed flux density maps and mass flux calculations than those derived from earlier Landsat TM data, which, nevertheless, have been particularly useful in assessing volcanic hazards. Further, assessment of ETM+, ALI, Hyperion, and ASTER data (flying on the TERRA satellite in formation with EO-1 and Landsat 7) would provide information about the short-term variability of eruptions and forest fires, which would be used to suggest constraints for the temporal distribution of successive measurements for future formation flying missions.

EO-1 was launched successfully in November 2000. By spring 2003, 10 volcanoes worldwide had been imaged with Hyperion and ALI. Images from Mt. Etna that showed a spectacular eruption during July 2001 were used most heavily in this investigation. Sixteen images were collected including two nighttime images. Of these, seven were good-quality images.

Volcanoes with lava flow activity

Lava flows that can easily travel tens of kilometers from their source vents in a matter of hours represent the most easily recognized volcanic activity from a satellite perspective. A February 14, 2000, Landsat 7 image acquired of Kilauea in Hawaii showed that lava flow fields and the underground tubes supplying them with lava can be mapped with ETM+. More importantly, the 15m/pixel ETM+ panchromatic band was used to map fresh (less than a few hours old) lava flows on the basis of their surface reflectance, not thermal radiance. However, ETM+ has suffered from the fact that usually only two bands detect emitted thermal radiance from the flows with the remainder of the bands suffering from saturation (due to higher thermal radiances that cannot be accommodated within the dynamic range of the detector) or a lack of anomalous radiance above the inactive background pixels. Both Hyperion and ALI provide more near-infrared bands that are necessary for accurate temperature and area determinations of active lava flows.

Hyperion observations of the Mt. Etna volcano collected on July 13, 2001, showed characteristic effusive lava flow activity typical of persistent effusion from the southeast cone (Figure 1). Lava flows and active vents containing molten lava with temperatures of up to 1080°C appear in the image as bright red and yellow colors. The inset to Figure 1 shows the four active craters that comprise the Mt. Etna summit complex. The red, green, and blue composite image was created using Hyperion bands 213, 152, and 32, respectively. In the west central portion of the inset, an active vent at the bottom of the Bocca Nuova crater is apparent. Approximately, 200 - 300 meters to the northeast is an active vent within La Voragine crater, while another 300 meters to the north, an active vent within the northeast crater is apparent. A large 300 m – 500 m-diameter anomaly about 700 meters southeast of La Voragine marks the location of the southeast cone of Mt. Etna. Lava flows issuing from fissures on the northeast side of the cone flowed to the northeast before turning east into the Valle del Bove. Lava flow appears to have been concentrated in a 600 m-long channel before flows bifurcated numerous times to form a compound flow field extending 1.5 km east in this image. A plume of ash and volcanic aerosol originates from the Bocca Nuova and disperses to the southeast.

Figure 1. Mt. Etna before the main eruption began, July 13, 2001.

Collected nine days later, on July 22, 2001, a second Hyperion image (Figure 2) revealed a much more active and potentially disastrous eruption of Mt. Etna. The pointing capability of the instrument allowed investigators to obtain multiple high-resolution images of this new flank eruption. On July 17, 2001, a much larger and more vigorous eruption had begun that involved lava flow activity on at least four separate active fissures. Again, in the west central portion of the July 22 image, a cluster of three yellow and red dots can be seen to mark the locations of active vents within the Bocca Nuova, La Voragine, and the southeast cone; however, at that time, the northeast crater was obscured by volcanic aerosols. The northernmost fissure had started to erupt on July 20, 2001, only two days before the Hyperion overpass. The July 22 image showed the 1.5 km-long lava flows from this fissure moving southeast at the base of the steep cliffs that mark the northern edge of the Valle del Bove. Approximately 360 meters to the southeast of the southeast cone a longer lava flow is apparent. These are flows from another fissure that had opened on July 17 to feed flows that first moved southeast before encountering the back wall of the Valle del Bove and being deflected in a more easterly direction. Two other fissures had also opened on July 17 to the south of the Etna summit complex and had fed lava flows that moved in a southerly direction. At the time the July 22 image was recorded, these two flows had advanced 2.7 km and 5.9 km, respectively, in the general direction of the town of Nicolosi. The end of the lava flow field is apparent as the more diffuse red and yellow anomaly south of a white cloud that obscures part of the flow. These fissures also erupted a large amount of ash and volcanic aerosols that are apparent in the image.

Figure 2. Mt. Etna eruption, July 22, 2001, acquired with Hyperion. The bands are equivalent to Landsat 7 ETM+ bands 7, 5, and 3 in red, green, and blue.

Vigorous, opening phases of flank eruptions on Mt. Etna were characterized by intensely hot molten lava flowing in open channels. It is certain that this vigorous eruption caused the infrared channels of Hyperion to malfunction, which is why the active lava flows were mirrored by a less intense radiance echo located roughly 300 meters to the west of the main lava flows. Discussions with researcher Pamela Barry led this investigative team to believe that it may be possible to reconstruct the original signal (above the saturation value for that spectral band) using the saturated pixel radiance and the radiance echo for that pixel. Essentially, the Hyperion data were collected in analog form. When they are converted to a digital signal, anything above a threshold value gets a saturation value. However, the remainder of the analog signal was recorded as a radiance echo 11 pixels west and one pixel south of the original saturated pixel. Thus, it may be possible to reconstruct the original analog signal using the radiance echo. This would enable calculation of higher temperatures and fractional areas for very high temperature lava channels and other areas prone to radiance saturation.

Spectra from this eruption are being evaluated. Obtaining spectra from Hyperion data was not too straightforward because of the data shifts required to align spectra. A shift of even one pixel will result in erroneous temperatures, as the pixels must be co-located in order for Planck curves to be fitted to the spectra. Spectra taken over active lava flows saturated in a number of areas. Temperatures were then modeled from those wavelengths that were not saturated. Investigators are developing an automated method to rapidly process large areas of the lava flow field at one time. If the attempt to reconstruct saturated pixel values is successful, this capability will greatly enhance the capacity to automate the creation of radiant energy maps using Hyperion data. Researchers can then compare these results with those obtained with Landsat 7 ETM+ and ALI.

ALI - Landsat 7 ETM+ comparison of temperature retrievals over active Etnean lava flows
Using near simultaneously acquired Landsat 7 ETM+ and EO-1 ALI data, investigators also assessed the relative radiant responses over active lava flows from the Mt. Etna July/August 2001 flank eruption. Investigators assessed the extent of saturation between the two instruments and by using the dual band method of extracting sub-pixel thermal information on the resulting lava flows. This dual band method simplifies lava flows as a two-component thermal surface: a hot incandescent core exposed through cracks in the crust and a cooler crust. Assessing the extent of saturation and use of the dual band method allowed the investigators to demonstrate that ALI represented an improvement over ETM+ in the current ability to assess temperatures of hot active lava flows. This was true because: (1) The extra spectral channels provided by ALI complemented the current shortwave infrared (SWIR) channels on ETM+ by providing a greater number of two-channel combinations for input into the dual band method. Thus, dual-band temperature solutions were available for a greater range of lava flow types than previously possible using the two channel combinations available on the ETM+. (2) The ALI instrument was less susceptible than ETM+ to saturation in the SWIR range, especially when using channels 5, 5p, and 4p. (3) The greater radiometric sensitivity of ALI's 12-bit electronics coupled with a significantly lower signal to noise ratio (SNR) aided in obtaining successful dual band solutions.

The investigators demonstrated the extensive application of the dual band method of extracting information on sub-pixel resolution hot spots in ETM+ and ALI data over active lava flows. The ability to obtain a successful solution requires the use of unsaturated instrument data within the SWIR range. The extensive saturation observed within ETM+ channels 7 and 5 have often precluded the use of this method. Similar levels of saturation were also found in ALI channel 7 that prevented the use of this channel in the dual band calculations. ALI channel 5 also displayed saturation over the most active flows and vents imaged within the study area. However, because ALI channel 5 can tolerate a higher level of thermal radiation before it saturates, it exhibited substantially less saturation than the equivalent ETM+ channel 5. The saturation of ALI data also was not readily apparent when using processed Level 1R data. Data based on Level 0 processing was used to identify areas where ALI was saturating. ALI channel 5p, placed in the SWIR range between ETM+ channels 4 and 5, saturated only over the most active regions within the study area. ALI channel 4p showed no saturation but was sensitive to the most active lava flows.

The ALI instrument demonstrated that it is possible to gain dual band estimates of sub-pixel detail over hot active lava flows that are not available or reliable when using ETM+ data because of the addition of the two extra SWIR channels, 5p and 4p. Different band combinations available using unsaturated ALI data are sensitive to differing P_H & T_C (basically area and

temperature) combinations, providing coverage for a range of lava flows from cooling stagnating flows to flows close to the vent using channel combinations at progressively shorter wavelengths. This was not possible with ETM+ because the relevant channels do not exist. The ease with which ETM+ channels 7 and 5 saturate over such flows as those within the study area prevented successful dual band solutions.

Conclusions:

The increased SNR of the ALI and better radiometric sensitivity coupled with the extra SWIR channels has produced an instrument that is very capable in terms of remote sensing of active lava flows. If ALI technology is incorporated into a replacement Landsat instrument with a fully populated focal place, the resulting data should prove highly useful in the analysis of active lava flows to an extent not possible before. The study also showed that the number and placement of channels offered by Hyperion and ALI allow investigators to assess more accurately the distribution of thermal radiators within a pixel than was available with Landsat ETM+.

Retrieval of Surface Reflectance and Estimation of Forest Leaf Area Index (LAI) Using Hyperion, ALI, and AVIRIS

Peng Gong, Greg Biging, and R. Pu

Objectives

The objectives of this investigation were to develop a simple atmospheric correction method; map leaf area index (LAI), study vegetation indices (VIs), and extract red edge optical parameter for estimating forest LAI with the EO-1 Advanced Land Imager (ALI) and Hyperion and with the Airborne Visible/Infrared Imaging Spectrometer (AVIRIS); examine the capabilities of the three sensors for extracting LAI information; and compare different VIs constructed from all possible Hyperion bands and red-edge parameters for LAI estimation.

Study Site and Datasets

Two study sites were used in Patagonia, Argentina, that were located in a flat, semiarid region. The study area had many patches of conifer forest plantations of different species of pine trees as well as some broad-leaf species and shrubs and grasses.

On March 27-29, 2001, field reflectance measurements were obtained for several targets using ASD Field Spec®Pro, and 70 LAI measurements were taken. On March 27, 2001, ALI and Hyperion measurements were acquired at a spatial resolution of 30 meters. AVIRIS data at a spatial resolution of 3.6 meters were acquired on February 15, 2001. Because of overcast conditions at one study site, data from only one of the two sites (the north site) were used for the analysis (Figure 1).

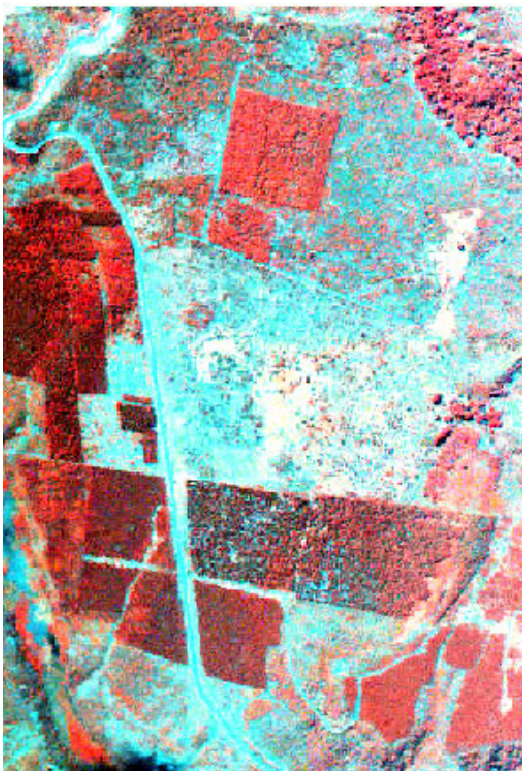

Figure 1. Part of the AVRIS image over the selected study site in Patagonia, Argentina.

Atmospheric Correction and LAI Mapping

Atmospheric correction was obtained by means of a radiative transfer model. The model was applied to sensor data in which three total radiances were simulated using MODTRAN4 to obtain improved pixel-based surface reflectance. Ground spectrometer data were also used to modify the retrieved surface reflectance images.

Using the improved retrieved surface reflectance images from the ALI, Hyperion, and AVIRIS sensors, LAI was estimated and mapped by following a set of procedures that involved extracting pixel values at 32 LAI measured plots, performing general correlation analysis of spectral bands with LAIs, and performing regression analysis on six bands selected from the total number of bands available for each sensor. Results were compared using only data from these six bands for each sensor.

The effectiveness of the procedures was evaluated using the following criteria:

1. Multi-correlation coefficient, R^2, of the LAI prediction model.
2. Overall average accuracy of LAI prediction accuracy of training and test samples.
3. Visual examination of LAI maps.

Results indicated that AVIRIS had the highest correlation with LAI among the three sensors. Hyperion had the next highest correlation, and ALI had the lowest correlation. Figure 2 shows a pseudo-color composite from AVIRIS (upper left) and LAI maps for the three sensors. AVIRIS data experienced fewer atmospheric effects than the data from the other sensors, especially in the visible and near infrared (VNIR) region. Hyperion was especially problematic in this region because of its strong atmospheric scattering.

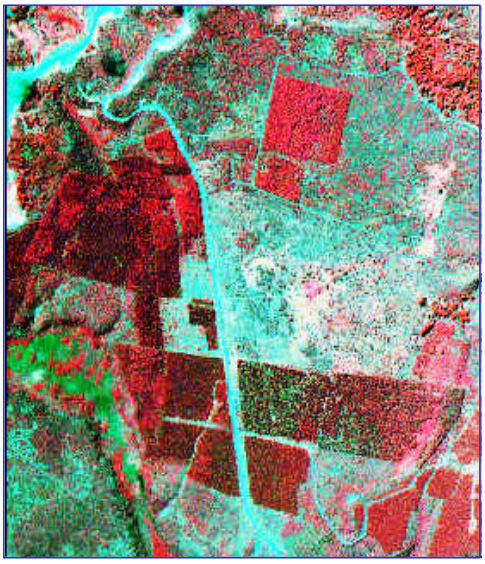

Pseudo color composite of AVIRIS.

LAI map from AVIRIS.

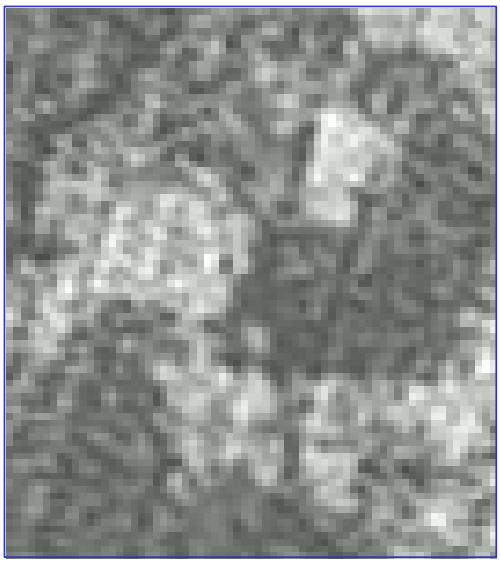

LAI map from Hyperion

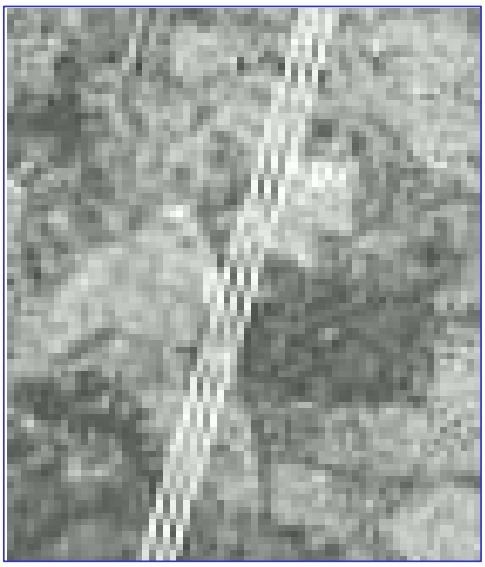

LAI map from ALI. The three white lines were from three ALI dead detectors.

Figure 2. LAI maps.

Conclusions

Investigators concluded that atmospheric correction is critical for hyperspectral data applications, especially for measurements in the VNIR region. Results indicated that the method of atmospheric correction used in this study holds promise but needs refinement. Results further indicated that retrieval of surface reflectance was the most successful for AVIRIS, followed by Hyperion and lastly by ALI. Mapped LAI results demonstrated that the procedure used in this investigation to map LAI can produce reasonable LAI maps, and that the LAI map produced with AVIRIS data was more reliable than the maps produced with Hyperion and ALI, which appear to have similar capabilities for LAI mapping. Hyperion in particular seems to have more potential for applications in the shortwave infrared (SWIR) region than in the VNIR region because the atmospheric effects are more pronounced on VNIR measurements. For imagery in the SWIR region, if atmospheric correction is carefully conducted, Hyperion has the potential to produce results similar to that of AVIRIS.

Estimating Forest LAI Using Vegetation Indices Derived From Hyperion Hyperspectral Data

Method

Pixel-based retrieved reflectance spectra from calibrated Hyperion images at the 32 LAI measurement plots were extracted from the image. One to four homogenous pixels were extracted and averaged for each LAI plot. The 12 VIs (Table 1) were applied to any possible pair of the 168 Hyperion bands. Note that red (R) bands and near IR (NIR) bands used for constructing one VI in Table 1 have been extended to all 168 bands. Consequently, for each pair of bands there are 12 VIs for each of the 32 LAI measurements.

For each of the 12 VIs, a linear correlation coefficient (R^2) was calculated between the VI and LAI measurement (32 samples). Because most LAI measurements are less than 5 in this study, a

linear R^2 is a suitable indicator for finding some important bands contributing to better correlation between a two-band index and the LAI. Since each VI in Table 1 could be constructed from any pair among the possible 168 bands, a linear correlation coefficient (R^2) matrix could be constructed. From the correlation matrices, hyperspectral bands with high correlation coefficients were examined.

Conclusions

Results indicate that many hyperspectral bands in the SWIR region and some in the NIR region have the greatest potential to form indices for LAI estimation. The most effective band wavelengths are centered near 820, 1040, 1200, 1250, 1650, 2100, and 2260 nm with bandwidths ranging from 10 to 300 nm (Table 2). These bands are controlled by plant leaf water content, yet the absorption features by other biochemicals such as protein, nitrogen, lignin, cellulose, sugar, and starch, may have indirect impacts. VIs derived from the R and NIR bands did not produce as high correlations with LAI as those with bands in the SWIR and NIR regions. Based on their high correlation with LAI measurements, the Modified Non-Linear Vegetation Index (MNLI), Simple-Ratio Vegetation Index (SRVI), and Normalized Difference Vegetation Index (NDVI) were recommended for use in environments similar to this study site for LAI estimation using satellite-based hyperspectral data.

Extraction of Red Edge Optical Parameters from Hyperion Data for Estimation of Forest LAI

Method

A correlation analysis was conducted between forest LAI and two red edge parameters: red edge position (REP) and red well position (RWP), extracted from reflectance image retrieved from Hyperion data. Field spectrometer data and LAI measurements were collected on the same day as the EO-1 satellite overpassed the study site in the Patagonia region of Argentina. They were extracted with four approaches: 4-point interpolation, polynomial fitting, Lagrangian technique, and IG (inverted-Gaussian) modeling.

Table 1. Summary of 12 two-band vegetation indices used in this analysis.

Index	Formula	Description	References (e.g.)
SR	ρ_{NIR} / ρ_R	Near-infrared / Red reflectance ratio (Simple Ratio VI). Related to changes in amount of green biomass, pigment content and concentration and leaf water stress etc.	Baret and Guyot, 1991; Tucher, 1979.
NDVI	$(\rho_{NIR}-\rho_R)/(\rho_{NIR}+\rho_R)$	Normalized Difference Vegetation Index. Related to changes in amount of green biomass, pigment content and concentration and leaf water stress etc.	Fassnacht et al., 1997; Smith et al., 1991.
PVI	$\frac{1}{\sqrt{a^2+1}}(\rho_{NIR}-a\rho_R-b)$ a = slope of the soil line, b = soil line intercept	Perpendicular Vegetation Index, orthogonal to the soil line. Attempts to eliminate differences in soil background and is most effective under conditions of low LAI, applicable for arid and semiarid regions.	Baret and Guyot, 1991; Huete et al., 1985.
SAVI	$\frac{(\rho_{NIR}-\rho_R)(1+L)}{(\rho_{NIR}+\rho_R+L)}$ L = a correction factor	Soil Adjusted Vegetation Index. L ranges from 0 for very high vegetation cover to 1 for very low vegetation cover; minimizes soil brightness-induced variations. L=0.5 can reduce soil noise problems for a wide range of LAI.	Huete, 1988; Leeuwen and Huete, 1996.

Index	Formula	Description	References (e.g.)
NLI	$(\rho_{NIR}^2 - \rho_R)/(\rho_{NIR}^2 + \rho_R)$	Non-Linear vegetation Index. Considers that the relationship between many VIs and surface biophysical parameters is often nonlinear, and NLI linearizes relationships with surface parameters that tend to be nonlinear.	Goel and Qin, 1994
RDVI	$(\rho_{NIR} - \rho_R)/(\rho_{NIR} + \rho_R)^{1/2}$	Renormalized Difference Vegetation Index. RDVI linearizes relationships with surface parameters that tend to be nonlinear.	Roujean and Breon, 1995.
MSR	$\frac{(\rho_{NIR}/\rho_R - 1)}{(\rho_{NIR}/\rho_R)^{1/2} + 1}$	Modified Simple Ratio. It can be an improvement over RDVI for linearizing the relationships between the index and biophysical parameters.	Chen, 1996.
WDVI	$\rho_{NIR} - a\rho_R$ a = slope of the soil line	Weighted Difference Vegetation Index. WDVI assumes that the ratio between NIR and R reflectances of bare soil is constant; it is related to PVI, but it has an unrestricted range.	Clevers, 1988; Clevers, 1991.
MNLI	$\frac{(\rho_{NIR}^2 - \rho_R)(1+L)}{(\rho_{NIR}^2 + \rho_R + L)}$ L = a correction factor	Modified Non-linear vegetation Index. MNLI is an improved version of NLI. L=0.5 may be applicable for a wide range of LAI.	Developed in this paper.
NDVI*SR	$\frac{(\rho_{NIR}^2 - \rho_R)}{(\rho_{NIR} + \rho_R^2)}$	Attempts to combine merit of NDVI with that of SR.	Developed in this paper.
SAVI*SR	$\frac{(\rho_{NIR}^2 - \rho_R)}{(\rho_{NIR} + \rho_R + L)\rho_R}$	Attempts to combine merit of SAVI with that of SR.	Developed in this paper.
TSAVI	$\frac{a(\rho_{NIR} - a\rho_R - b)}{[a\rho_{NIR} + \rho_R - ab + X(1+a^2)]}$ a = slope of the soil line, b = soil line intercept, X = adjustment factor to minimize soil noise.	Transformed Soil Adjusted Vegetation Index. Modify Huete (1988) SAVI to compensate for soil variability due to changes in solar elevation and canopy structure.	Baret and Guyot, 1991;

Note: ρ_R and ρ_{NIR} denoted as reflectances in red and near-infrared wavelengths, but in this study, they represent band 1 and band 2 across all avaliable 168 bands of Hyperion data.

Table 2. Potential hyperspectral bands for 12 vegetation indices applied to forest LAI estimation.

Index	**R^2** NIR-R/Optim.	**Band** center (nm)	**Bandwidth** (nm)	**Band description** (spectral region and possible absorption features)
SR	0.55/0.70	825	140	NIR region, **cell structure** multi-reflected spectra.
		1038	230	NIR-SWIR region, **water**, **protein**, lignin, starch & oil absorption
		1250	180	SWIR region, **water**, cellulose, starch and lignin absorption
		1648	290	SWIR region, **protein**, **nitrogen**, **lignin**, **cellulose**, sugar, starch absorption.
NDVI	0.55/0.70	…	…	4 bands similar to SR's
PVI	0.45/0.64	814	140	NIR region, **cell structure** multi-reflected spectra.
		1050	100	NIR-SWIR region, **protein**, lignin, and oil absorption
		1250	190	SWIR region, **water**, cellulose, starch and lignin absorption
		2100	10	SWIR region, **starch,** cellulose absorption
SAVI	0.50/0.67	…	…	4 bands similar to NDVI's or SR's

Index	R^2 NIR-R/Optim.	Band center (nm)	Bandwidth (nm)	Band description (spectral region and possible absorption features)
NLI	0.50/0.73	821	157	NIR region, **cell structure** multi-reflected spectra.
		1200	578	NIR-SWIR region, **water**, protein, starch, lignin, cellulose, and oil absorption
		1250	191	SWIR region, **water**, cellulose, starch and lignin absorption
		1640	300	SWIR region, **protein**, **nitrogen**, **lignin**, **cellulose**, sugar, starch absorption.
RDVI	0.45/0.66	810	170	NIR region, **cell structure** multi-reflected spectra.
		1054	10	SWIR region, lignin and oil absorption
		1255	161	SWIR region, **water**, cellulose, starch and lignin absorption
		1669	10	SWIR region, lignin and starch absorption
		2093	10	SWIR region, starch and cellulose absorption
MSR	0.50/0.70	…	…	4 bands similar to NDVI's or SR's
WDVI	0.45/0.63	1639	10	SWIR region, non apparent absorption
		2113	10	SWIR region, **starch** and cellulose absorption
		2285	30	SWIR region, starch, cellulose and protein absorption
MNLI	0.45/0.75	…	…	4 bands similar to NLIs
NDVI*SR	0.50/0.71	…	…	4 bands similar to NDVI's or SR's, but
SAVI*SR	0.50/0.71	…	…	1 - 4 bands similar to SAVI's or SR's
		2083	30	SWIR region, sugar, starch and cellulose absorption
		2153	10	SWIR region, protein absorption
TSAVI	0.50/0.71	832	120	NIR region, **cell structure** multi-reflected spectra.
		1038	150	NIR-SWIR region, **water**, **protein**, lignin, starch & oil absorption
		1240	170	SWIR region, **water**, lignin, cellulose and starch absorption
		1660	260	SWIR region, **lignin**, **cellulose, sugar**, starch, protein, and nitrogen absorption
		2108	20	SWIR region, **starch**, cellulose and protein absorption
Note: Optim. = optimal correlation R^2; **bold chemicals** are principal for the absorption features				

Conclusions

The experimental results indicate that the 4-point approach is a more practical method for extracting the two red edge parameters because only 4 bands are needed. The polynomial fitting approach also has the advantage that it is a direct method for deriving these parameters. It also has practical value if hyperspectral data (spectral resolution narrower than 10 nm like Hyperion data) are available. Moreover, this approach can model the phenomenon of two maximum first-derivatives along the red edge curve. Since the first derivative spectra frequently are not directly available for most multi/hyperspectral sensors, use of the Lagrangian technique is less practical. The IG modeling, used for extracting red edge optical parameters from space-borne hyperspectral data, needs further testing if a linear fitting approach as tested in this study is applied.

Evaluation and Validation of EO-1 for Sustainable Development (EVEOSD) of Forests

David G. Goodenough, A. Hollinger, R. Hall, D. Leckie, A. Dyk, J. Miller, J. Iisaka, Olaf Niemann, Karl Staenz, Harold Zwick, Jay Pearlman

In this investigation, EO-1 data were acquired to evaluate the ability of the EO-1 spaceborne sensors to measure forest attributes. Experiments were conducted with EO-1 data to validate that products obtained from the Advanced Land Imager (ALI) and Hyperion were as good as or better than products produced earlier with Landsat sensors with an eye toward ensuring Landsat continuity. The EVEOSD team, with members from the Canadian and U.S. government, academia, and industry, also validated Hyperion imagery by comparing it with Airborne Visible/Infrared Imaging Spectrometer (AVIRIS) hyperspectral data and detailed field data. Further, since it was determined that precise geometric correction of remotely sensed data was critical to link ground spectral data with satellite data, the investigators also examined the process of calibrating and correcting Hyperion and ALI data.

EO-1 data were collected over seven of eight test sites in Canada and one in Washington State for the Evaluation and Validation of EO-1 for Sustainable Development (EVEOSD) project. Two of the sites, the Greater Victoria Watershed District (GVWD) located on south Vancouver Island, British Columbia, and Hoquiam in southwestern Washington State, were used to examine the atmospheric correction process and the creation of bioindicators and determination of forest chemistry. The EO-1 satellite successfully acquired imagery over Hoquiam on August 9, 2001, and over GVWD on September 10, 2001. Figure 1 shows the EVEOSD sample plots in GVWD.

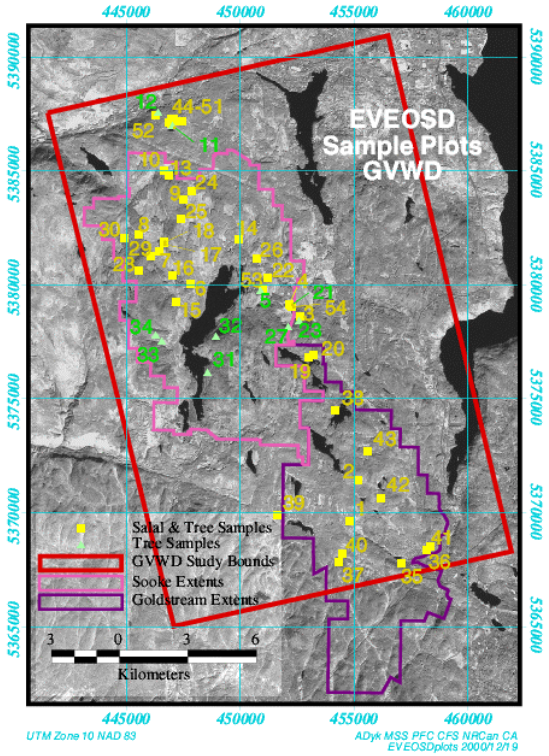

Figure 1. Sampling locations in GVWD.

Ground samples of treetop foliage and salal (a shrub) were also collected, and organic and inorganic data analyses were performed on these samples in September 2000 and July 2001. The organic chemical analyses on the treetop samples were separated into current (during the last year) and non-current growth. Analyses contained data on chlorophyll, the percentages of moisture and nitrogen, and the concentration of several chemical elements in each sample. Four plots identified Douglas fir foliage that had elevated arsenic levels. The arsenic level in the elevated Douglas Fir plots reached as high as 348 parts per million (ppm), while normal plots averaged only 29 ppm. Neither salal nor soil samples nearby showed such elevated levels.

The correction process consisted of GCP (ground control point) collection, Hyperion and ALI registration (separately for data from each instrument), and orthorectification. Hyperion data required that "smile errors" be fixed. Hyperion images also commonly contained stripes that needed to be removed, as more than 15% of Hyperion bands exhibited some stripes. Destriping could be accomplished in two ways. One used an algorithm to replace the striping pixels by taking the average of their immediate left and right neighbors. The second used an algorithm (based on work by Alexander F.H. Goetz) to perform minimum noise fraction (MNF) rotation on the original Hyperion image, force the column mean to zero of each MNF band, and apply the inverse MNF to the mean removed data.

GCP collection used a feature-fitting method in which ground features were adjusted to match the same features as they appeared in a hyperspectral image such as acquired from AVIRIS or Hyperion. Images were calibrated to reflectance. Final adjustment factors were determined to force the image reflectance to agree with the ground reflectance for a calibration target. Figure 2 shows pre- and post-force-fit AVIRIS images. For Hyperion, GCPs were collected independently from both the visible and near infrared (VNIR) and shortwave infrared (SWIR) arrays to determine the adjustment factor required to remove the displacement and skew between these arrays. When the adjustment factor had been determined, it could then be applied to GCPs that had been collected from both the VNIR and SWIR arrays and the effects of geometric correction of the spectra analyzed.

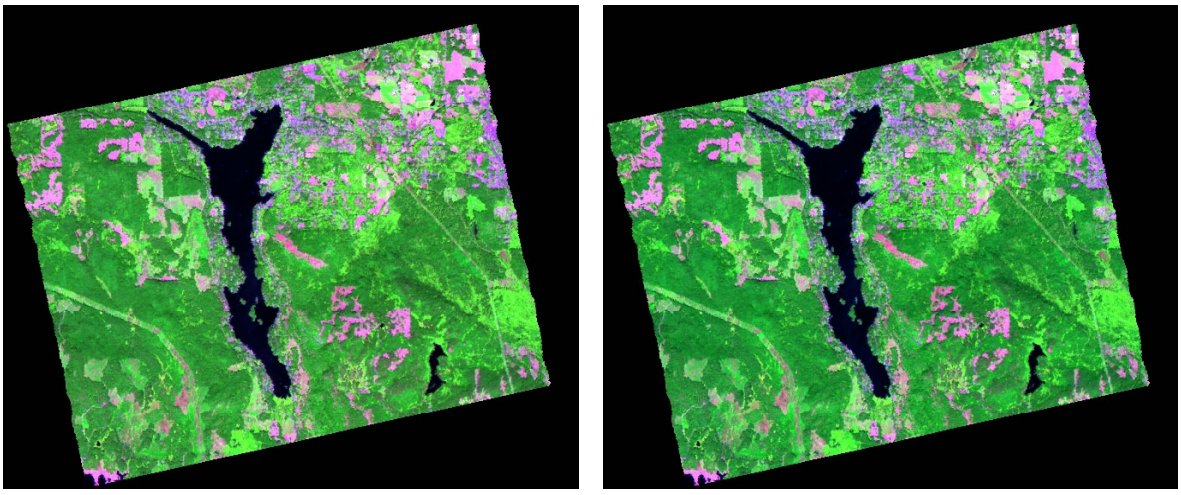

Pre force-fit **Post force-fit**

Figure 2. Force-fit AVIRIS images.

Geocorrection had good results. It was found that both Hyperion and ALI data could be geocorrected with considerable accuracy. Using the Rational Function Model (RFM) and a digital terrain model, excellent geocoding accuracies were obtained in orthorectifying the data to merge with GIS (Geographic Information System) data, with rms (root mean square) errors of collected GCPs at or under the 10-meter accuracy of the source vectors. Hyperion was geocoded to an rms of 10.01 meters and ALI to an rms of 5.18 meters.

Two EO-1 products were produced from this investigation: classification products and bioindicator products. For forest classification, Hyperion produced an aggregated classification accuracy of 94.2%. This compared with an accuracy of 77.5% for Landsat's Enhanced Thematic Mapper Plus (ETM+), 94.0% for AVIRIS, and 87.5% for ALI using 70% of the training data and accuracies of 90.0%, 75.0%, 92.1%, and 84.8% for Hyperion, ETM+, AVIRIS, and ALI respectively with 30% of the test data (Figure 3).

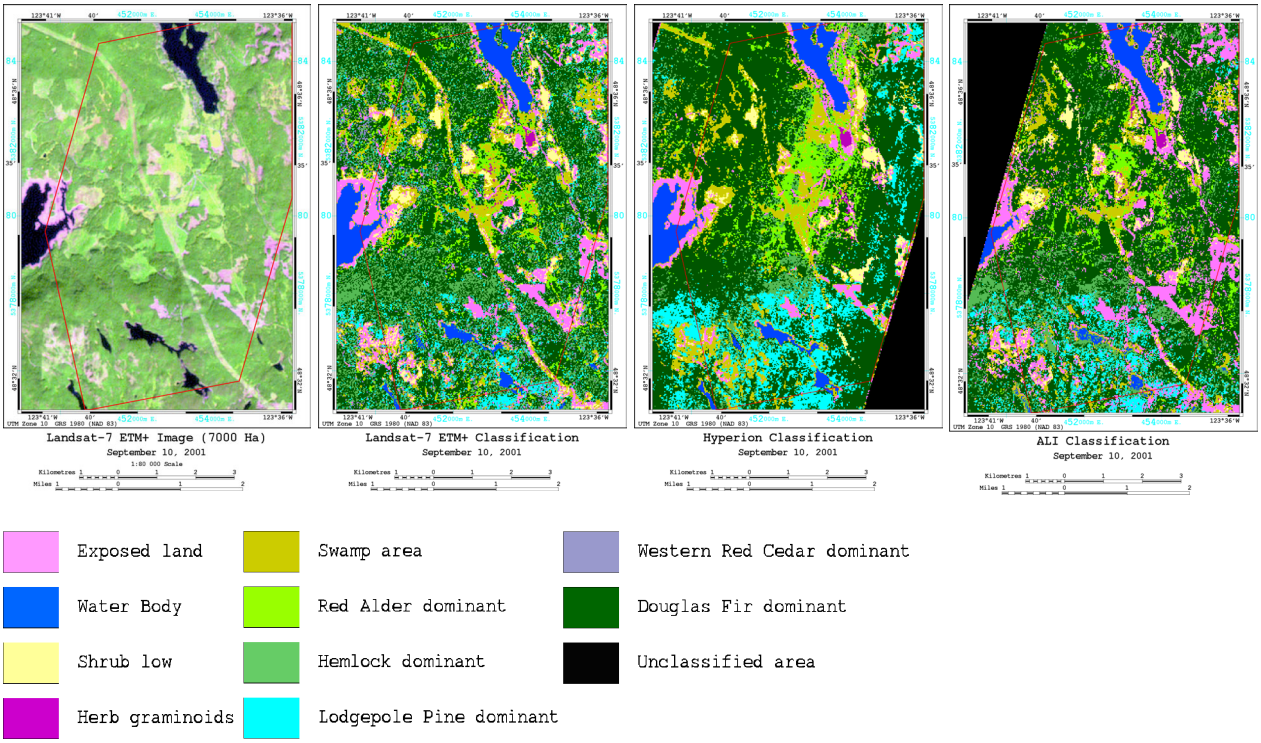

Figure 3. Classification results.

Bioindicators, indicators of forest health, involve assessing ecological processes in forested environments. They provide insight into the health of forest ecosystems by revealing current ecological conditions and have the potential to assess and improve large-scale management of forest environments. Bioindicators are being developed to characterize chlorophyll and nitrogen distribution in forests and to identify moisture and environmental stresses. The concentration of chlorophyll a in the GVWD was measured using Hyperion bands at 750 nm and 700 nm (Figure 4). Figure 5 shows the corresponding chlorophyll a and bioindicator values for mature Douglas Fir plot locations.

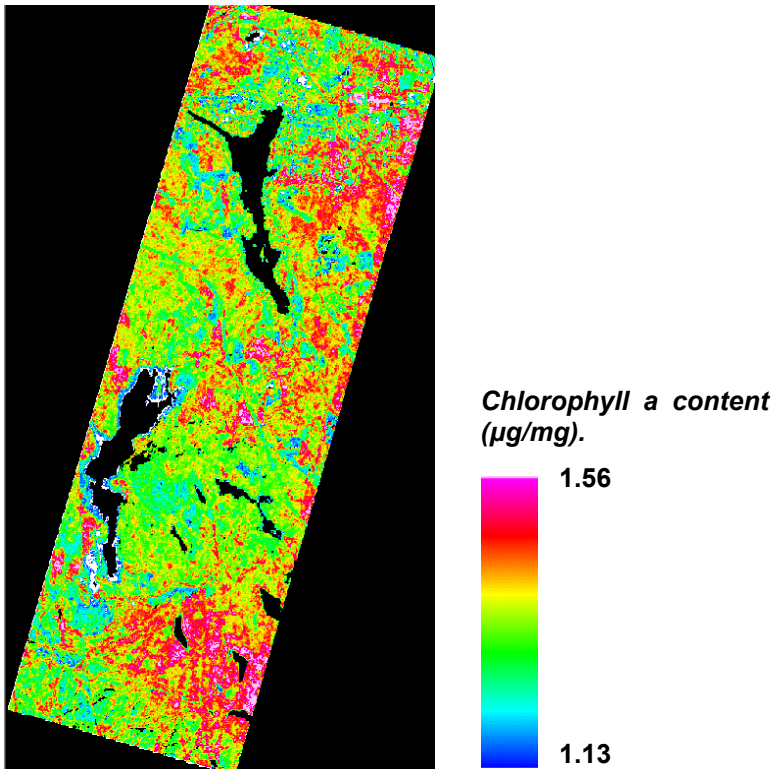

Figure 4. Chlorophyll a concentrations acquired by Hyperion, September 10, 2001.

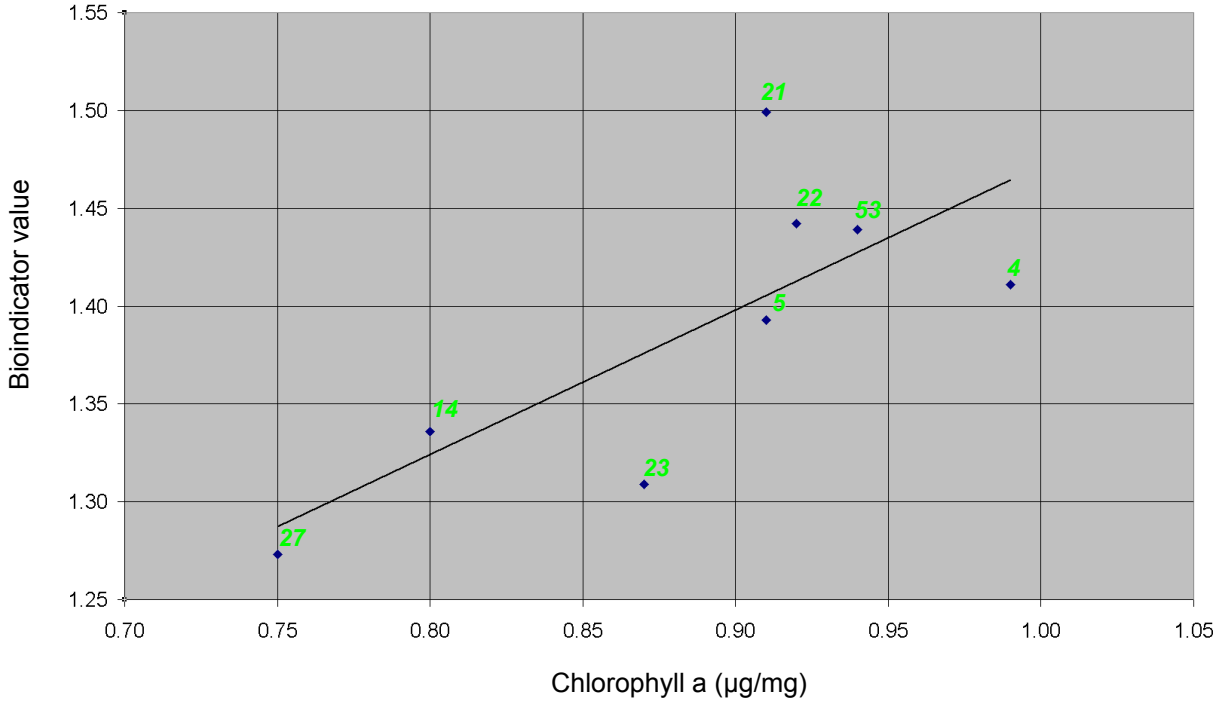

Figure 5. Chlorophyll a and bioindicator values in mature Douglas Fir plots.

Conclusions:
Hyperion data can be corrected automatically for stripes and smile, but atmospheric correction needs further research. Radiometric errors remain. Image resampling needs to be improved for 12-bit inputs; 12-bit data challenge the current capabilities and accuracies of commercial image analysis software. Excellent geocoding accuracies of 10.1 meters for Hyperion and 5.18 meters for ALI were obtained. Hyperion produced operational forest classification accuracies of 90.0% and AVIRIS of 92.1% for several tree species in GVWD. ALI forest classifications were much better than that for ETM+, with ALI producing accuracies of 84.8% compared with 75.0% for ETM+. Calibration databases of foliar and ground organic and inorganic chemical measurements, forest mensuration parameters, and spectral reflectances were constructed.

The investigators also identified future steps to be taken. The need exists to better understand the chemistry of forests based on ground measurements, three-dimensional monitoring, and modeling. The investigators found that the best correlations were obtained with stratification into species of similar forest maturities. They anticipate that chemistry products from hyperspectral remote sensing will revolutionize GIS and forest information systems. Hyperspectral remote sensing also has the potential to provide early detection of insect damage in forests, and accurate hyperspectral nitrogen maps will make forest company fertilization programs much more effective.

Using ALI Observations to Estimate Land Surface Biophysical Variables
Shunlin Liang

This study examined whether observations from the EO-1 Advanced Land Imager (ALI) can be used to estimate land surface biophysical variables accurately. The investigators developed and tested a series of new algorithms and validated the derived products using correlative ground measurements through field campaigns. Validation through field campaigns was carried out at the U.S. Department of Agriculture Beltsville Agricultural Research Center in Beltsville, Maryland, and at the Coleambally Irrigation Area in Australia.

The investigation focused primarily on two biophysical variables: broadband albedos and leaf area index (LAI). Albedo is important when determining the Earth's climate and for computing the surface energy balance. Land surface albedo can be acquired only through remote sensing. LAI is also an important factor in land surface models.

Two important pre-processing steps must occur before albedo and LAI can be quantitatively estimated. First, sensor radiometric calibration that converts the digital numbers to top-of-atmosphere (TOA) radiance must take place. Second, TOA radiance must be converted to surface reflectance. This is done through atmospheric correction. An atmospheric correction algorithm designed for use with the Landsat Enhanced Thematic Mapper (ETM+) imagery was enhanced for this purpose. The method used to develop this enhanced algorithm built on a series of steps. First, atmospheric correction that converts TOA radiance to surface directional reflectance was carried out. ALI's one extra blue band proved very useful in this atmospheric correction algorithm. Then, BRDF (Bidirectional Reflectance Distribution Function) modeling that converts directional reflectance to narrowband albedos, and also narrowband to broadband conversions were done. A set of formulae were developed for converting ALI narrowband albedos to three broadband albedos. Figure 1 shows broadband albedo maps over Beijing City, China.

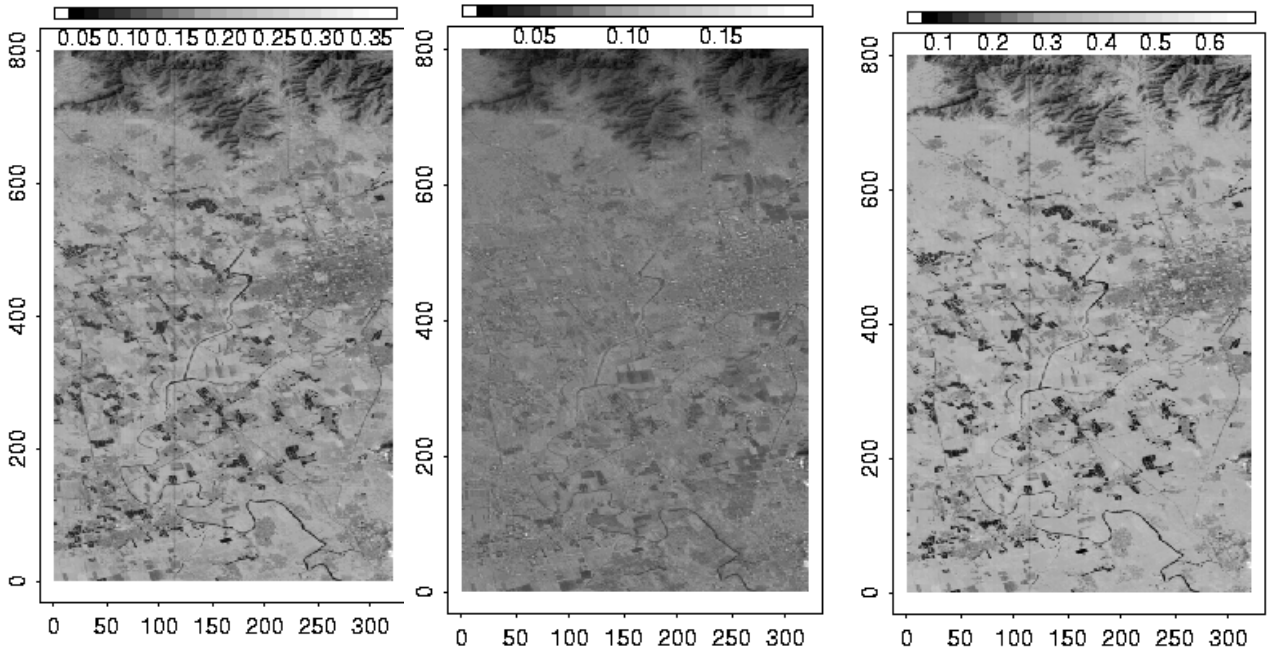

Figure 1. ALI broadband albedo maps over Beijing, China.

To estimate canopy LAI, two types of algorithms can be used: (1) statistical, which relies primarily on vegetation indices that are linked with measured LAI data; and (2) physical models. The second type, physical models, is based on inverting canopy reflectance models and is very time-consuming and difficult at the regional level. In this study, investigators developed a "hybrid," or "inversion," algorithm that combined both statistical and physical algorithms. The statistical part of this model used a nonparametric regression algorithm to link LAI and band reflectance. The physical component used the canopy radiative transfer model for extensive simulations. Figure 2 shows LAI maps made using the hybrid inversion algorithm at three different times of crop growth. The maps show logical LAI for the crops and months being mapped. Validation resulted in an error of less than 0.5.

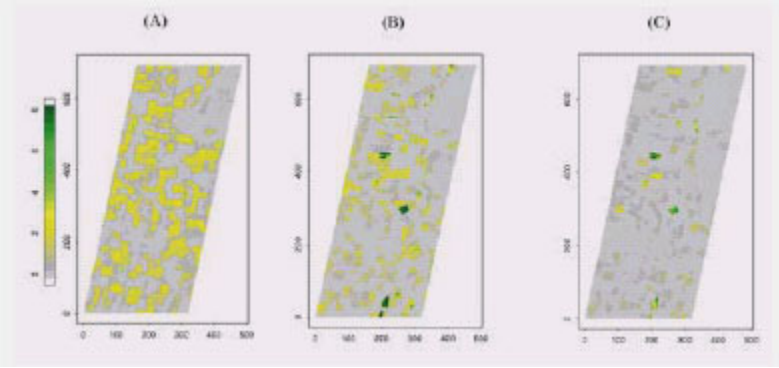

Figure 2. Retrieved LAI maps over Coleambally Irrigation Area from ALI imagery in January (left), February (center), and March (right).

Results and Conclusions:

Comparisons of ALI corrected imagery that used the newly developed algorithm with simultaneous measurements of surface reflectance indicated that the algorithm was highly accurate. Use of the algorithm enabled accurate retrieval of surface reflectance with residual errors of about 0.01 in the shortwave bands and about 0.03 in the near-IR bands. Figure 3 shows a composite image before and after atmospheric correction. Results also demonstrated that the algorithm could remove heterogeneous aerosol scattering effects effectively. It was also seen that the additional spectral bands present on ALI but not on the ETM+ were helpful for atmospheric correction and retrieval of land surface variables. In particular, the additional blue band helped identify hazy regions in the algorithm. Further, the two near-IR bands (4' and 5') were valuable in converting narrowband to broadband albedos and determining LAI. The advantages these additional bands provide may be algorithm-dependent, but the algorithms developed in this investigation were able to take full advantage of the additional bands.

Figure 3. False-color composite imagery near Beijing City, China, before (left) and after atmospheric correction.

Data Continuity of Earth Observation (EO-1) Advanced Land Imager (ALI) and Landsat TM and ETM+

R. Bryant, **M.S. Moran**, S. McElroy, C. Holifield, K. Thome, T. Miura, and S.F. Biggar

In the year 2000, NASA launched the Earth Observing-1 (EO-1) Advanced Land Imager (ALI) to test new technologies that could improve the Landsat Thematic Mapper/Enhanced Thematic Mapper Plus (TM/ETM+) sensor series, yet ensure Landsat data continuity. The ALI sensor is characterized by a better signal to noise ratio (SNR) than the Landsat ETM+ and also has three additional bands (Table 1).

Table 1. Spectral and spatial definitions for the 10 EO-1 ALI bands. Bands 1p, 4p, and 5p are bands that are not found on the ETM+. Other bands correspond to ETM+ bands.

Band	Wavelength (μm)	Ground Sampling Distance (m)
Pan	0.48 – 0.69	10
MS-1p	0.433 – 0.453	30
MS-1	0.45 – 0.515	30
MS-2	0.525 – 0.605	30
MS-3	0.633 – 0.69	30
MS-4	0.775 – 0.805	30
MS-4p	0.845 – 0.89	30
MS-5p	1.2 – 1.3	30
MS-5	1.55 – 1.75	30
MS-7	2.08 – 2.35	30

This study quantified the continuity of satellite-retrieved surface reflectance (Δ) for the three most recent Landsat sensors (Landsat 4 TM, Landsat 5 TM, and Landsat 7 ETM+) and the EO-1 ALI sensor. The study was based on ground data verification and, in the case of the ETM+ to ALI comparison, coincident image analysis. Image data was obtained from two locations where extensive ground data was available: the Maricopa Agriculture Center (MAC) southwest of Phoenix, Arizona; and the Walnut Gulch Experimental Watershed in southeastern Arizona, an area that has been studied for nearly 50 years (Figure 1). All comparisons relied on ground measurements of surface reflectance for an independent measure of sensor response.

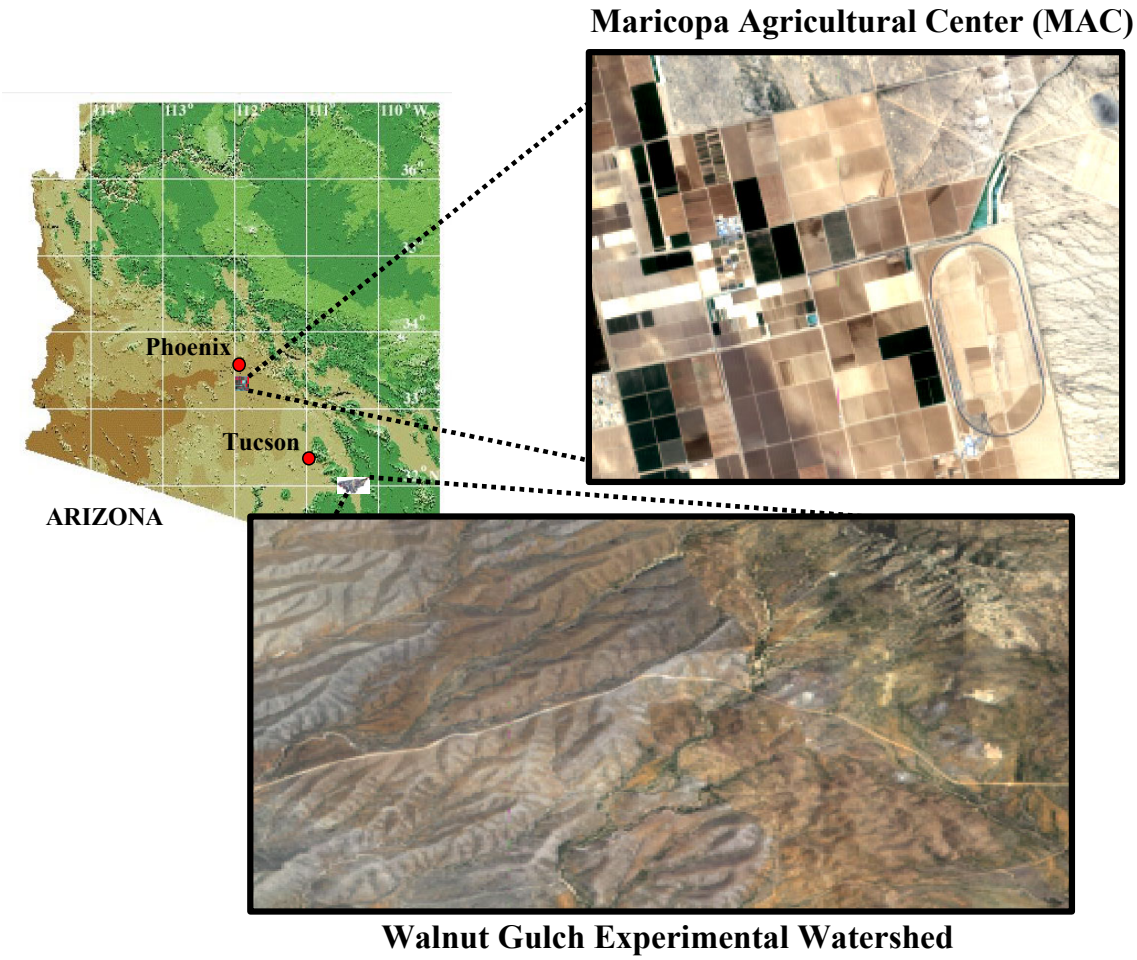

Figure 1. Study Sites

Three separate analyses of data continuity were conducted: (1) Landsat 4 to Landsat 5 TM, (2) Landsat 5 TM to Landsat 7 ETM+, and (3) Landsat 7 ETM+ to EO-1 ALI. For the Landsat 4 – Landsat 5 comparison, data from four Landsat 4 TM images and five Landsat 5 TM images were used. For the Landsat 5 and Landsat 7 comparison, a total of 25 targets were analyzed. In the case of the Landsat ETM+ - ALI comparison, direct sensor-to-sensor comparison was possible because the images from the two sensors were acquired almost simultaneously. For this analysis, 21 data points from five different days at two sites were used. Except for the Landsat 4 – Landsat 5 comparison, atmospherically corrected satellite-based reflectances were compared to ground reflectance.

In all cases, the root mean squared error (RMSE) between satellite-retrieved and ground-measured reflectance were comparable between sensors, and RMSE was generally within the required accuracy for many applications (Tables 2-4). The direct comparison between image pairs of Landsat 7 ETM+ and EO-1 ALI (Table 5) showed good comparability for bands 1-4 and band 7, (RMSE <= 0.02) and moderate results for band 5 (RMSE = 0.03). When the RMSE of all sensors were compared (to minimize the effects of different methodologies), the sensors showed excellent data continuity. The absolute differences in RMSE ranged from 0.00 to 0.02 (Table 6).

Table 2. Root mean square error (RMSE) for ground measured reflectance and reflectance derived using the Refined Empirical Line method for Landsat 4 TM and Landsat 5 TM sensors.

Sensor	Band 1	Band 2	Band 3	Band 4
Landsat 4 TM	0.008	0.006	0.009	0.011
Landsat 5 TM	0.015	0.006	0.009	0.023

Table 3. Root mean squared error (RMSE) between ground-measured reflectance and satellite-retrieved reflectances from Landsat 5 TM and Landsat 7 ETM+ sensors.

Sensor	Band 1	Band 2	Band 3	Band 4
Landsat 5 TM	0.017	0.016	0.022	0.027
Landsat 7 ETM+	0.022	0.018	0.022	0.038

Table 4. Root mean squared error (RMSE) between ground-measured reflectance and satellite-retrieved reflectances from Landsat 7 ETM+ and EO-1 ALI.

Sensor	Band 1	Band 2	Band 3	Band 4	Band 5	Band 7
Landsat 7 ETM+	0.023	0.024	0.027	0.057	0.032	0.013
EO-1 ALI	0.021	0.020	0.023	0.037	0.020	0.020

Table 5. Root mean squared error $RMSE_s$ between satellite-retrieved reflectance for Landsat 7 ETM+ and satellite-retrieved reflectance for EO-1 ALI.

Band 1	Band 2	Band 3	Band 4	Band 5	Band 7
0.003	0.012	0.009	0.018	0.031	0.020

Table 6. Absolute difference in RMSE of ground-measured reflectance and satellite-retrieved reflectance between sensor pairs.

Sensor Pair	Band 1	Band 2	Band 3	Band 4	Band 5	Band 7
Landsat 4 TM Landsat 5 TM	0.007	0.000	0.000	0.012		
Landsat 5 TM Landsat 7 ETM+	0.005	0.002	0.000	0.011		
Landsat 7 ETM+ EO-1 ALI	0.002	0.004	0.004	0.020	0.012	0.007

A qualitative analysis of the new ALI spectral band 5p (1.20-1.30 μm) showed that ALI band 5p provided information that differed from that provided by the ETM+/ALI SWIR bands 5 and 7 for agricultural targets (Figure 2). Further investigation is warranted to determine what distinctive surface characteristics influenced the reflectance in band 5p.

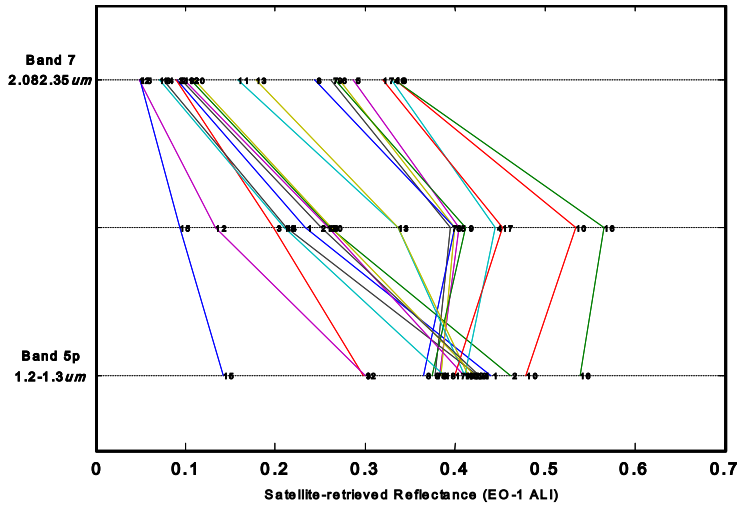

Figure 2. Reflectances retrieved from EO-1 ALI shortwave infrared (SWIR) spectral bands for all 21 targets. Numbers on the graph correspond to target numbers.

ALI band 4p has the advantage over both the ETM+ band 4 and ALI band 4 in that it is relatively insensitive to water vapor absorption (Table 7). Furthermore, since the reflectances retrieved from ETM+ band 4, ALI band 4, and ALI band 4p for 21 agricultural targets were nearly identical, it could be an excellent substitute band for ETM+ band 4 on the next Landsat mission.

Table 7. Root mean squared error (RMSE) reflectance retrieved from Landsat 7 ETM+ band, EO-1 ALI bands 4 and 4p, and associated ground-measured reflectance. Two cases are presented: atmospheric correction without water vapor correction and with water vapor correction.

Band	Without water vapor correction	With water vapor correction
ETM+ Band 4	0.078	0.057
ALI Band 4	0.052	0.041
ALI Band 4p	0.037	0.034

Conclusion:

The four sensors can provide excellent data continuity for temporal studies of natural resources. Furthermore, the new technologies put forward by the EO-1 ALI sensor have had no apparent negative effect on data continuity and should be considered for the next Landsat sensor payload.

Comparison of the Precision and Accuracy of ALI and ETM+ Data for Semiarid Vegetation Studies

Andrew Elmore and **John Mustard**

Land monitoring in semi arid and arid regions is often difficult because of inhospitable, remote terrain and wide expanses of land. For at least the past 20 years, remote sensing, particularly from Landsat satellites, has aided in vegetation monitoring. In the past, investigators have used data from Landsat along with Spectral Mixture Analysis (SMA) to estimate the percent of vegetation green cover (GC). Estimates of uncertainty in the remotely derived estimates of percent green cover were arrived at through comparisons of remote and field-based observations and serve as a basis for comparison of future remote sensing techniques.

This study investigated the capability of the EO-1 Advanced Land Imager (ALI) for measurement of the %GC. In particular, the study investigated three areas: (a) the ability of ALI to determine %GC using the spectral bands functionally equivalent to those found on Landsat's Enhanced Thematic Mapper Plus (ETM+), (2) how well ALI calculated %GC using all nine spectral bands, and (3) how well ALI produced internally consistent images of vegetation cover for quantitative ecological analyses.

Owens Valley, a semi-arid basin in eastern California characterized by drought-tolerant shrubs and grasses (Figure 1), was chosen for this study. ALI and ETM+ each acquired one dataset on June 21, 2001. Concurrently, field data on %GC floristic composition was collected at 27 field sites.

Figure 1. Study area, Owens Valley, California.

By averaging the near infrared (NIR) bands centered at 0.790 µm and 0.868 µm and removing the bands centered at 0.443 µm and 1.25 µm, a six-band ALI data set was created. The ETM+ and ALI data sets were then co-registered to a previously georeferenced data set and the six-band ALI data set was spectrally aligned to the ETM+ data set. Endmember sets were selected for the ETM+ and the ALI data that included spectra from a variety of land cover. An additional

endmember was selected utilizing ALI's complete range of nine bands. SMA was applied to the one ETM+ dataset and the two ALI datasets (six-band and nine-band). The resulting vegetation fraction images were used as the remotely sensed estimate of %GC as compared to field data. Field sites were located in each data set and compared with the remotely acquired data to determine the accuracy of the vegetation measurement (Figure 2). The Global Positioning System and aerial photography were used to help accurately locate the field sites.

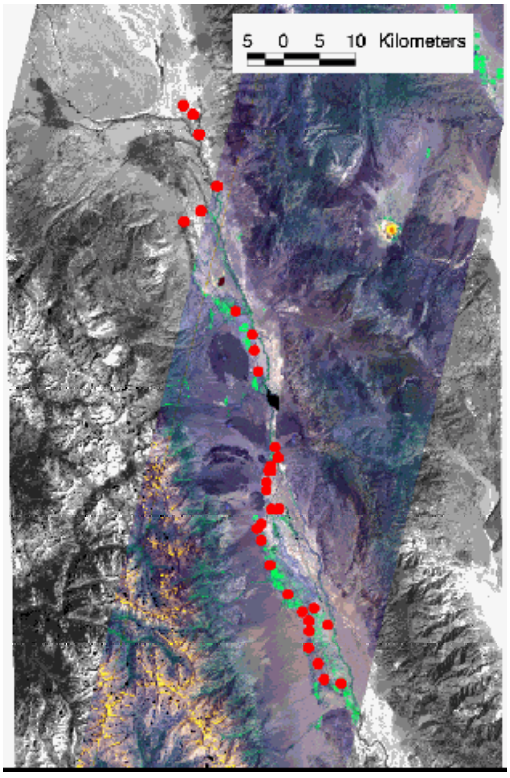

Figure 2. ALI image. Field sites are designated with red circles.

The ability of ALI and ETM+ to estimate vegetation cover relative to field results was compared using criteria that calculated the standard deviation from a perfect fit, a 1:1 line. The deviation from the 1:1 line represents the uncertainty in using remotely sensed measurements as a replacement for field-based vegetation measurements. ALI and ETM+ produced similarly accurate %GC estimates: +/- 6.16 %GC for ALI and +/- 5.61 %GC for ETM+ deviation from a perfect fit with the 1:1 line. Although these uncertainty values indicated little advantage to using ALI over ETM+ for these measurements, other differences between the sensors favored ALI. For example, ALI did not result in as many negative %GC values as did ETM+. And, when profiles across landscapes with low vegetation cover were compared, ALI exhibited lower pixel-to-pixel noise. Using only six ALI bands appeared to produce the same degree of accuracy as using all nine of its bands. This fact can lead investigators to conclude that increased data precision, rather than the number of bands, makes ALI a better, more accurate sensor for estimating vegetation coverage in this type of environment. An alternate conclusion is additional bands should be in spectral regions that can provide new information and not in regions that are highly correlated with existing bands.

Investigators also examined whether ALI was internally consistent. A transect across a center-point agricultural field was extracted for a region where SCA3 (Sensor Chip Assembly) and SCA4 overlapped. Results showed that multispectral band registration was inconsistent between the ALI SCA arrays. However, despite the Band 3 residual anomaly, the percent live cover was very similar for each of the SCA data sets, producing inconsistent measures only where gradients in vegetation cover were very high.

Conclusions:
The investigators found no large and consistent differences between ALI and ETM+ results. The variation in band-registration between ALI SCAs was the only significant negative outcome. Investigators emphasized the importance of being able to obtain consistent measurements of specific geographic regions, particularly in regions of high vegetation variability and when studying annual vegetation changes.

Canopy Modeling and Satellite Comparison Studies Using EO-1

James A. Smith

Background

This report gives a brief synopsis of our research studies in the comparison and use of EO-1 satellite observations with field measurements, modeling, and other satellite systems. The work is on-going. We have three study areas representing different physiographic and land cover regions where we make detailed measurements of the surface and atmospheric state, co-incident with satellite tasking. Our sites include areas near Rochester, NY, Howland, ME, and Fraser, CO. This summary principally discusses analyses from the Rochester site. Additional material is given in the references.

The Rochester site is near the shore of Lake Ontario and contains a variety of features, ranging from water of varying depths, deciduous/coniferous forest, grass fields, and urban areas. It was chosen because of its proximity to the Rochester Institute of Technology (RIT), which assisted in ground data collection. Additionally, we originally intended to compare observations with the RIT airborne multispectral scanner, especially its thermal infrared bands, with the Landsat thermal infrared band. However, our key aircraft data acquisition effort coincided with September 11, 2001, and we were not able to complete this line of attack.

But we were successful in acquiring co-incident, high resolution multispectral and thermal infrared observations from the Department of Energy Multispectral Thermal Imager (MTI) satellite. In collaboration with the Los Alamos National Laboratory, we also have obtained co-incident tasking of the MTI and EO-1 over all three of our study sites, and fieldwork and analyses continue.

The Howland, ME study site is contained within the International Paper's Northern Experimental Forest (NEF). It is a boreal--northern hardwood transitional forest consisting of hemlock-spruce-fir, aspen-birch, and hemlock-hardwood mixtures and is a MODIS validation site.

The Fraser, CO study site is contained within the U.S. Forest Service Fraser Experimental Forest. It is a high elevation site ranging from 2680 to 3900 m. Engelmann spruce and subalpine fir are the predominant trees at higher elevations or north slopes; lodgepole pine is the predominant tree at lower elevations and on drier upper slopes. The study site is part of the NASA Cold Land Processes Experiment (CLPX).

Objectives

Our initial objective was to compare the performance of the EO-1 Advanced Line Imager (ALI) with the Landsat 7 Enhanced Thematic Mapper (ETM+). Secondly, we wanted to apply calibration and atmospheric corrections to the data to compare with surface measured reflectance and predicted canopy reflectance and thermal infrared model simulations.

A long-term objective is to see if we can separate the observations of the thermal infrared versus reflectance measurements in time and from different platforms. Originally, we intended to use the ETM+ thermal infrared band. However, the DOE MTI sensor provides a better capability to test our hypotheses. Further, we found that the EO-1 Hyperion sensor provides a rich source of spectral features for comparison to our models and can be used for atmospheric corrections using its appropriate spectral bands. Our current efforts emphasize Hyperion and MTI.

Comparison of Landsat-7 ETM+ and EO-1 ALI

The ALI differs from the ETM+ in a number of ways. The pushbroom design of the ALI provides a much longer dwell time per pixel (~4 msec) than the whiskbroom ETM+ (~10 µsec), which permits 12-bit digitization of the ALI data with a single gain setting. The 10m resolution of the panchromatic band improves on the 15m resolution of the ETM+, and the ALI panchromatic band was narrowed to 0.48µm - 0.70µm from the 0.52µm - 0.90µm bandwidth on the ETM+. The ALI also has two new multispectral bands: band 1' (0.43µm - 0.45µm) and 5' (1.20µm – 1.29µm). Additionally, the ETM+ band 4 was split into bands 4 and 4' to avoid a water absorption feature. Finally, the ALI has no thermal band.

For the comparisons discussed here, we obtained ETM+ and ALI images on August 25, 2001 over the Rochester, NY area. A recent Ikonos image highlighting the area is shown below in Figure 1.

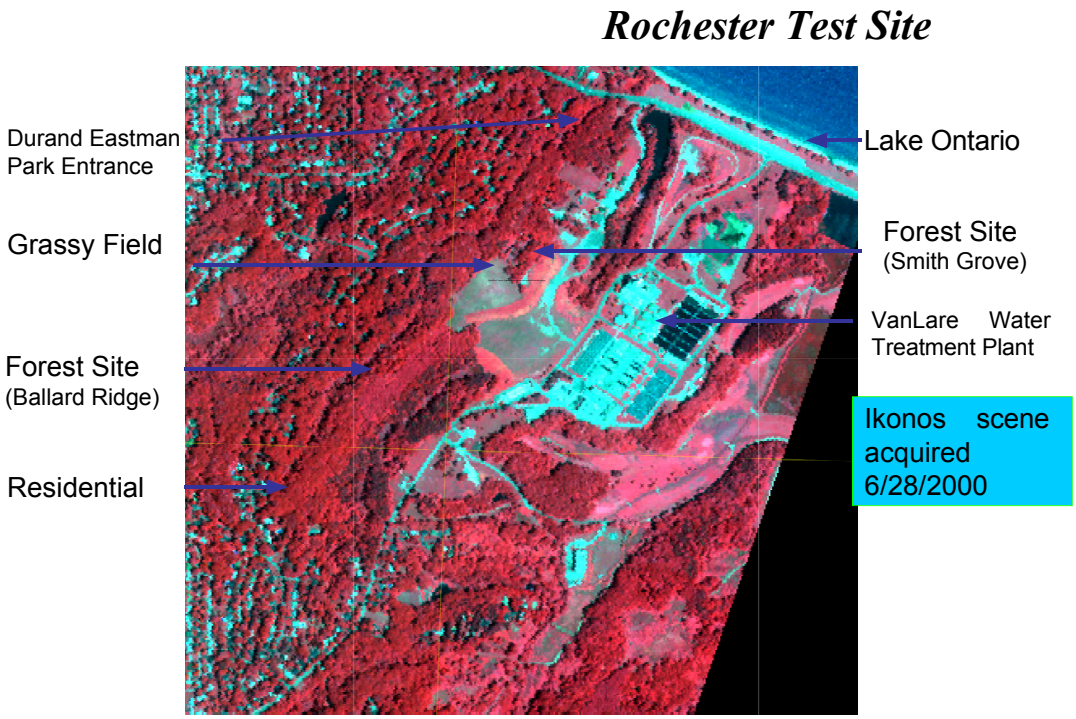

Figure 1. Ikonos Image of Rochester, NY Area

The ETM+ image was on the WRS2 path 16, row 30 scene at 15:40:12 GMT, while the ALI was approximately one minute behind at 15:41:08 GMT. We received the ETM+ L0R data product from the USGS EROS Data Center (EDC) via the EOS Data Gateway. The L0R scene is essentially a raw, but band separated, data product. We applied standard radiometric and geometric corrections to create L1R datasets using our local copy of the EDC Image Assessment System. Full details of the data formats and radiometric and geometric processing are provided in the Landsat 7 Science Data Users Handbook. We received the ALI Level 1 data product from the EO-1 Science Validation Facility at NASA's GSFC. The ALI Level 1 product has been radiometrically, but not geometrically corrected. Our study area was fully imaged by subchip assembly #4, and thus was affected by 3 inoperable detectors in band 5. We interpolated across these inoperable detectors.

We converted the ETM+ and ALI data numbers (DN) to atmospherically corrected reflectance (ACR) by a multi-step process. We first converted each data product from scaled radiance to at sensor radiance (units $W/m^2/sr/\mu m$) by using calibration factors and dividing the ALI image values by 30 and the ETM+ values by 100. We monitored the atmospheric properties using a Cimel sun photometer that was part of the Aerosol Robotic Network (AERONET). It measured the aerosol optical thickness (AOT) at 670nm and 500nm and water vapor column density approximately every 15 minutes. We interpolated these AOT measurements to 550nm and to the image acquisition times to give an AOT of 0.09. We similarly obtain a water content of 1.85 g/cm^2. For ozone content, we used National Center for Environmental Prediction (NCEP) data, which provides ozone data every 6 hours. We interpolated the nearest two measurements to obtain an ozone content of 0.30 cm-atm.

We ran the 6S atmospheric correction code for each of the 15 ALI and ETM+ bands using these measures of the atmospheric conditions and assuming a continental aerosols model. In this mode 6S generates the coefficients xa, xb, and xc that convert the measured at sensor radiance in each band to atmospherically corrected surface reflectance (ACR) via the following equations:

$$y = xa * radiance - xb$$

$$ACR = y / (1 + xc * y)$$

In Tables 1 & 2 below, we show the center wavelength, bandwidth, and the 6S-derived xa, xb, and xc correction coefficients for each of the ETM+ and ALI bands.

Table 1. Bandpass and Atmospheric Correction Parameters for the VNIR Bands

	ALI 1'	ALI 1	ETM+ 1	ALI 2	ETM+ 2	ALI 3	ETM+3	ETM+ 4	ALI 4	ALI 4'
Center λ	0.442	0.485	0.483	0.567	0.56	0.660	0.662	0.835	0.790	0.866
Bandpass	.43-.45	.45-.51	.45-.51	.53-.60	.52-.60	.63-.69	.63-.69	.77-.90	.78-.80	.84-.89
xa	0.0032	0.0028	0.0028	0.0029	0.0029	0.0032	0.0032	0.0045	0.0039	0.0045
xb	0.1404	0.0932	0.0989	0.0507	0.0528	0.0271	0.0270	0.0119	0.0135	0.0097
xc	0.1868	0.1466	0.1520	0.0950	0.0980	0.0630	0.0627	0.0349	0.0394	0.0314

Table 2. Bandpass and Atmospheric Correction Parameters for the SWIR and Panchromatic Bands

	ALI 5'	ETM+ 5	ALI 5	ETM+ 7	ALI 7	ETM+ pan	ALI pan
Center λ	1.244	1.648	1.640	2.206	2.226	0.705	0.592
Bandpass	1.20-1.29	1.55-175	1.55-1.73	2.07-2.35	2.09-2.36	0.52-0.90	0.50-0.68
Xa	0.0101	0.0199	0.0194	0.0598	0.0612	0.0036	0.0030
Xb	0.0037	0.0017	0.0017	0.0007	0.0007	0.0280	0.0461
Xc	0.0148	0.0080	0.0081	0.0037	0.0037	0.0618	0.0895

Visual Image Comparisons

We extracted a 320 x 320 pixel subimage that includes the Durand Eastman Park, Lake Ontario, Irondequoit Bay, and NE Rochester. In Figure 2 below, we show true color composites of the atmospherically corrected reflectance images using bands 3, 2, and 1 of the ETM+ (left) and ALI (right). We use identical linear color transfer functions that exclude the highest and lowest 2% of the pixel histograms. We present Level 1R data from both instruments to maximize radiometric fidelity, which means that slight geometric displacements are visible in the ETM+ image, and that north is not precisely up.

Qualitatively the ETM+ and ALI images are nearly indistinguishable. We can see more detail in Lake Ontario because of the 12-bit quantization of the ALI data. Interestingly, we can use the ~one minute separation between the images to conclude that the ship near the pier in the ETM+ image is entering Lake Ontario at roughly 24 knots.

Figure 2. True Color Composites (Bands 3, 2. & 1) – ETM+ (Left) and ALI (Right)

We illustrate the differences in the ALI and ETM+ panchromatic bands in Figure 3 below which shows Irondequoit Bay and the pier into Lake Ontario. The ALI data provide better definition of the marina and pier, and much more detail in the water features of both Lake Ontario and Irondequoit Bay. Three effects

are responsible for the improvement in the ALI panchromatic image: the increase in resolution from 15m to 10m, the increase to 12-bit quantization, and the narrowing of the bandpass. The 12-bit quantization is most responsible for the improved water detail. With a bandpass that cuts off at 0.7μm the ALI image excludes the sharp vegetation rise, which leads to a darkening of vegetation features and improved contrast.

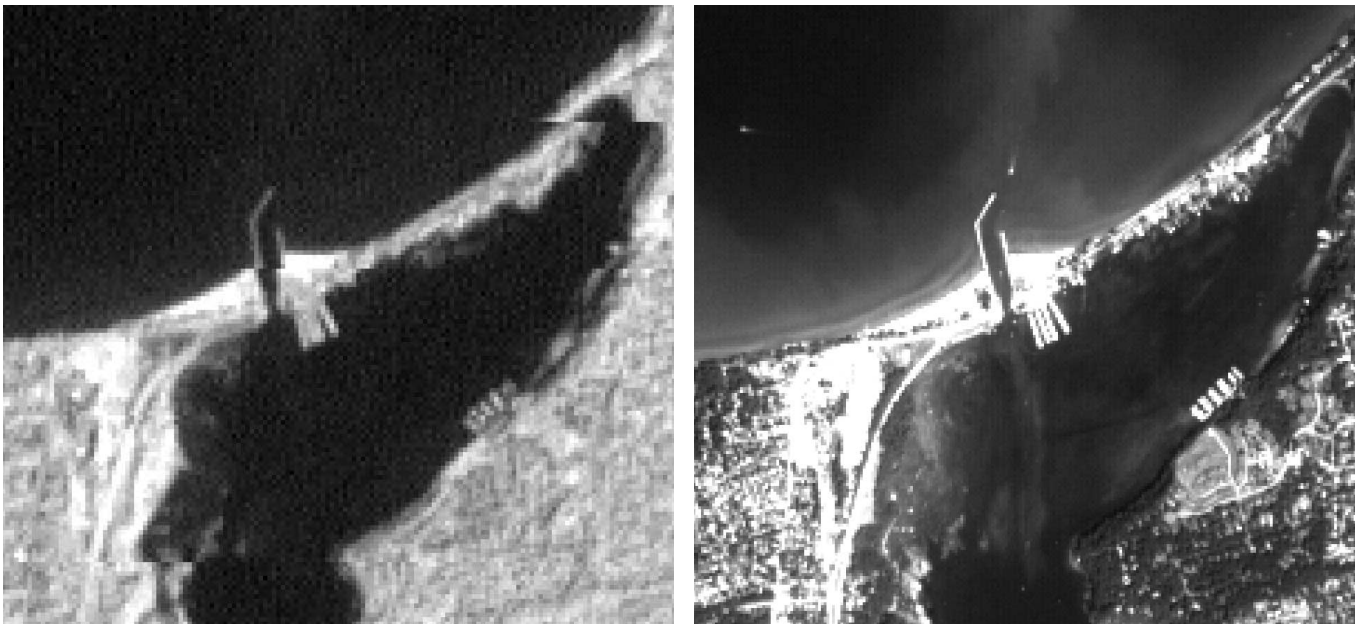

Figure 3. Panchromatic Bands – ETM+ (Left) and ALI (Right)

Spectral and NDVI Comparisons

We extracted 4 pixels each from the ALI and ETM+ images from a reasonably uniform grass region and from the Ballard Ridge forest test site, which we judged by eye to be common between the scenes. We found the overall agreement in spectral response is very good. The largest percent difference is 6% for band 1, but this is only an absolute reflectance difference of 0.005. All other bands agree to within 5%, and the agreement in the SWIR (bands 5 and 7) is ~2%. We find that the formal uncertainty in these reflectance spectra due to the 6S atmospheric correction process is at most ~1.5%, as evaluated by the sensitivity study described above. The uncertainty is largest in the shortest wavelength bands and decreases to less than 0.5% in bands 5 and 7. We note that the new ALI band 5' measures near the peak of the reflectance spectrum, which is unsampled in the ETM+ data.

We calculated the NDVI by calculating the normalized difference between the near infrared and red reflectance values. Figure 4 below are NDVI images calculated from the ETM+ data (left) using bands 4 and 3, and from the ALI (right) using the average of bands 4 and 4' along with band 3. We see the two NDVI images are very similar over land, e.g. both histograms peak at an NDVI value of 0.88 because of the vegetation response. However, we see significant differences between the two sensors in water regions where the signal is very low. We clearly see black and white speckle in the ETM+ data for Lake Ontario, while the ALI is able to distinguish real details in the suspended sediments. The NDVI images show the superior signal to noise of the ALI instrument because of its 12-bit quantization.

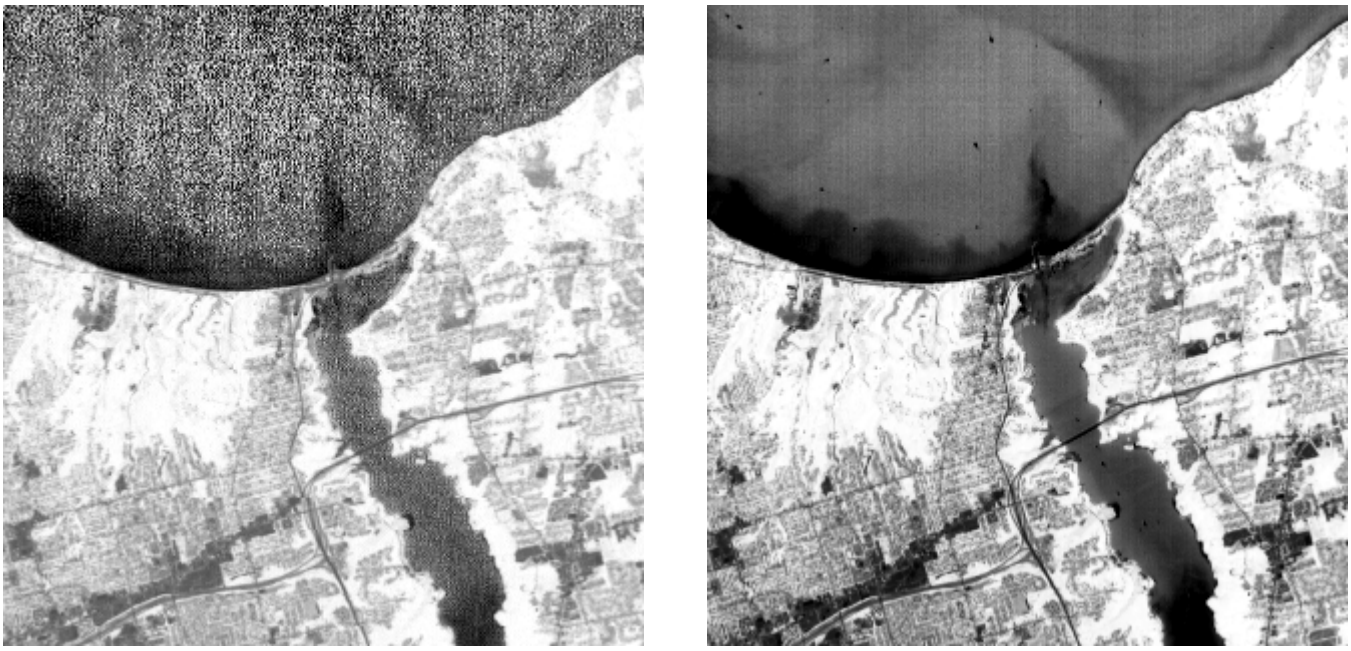

Figure 4. NDVI Inages – ETM+ Bands 3 & 4 (Left) and ALI Bands 3 & 4/4' (Right)

Our results show good qualitative agreement between the multispectral sensors and a significantly improved ALI panchromatic band. We find ≤ 6% differences in the visible/NIR and ~2% differences in the SWIR between the ALI and ETM+ spectral response. Principal component analyses (not reported here) for each sensor indicate that the ALI is able to reproduce the information content in the ETM+ but with superior signal to noise performance because of its increased 12-bit quantization.

Bidirectional Reflectance Distribution Function (BDRF) and Thermal Infrared Modeling of Scenes Imaged with EO-1 and MTI

A second objective of our work is to model the BDRF and thermal infrared characteristics of terrain features at hyperspectral and thermal infrared wavelengths and compare our results to atmospherically corrected EO-1 Hyperion and MTI observations. We selected the Ballard Ridge forest site for intensive measurement and sampling of tree geometry and canopy structure for use in our simulation models. An atmospherically corrected false color composite of the Hyperion image acquired over the area on August 25, 2001 and of a thermal infrared composite of bands L (8.0-8.40 μm), M (8.4-8.85 μm), and N (10.20-10.70 μm) from the MTI acquired on September 9, 2001 are shown below in Figures 5 & 6 respectively.

We used the 6S atmospheric correction code, driven by the Aeronet Sensor, as described above, to correct the Hyperion data. We also have applied the FLAASH atmospheric correction code based on MODTRAN and driven by atmospheric parameters extracted from the Hyperion observations. This is not discussed here, but we are actively researching the application of several atmospheric correction techniques.

Figure 5.
Hyperion Image Acquired August 25, 2001

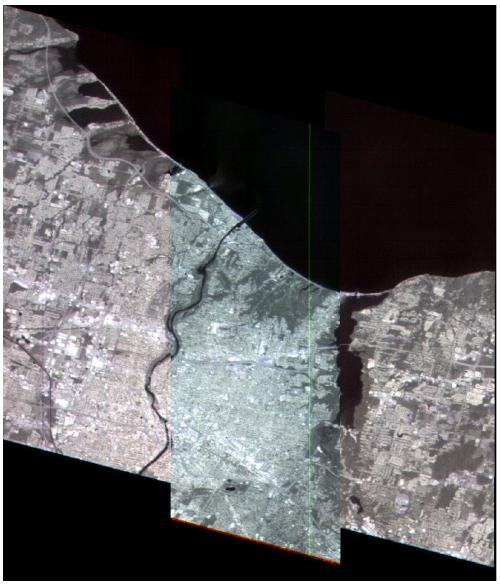

Figure 6.
MTI Image Acquired September 9, 2001

During August and September of 2001, we conducted a detailed survey of the trunk locations, trunk diameter at 1.5 m, crown diameter, canopy dominance (lower, middle, and upper), and species type of approximately 100 trees located within a 30-meter radius.

Plant area index and leaf angle distributions were estimated using indirect optical techniques including the LAI-2000 LAI-meter and hemispherical digital photography. The digital hemispherical photographs were analyzed using Gap Light Analyzer software. The average leaf area index (LAI) from both methods was 4.5.

Detailed geometric measurements of trunks, branches, leaves, leaf clusters, branching angles, and branch length were collected from several trees representing different levels of canopy dominance. These mensuration parameters were then used to generate several geometric tree models. Using the site characterization data, a scene was constructed over a large area that approximated the physical properties of the study site canopy. The resulting tree models were randomly placed at multiple (47,600 trees) locations over a 2 by 2 km area to model the same spacing and density as measured at the study site.

To simulate the reflective wavelengths, we employ simple ray tracing of the reflective and transmissive flux between all scene elements to the sensor. The direct and diffuse flux incident on the canopy are specified and the resulting flux scattered back to the sensor. For the thermal wavelengths, first the temperature distribution of foliage elements are estimated from energy balance models driven by measured meteorological parameters, and then ray-tracing is applied to project thermal exitance from the scene elements into the sensor field of view.

Results

Figure 7, on the left below, is a simulation of the scene at visible wavelengths using a perspective projection out to 45 deg and a viewer position 30 m above the canopy. The solar reflective hot spot can be seen near the upper center of the image. The height of the modeled trees has been varied to match the measured variation in measured tree height at the study site.

Figure 8, on the right, shows the simulation of the scene in the shortwave infrared, 1.55 – 1.73 micrometers. This image is a hemispherical projection out to 90 deg with the viewer 30 m above the canopy. For this short-wave infrared image we also used measured spectral data for the ground, leaves, trunks, and grass in the simulation. In this image the reflective hot spot can be seen approximately 4 deg west of north; this matches the modeled solar azimuth for August 24 at the study site.

Figure 7. Simulation at Visible Wavelengths

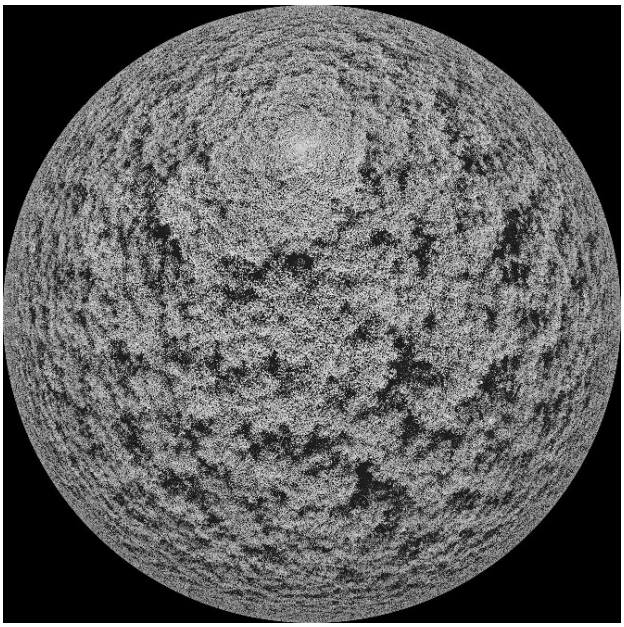

Figure 8. Simulation at Shortwave Infrared Wavelengths

Finally, the Figure 9 below shows the simulation of the canopy in the MTI band M (8.40 – 8.85 micrometers) We have increased the contrast to illustrate the differences in radiance from the sunlit to shaded tree crowns. Gaps in the canopy are much cooler than the surrounding foliage and appear dark. In this high-density canopy (LAI 4.5) the tree trunks, branches, and stem signatures are not easily seen**.**

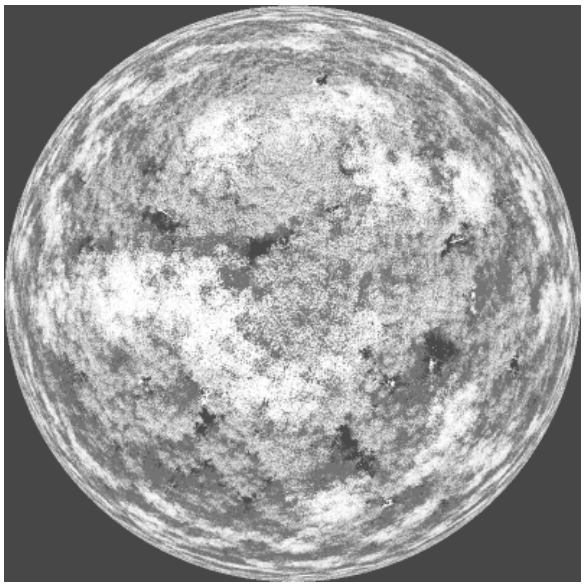

Figure 9. Simulation of Canopy in MTI Band M (8.40 – 8.85 μm)

Acknowledgements

Mr. J. R. Ballard, Jr., U. S. Army Research and Development Laboratory, Dr. J. A. Pedelty and Dr. J. T. Morisette, NASA Goddard Space Flight Center, Dr. S. M. Goltz, University of Maine, and Dr. Lee K. Balick, Los Alamos National Laboratory made major contributions to the work reported here.

Mr. Brent Holben, NASA Goddard Space Flight Center, provided the AERNONET sun photometer at Rochester and Howland. Mr. Don Ho, SSAI, installed the photometer at Rochester during the field campaign and assisted with field measurements. Field spectra at Rochester and other technical assistance were obtained by Ms. Nina Raqueño and Dr. John Schott, Rochester Institute of Technology.

References

J. A. Pedelty, J. T. Morisette, and J. A. Smith, "Comparison of Landsat-7 ETM+ and EO-1 ALI," *Opt. Eng*. 2003 (In Review)

J. R. Ballard, Jr. and J. A. Smith, "Hyperspectral canopy reflectance modeling and EO-1 Hyperion," SPIE Conference, Orlando, FL, 1-5 April 2002.

J. R. Ballard, Jr. and J. A. Smith, "A multi-wavelength thermal infrared and reflectance scene simulation model," Proc. IEEE Intl Geosci. and Rem. Sens. Symposium 2002, Toronto, Canada, 24-28 June 2002.

Chein-I Chang, Shao-Shan Chiang, James A. Smith, and Irving W. Ginsberg "Linear spectral random mixture analysis for hyperspectral imagery," *IEEE Trans. Geosci. and Rem. Sens.* 40(2):375-392, 2002.

James A. Smith and Jerrell R. Ballard, Jr., "Thermal infrared hot spot and dependence on canopy geometry," *Opt. Eng*. 40, pp. 1435-1437, 2001.

Evaluation of EO-1 ALI Data Through an Analysis of Land Cover and Land Use and Local Impacts of Hurricane Iris in Belize, Central America

William A. White, Melba Crawford, Sinan Erzurumlu, Thomas Tremblay, Jay Raney

This investigation evaluated EO-1 Advanced Land Imager (ALI) data by classifying a diverse set of land cover/land use types, comparing the results to previously classified Landsat Thematic Mapper (TM) imagery, analyzing land cover changes associated with natural and manmade events, and evaluating its capability to resolve classification problems encountered with historical TM data. A related objective was to evaluate Hyperion data in terms of potentially improved discrimination capability relative to concurrent ALI and Landsat Enhanced Thematic Mapper Plus (ETM+) data. The research sites were located in central and southern Belize, Central America (Figure 1).

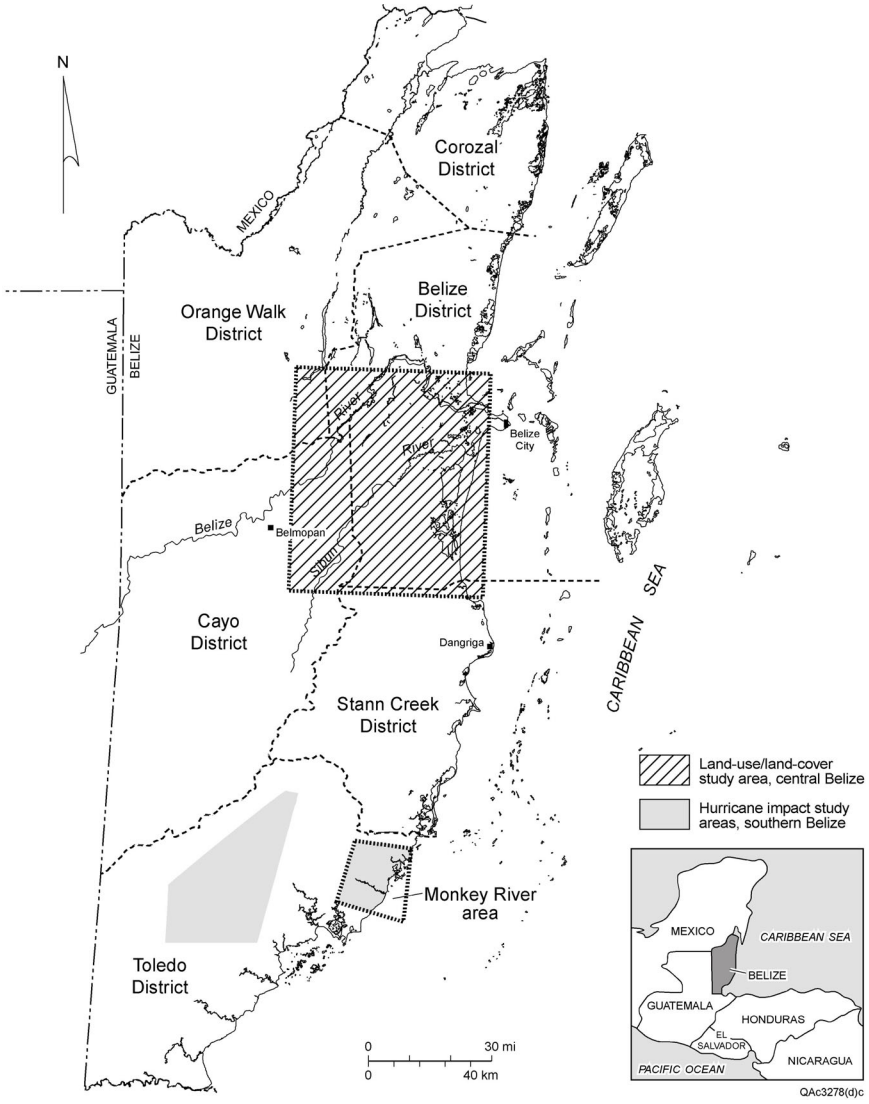

Figure 1. Index map of study areas in central and southern Belize.

Baseline data for the investigation included 1994 and 1996 studies of land cover/land use and deforestation based on Landsat ETM+ data and numerous GPS-located field survey sites and

overflights. Although many EO-1 acquisitions were scheduled in 2001 and 2002, only one acquisition, March 7, 2001, had reasonably cloud-free concurrent ETM+, ALI, and Hyperion data. Small cloud-free areas of ALI acquired on October 1, 2001, December 4, 2001, and March 10, 2002, over southern Belize were also analyzed. A field campaign was conducted in April and May 2002, in central and southern Belize to evaluate land cover/land use classification results, to assess impacts of Hurricane Iris, and to obtain additional field data for refining training sites for supervised classifications. Field data were collected at more than 110 GPS-located sites, which when combined with previously visited sites, provided data for almost 300 field sites. Figure 2 shows an ALI swath and preliminary classification of land cover/land use in central Belize.

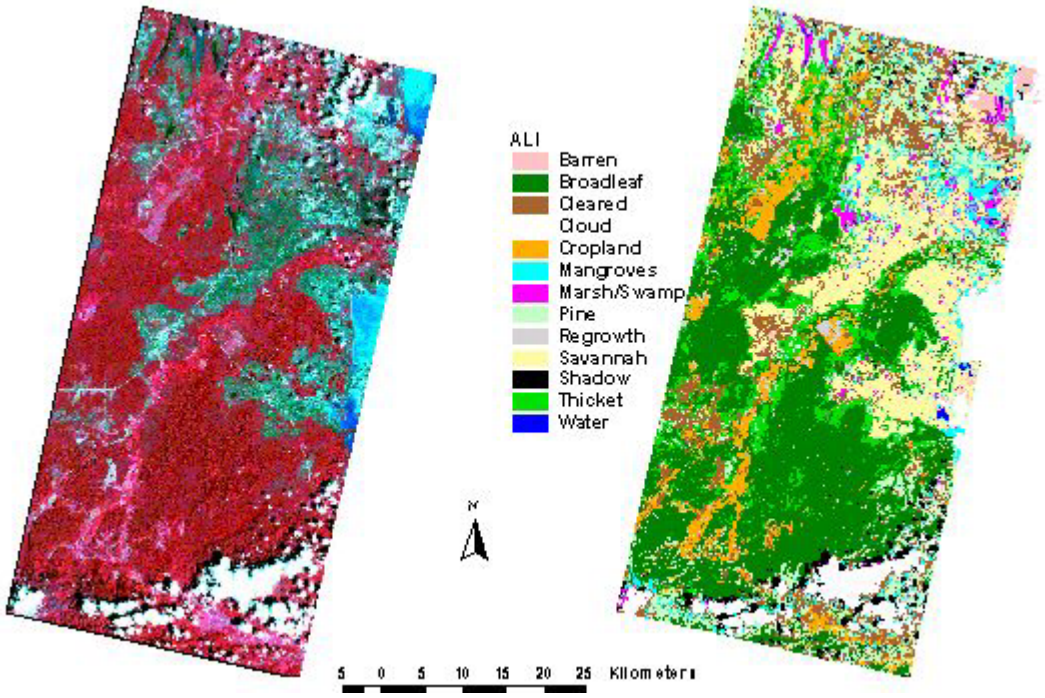

Figure 2. ALI coverage, March 7, 2001, and preliminary classification results in central Belize.

Investigators encountered several problems with the March 7 Hyperion data: no shortwave infrared (SWIR) data were collected, potential artifacts were identified in several bands, the diversity of vegetation in this particular swath was limited, and atmospheric effects were evident. Research then focused on analysis of the ALI data and on development of new statistical methods for analysis of multispectral and hyperspectral data, with the goal of applying these methods to Hyperion acquired at later dates or over other sites. ALI preprocessing included destriping, band-to-band alignment, geometric correction, and georeferencing. Work is ongoing in classifying and analyzing results of ALI and Landsat 7 data in central Belize.

The occurrence of Hurricane Iris provided the opportunity for a later investigation relating to change in forest cover. Hurricane Iris crossed southern Belize on October 8, 2001 (Figure 3). A Category 4 storm with winds exceeding 200 kph, it caused extensive wind damage including toppled and defoliated trees and major losses to the local banana industry. Among the regions affected by the storm were the Monkey River area on the coastal plain and inland mountain regions located approximately 130 km south of Belize City. In this study, investigators evaluated

the capability of ALI data to delineate land cover changes associated with destructive natural events such as hurricanes, focusing particularly on broadleaf forests.

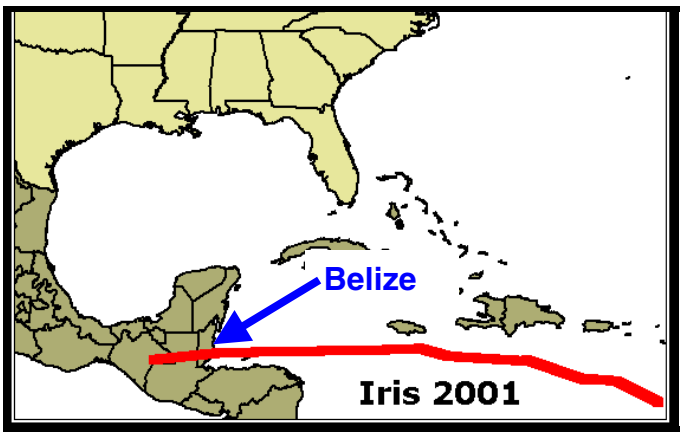

Figure 3. Path of Hurricane Iris.

The study areas spanned approximately 280 km^2 centered on the mouth of the Monkey River and an inland mountainous area more than 600 km^2 in size. Pre-hurricane classification data were acquired of the Monkey River area on March 1996 (Landsat TM) and on October 1, 2001 (Landsat 7 ETM+). Post-hurricane data were acquired on December 4, 2001 (ALI). Figure 4 shows a subset of a 1996 TM image that serves as an "index map." Figure 5 shows comparable natural color pre-hurricane 2001 ETM+ and post-hurricane ALI images.

Figure 4. Close up of 1996 TM image of Monkey River area.

.

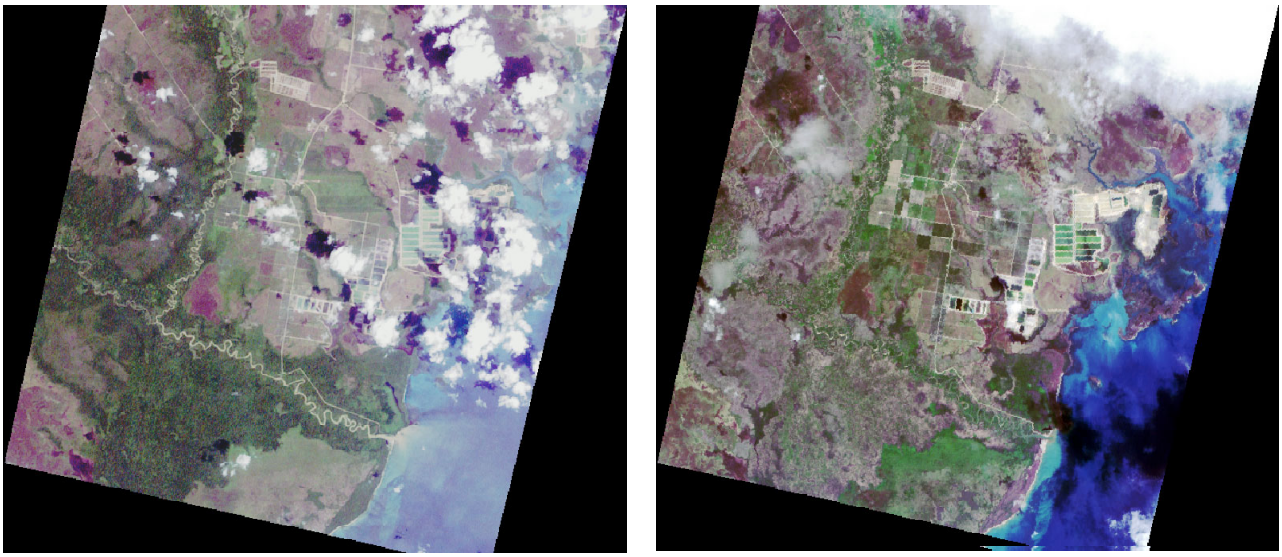

Figure 5. (Left) pre-Hurricane Iris from Landsat 7, October 1, 2001; post-Hurricane Iris from ALI, December 4, 2001. Both are natural color images.

Thirteen land cover/land use classes were identified before the hurricane, including four classes of forest and savannah, five classes of wetlands and coastal land, four classes of developed land, as well as as water, cloud, and cloud shadow. Of particular interest was the impact of the hurricane on the broadleaf forest. Figure 6 shows the pre-hurricane classes, and Figure 7 shows the post-hurricane classes that were mapped in the imagery.

Comparison of pre- and post-hurricane imagery showed substantial losses in broadleaf forests. Broadleaf forests made up approximately 40 percent of the study area in the 1996 Landsat imagery. At the Monkey River site, approximately 20 percent of the area had been classified as broadleaf forest on Landsat 7 imagery acquired pre-hurricane on October 1, 2001. Post-hurricane, ALI 2001 imagery identified less than 1 percent of the area as broadleaf forest (Table 1). Through GIS overlay analysis, the investigators found that areas that had previously been identified as broadleaf forest now had a different spectral reflectance, with more than 70 percent of the area classified as “savannah, pine/savannah, and other grasslands such as farmland.” This change indicated extensive broadleaf defoliation. In the inland study area, broadleaf forests made up about 70 percent of the land cover before the hurricane and only about 12 percent after the hurricane, also indicating extensive forest damage.

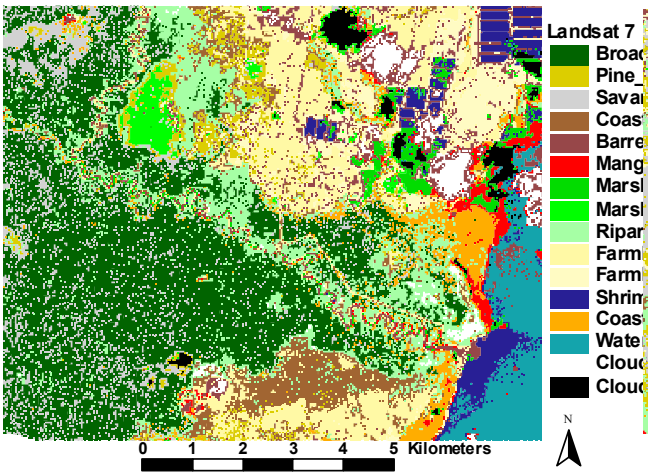

Figure 6. Pre-Hurricane Iris classes.

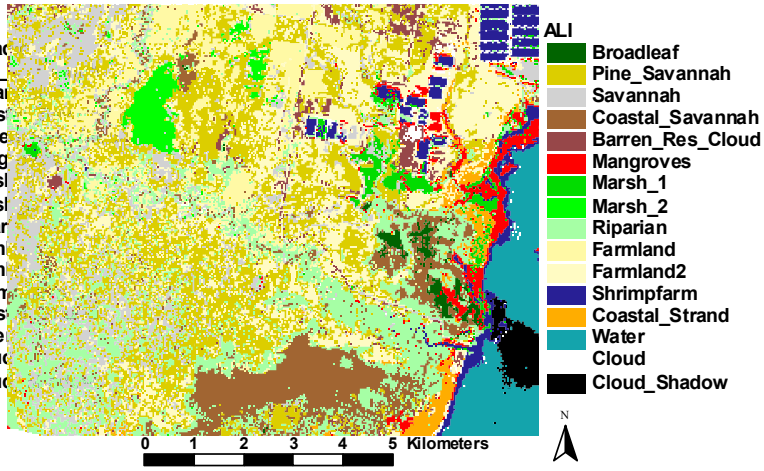

Figure 7. Post-Hurricane Iris classes.

Table 1. Pre- and post-hurricane land cover/land use percentages at Monkey River (Total area ~24,750 ha)

Class	ETM+	ALI
Broadleaf	19.0	0.3
Pine/Savannah	7.3	18.2
Savannah	5.4	9.5
Coastal Savannah	3.1	3.1
Barren/Residential/Cloud	6.3	7.2
Mangroves	2.6	3.7
Marsh 1 & 2	5.7	2.6
Riparian	6.3	7.5
Farmland 1 & 2	17.6	17.5
Coastal Strand	1.9	2.4
Shrimp Farm	2.7	3.5
Water	12.9	12.3
Cloud	6.6	10.6
Shadow	2.5	1.7

Accuracy of the classification using ETM+ October 1 data and ALI December 4 data was also evaluated in using imagery from the two sensors (Figure 8). For all experiments, although classification results were similar, ALI exhibited the highest degree of accuracy in discriminating several difficult class pairs in test data (Table 2). Striping artifacts in ALI were limited and could usually be removed effectively for classification purposes. Accuracy was determined by use of ground truth from field surveys taken in 1996-98. It should be noted that some classes defined in these surveys may have changed in the interim, and additional ground truth is being used to verify the results.

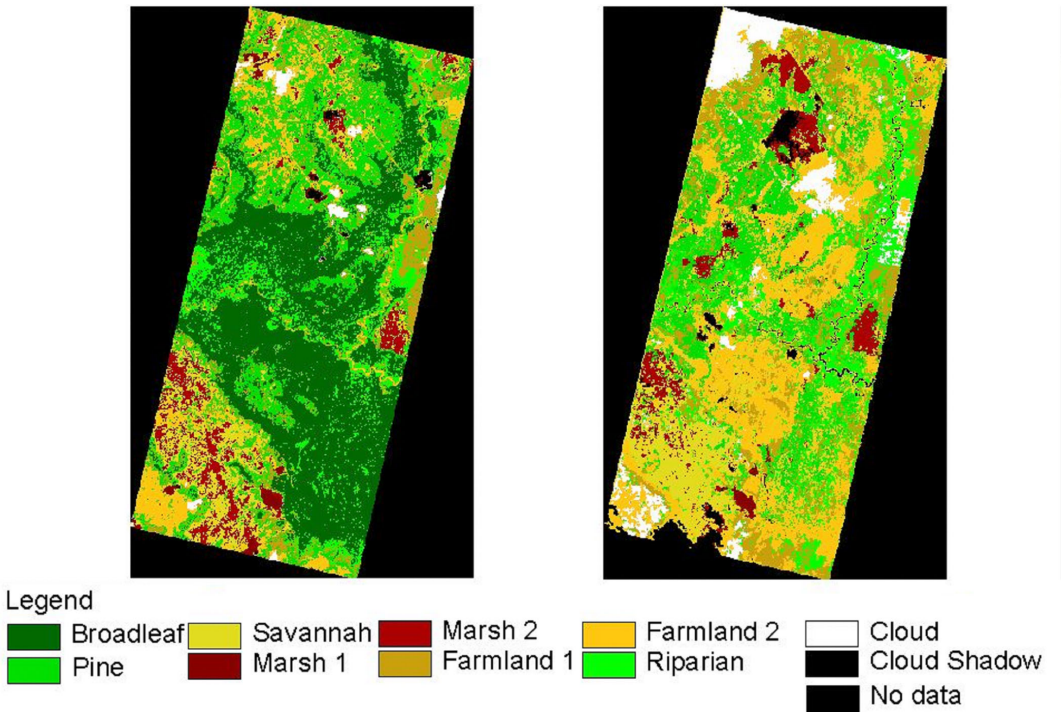

Figure 8. Monkey River area classification results. Landsat results are on the left and ALI on the right.

Table 2. Classification accuracies.

Experiment No.	ETM+ October 1, 2001	ALI December 4, 2001
1	86.29	97.14
2	86.18	98.18
3	86.74	97.66
4	86.74	97.40
5	85.62	97.66
Overall Accuracies	**86.31**	**97.61**
Std. Deviation	**0.47**	**0.39**

Conclusion:

Comparison of ALI and Landsat ETM+ classification results indicated overall that ALI is superior for discriminating several difficult classes such as thicket, regrowth, cropland, and cleared land. In addition, ALI appeared to be superior to Landsat TM data in delineating some coastal land cover classes such as mangrove. Additional ground truth data collected during a field campaign in May 2002, helped verify preliminary classification results, particularly for the mangrove class.

ALI data was also used effectively to determine the impacts of Hurricane Iris on broadleaf forests and possibly on other land-cover types. Changes in spectral signatures and texture were clearly delineated.

ALI Superior SNR Performance